THE ATMOSPHERIC BOUNDARY LAYER ABOVE THE AGULHAS CURRENT

Thesis submitted to the Faculty of Science, University of Cape Town, in fulfilment of the requirements for the degree of Master of Science

Andrew M Lee-Thorp

June 1996

Abstract

This thesis describes the atmospheric boundary layer above the Agulhas Current using shipboard meteorological measurements and rawinsonde ascents. The juxtaposition of the warm Agulhas Current and cool shelf waters is shown to have far-reaching effects on the overlying atmosphere.

Air-sea fluxes of momentum, sensible and latent heat and resultant boundary layer characteristics demonstrate high horizontal inhomogeneity. The results suggest that this inhomogeneity is permanent. The spatial heat flux gradient is reflected in the overlying atmosphere by a transition in stability of the boundary layer and potential cumulus formation from the cool shelf to the warm current.

For airflow perpendicular to the Agulhas Current an internal boundary layer was observed to develop at the inshore sea surface temperature front. Onshore-moving air accumulated a significant quantity of moisture during its trajectory over the current. When airflow is parallel to the current an atmospheric moisture front exists along the axis of the inshore sea surface temperature front.

The mean thermodynamic structure of the atmosphere was investigated. An inversion capped the boundary layer whilst a second, higher-level subsidence inversion was found which acts to limit the vertical development of cumulus clouds and therefore the redistribution of heat and moisture above the boundary layer.

The results presented in this thesis are useful in two ways. The Agulhas Current has frequently been linked to South African climate. This is the first dedicated study which quantifies and characterizes the atmospheric boundary layer in this region. Secondly, maritime airmasses are dramatically modified above the Agulhas Current. The resultant large horizontal inhomogeneity, its vertical extent and permanence suggest that its inclusion is vital to any successful climate model. Atmospheric general circulation models have been criticized for not taking into account regions of strong horizontal inhomogeneity. The results of this thesis support this argument and highlight the need for similar studies.

Acknowledgements

I wish to thank the South African Weather Bureau especially Sidney Marais, Eugene Burger and Piet King, the Sea Fisheries Research Institute for making data available, my office colleagues for their eternal optimism and prevailing sanity, Douw Steyn and Shaun Courtney for their tips on LaTeX, Dr Chris Fairall for his useful hints, and my supervisors Professor JRE Lutjeharms and Dr M Rouault for their guidance.

The financial support of the Foundation for Research Development and the Water Research Commission is gratefully acknowledged.

Contents

List of Figures

List of Tables

Chapter 1

Introduction

The Agulhas Current is the name given to the intense western boundary current on the east coast of Southern Africa.

The continental shelf in this region displays some unusual characteristics (Fig 1.1). In the area of the Northern Agulhas Current, two large offsets may be found in the Delagoa and Natal Bights. The continental shelf then closely parallels the coast until the latitude of Port Elizabeth. Here it widens to form the Agulhas Bank. These features are reflected in the unusual behaviour of the current. The source waters of the Agulhas Current constitute a fully fledged current in the region of Ponta de Oura. In general, the Agulhas Current closely follows the continental shelf. In the area of the Agulhas Bank shear edge features such as eddies, plumes and filaments may be found on the inshore edge of the current. At its southern termination, the current demonstrates a tight, anticyclonic loop in a region known as the Agulhas retroflection, whereupon it flows eastward as the Agulhas Return Current. The Agulhas retroflection region has been shown to be populated with Agulhas rings and eddies (Bang, 1970).

The Agulhas Current circulation system is unique in many respects. Firstly the structure of the continental shelf along which the current flows is quite unusual. Secondly, the invariant flow path of the current is frequently disturbed by anomolous, solitary, downstream perturbations which may exceed the width of the current (Pearce, 1977; Lutjeharms and Roberts, 1988). Thirdly, the Agulhas retroflection is inherently unstable, vacillating between extreme westerly and easterly positions (Lutjeharms and van Ballegooyen, 1988a). Lastly, the Agulhas retroflection is distinctive in terms of its climatological setting. In contrast to other western boundary currents in the northern hemisphere, heat loss from the ocean in the retroflection region occurs throughout the year (Bunker, 1988; Walker and Mey, 1988).

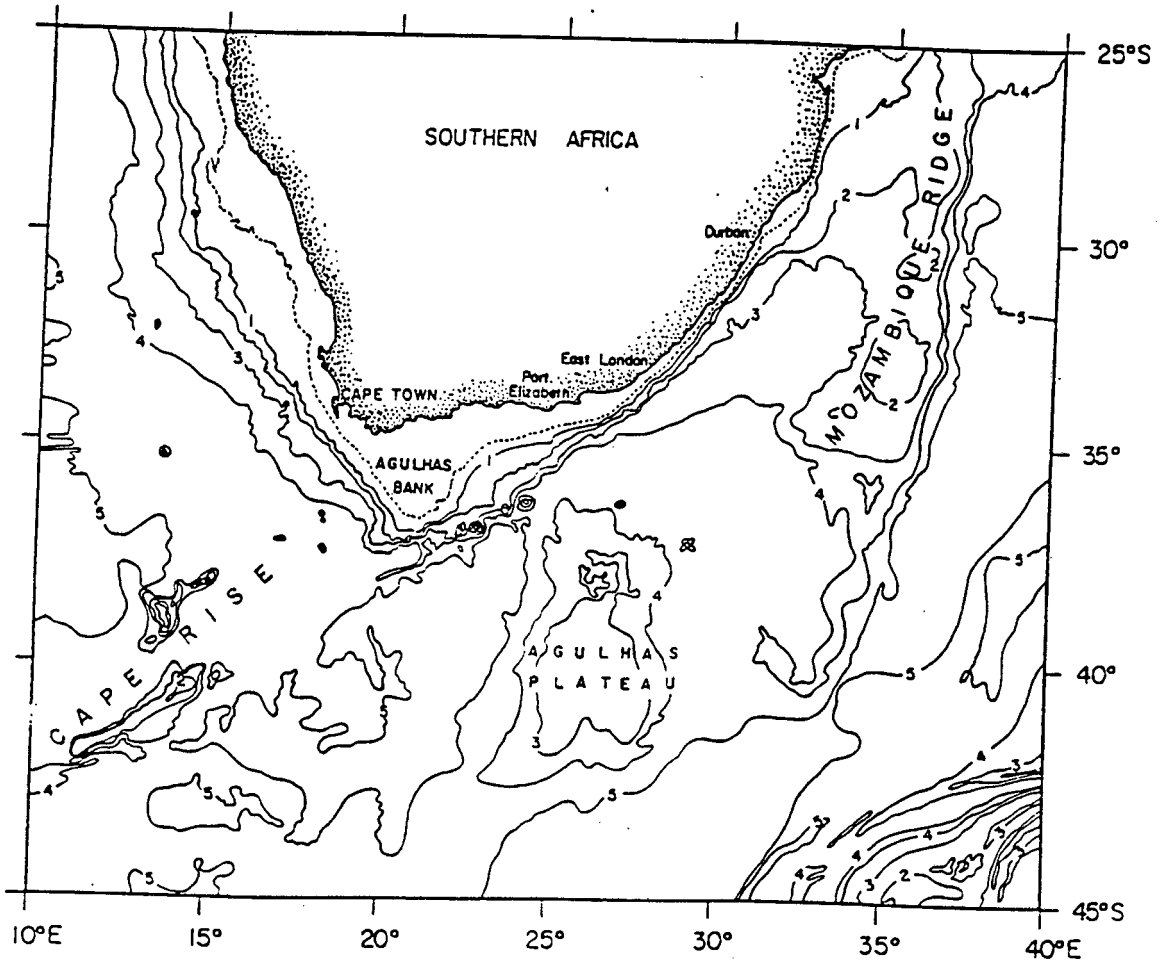

Figure 1.1: The bottom topography of the ocean area adjacent to South Africa. The contours are at 1000 m intervals. The continental shelf is indicated by the 200 m contour (dotted line).

Recent statistical correlations (Walker, 1990; Jury et al., 1993) have demonstrated that heat losses in the Agulhas Current proper and Agulhas retroflection play an important regulating role in the weather and climate of the subcontinent. The mechanisms of control have been actively investigated (Jury and Walker, 1988; Mey et al., 1990; Jury 1993). These studies, however, have produced more questions than answers. In order to investigate the interaction between ocean and atmosphere in those key ocean areas, a dedicated research programme has been instituted (Rouault and Lutjeharms, 1994) of which this thesis forms a part.

Despite the recognised importance of the Agulhas Current circulation system and associated oceanic environment on the weather and climate of the subcontinent, few studies to investigate these relationships have been undertaken to date. As a result our understanding of the mechanisms is poor. This is due, in part, to the daunting task of relating air-sea interactions to weather and climate. Since air-sea interactions over the Agulhas Current transmit their effect on weather and climate through the lower domain of the atmosphere, the boundary layer, it is not difficult to motivate research in this field. A key question may therefore be formulated. What are the characteristics of the boundary layer over the Agulhas Current ?

This thesis sets out to quantify the nature of *air-sea interactions* and the *boundary layer over the Agulhas Current.*

Since a rather scant preliminary picture of the Agulhas Current has been presented here, the next chapter provides a more detailed overview for those less familiar with the Agulhas Current. The following chapter, *Air-sea interaction over the Agulhas Current* explores our current knowledge on the nature of air-sea interactions in the Agulhas Current system.

Chapter 2

The Agulhas Current

The Agulhas Current is considered to be *the* major western boundary current in the southern hemisphere (Gordon, 1986).

It forms the western limb of an anticyclonic subtropical gyre in the South Indian Ocean. The South-Equatorial Current in the north, an eastward flow in the south, including the South-Indian Ocean Current and a complicated northward-flowing closure in the east serve to complete the system (Lutjeharms, 1996).

The historical portrayal of the Agulhas Current circulation system shows the Agulhas Current as being derived from the "Mozambique Current" and the East Madagascar Current. The latter would supplement the Agulhas Current-Mozambique Current continuum by flowing westward upon passing south of Madagascar. Thus the South Equatorial Current was seen to feed the Agulhas Current via the separate routes of the Mozambique Channel and the area east of Madagascar. Subsequent research has, however, demonstrated the inadequacies of this simple model.

The East Madagascar Current closely follows the continental shelf on the east coast of Madagascar. Lutjeharms et al. (1981) have identified this current as an intense, miniature western boundary current. South of Madagascar it retroflects and reenters the subtropical gyre. Whilst most of this water returns to the centre of this gyre some may intermittently enter into the Agulhas Current circulation system in the form of rings, eddies or filaments (Lutjeharms, 1988).

Water flowing southward within the Mozambique Current through the Mozambique Channel was considered to be a precursor to the Agulhas Current. Saetre and Jorge da Silva (1984) have questioned the idea of such a continuum, using a large collection of hydrographic data to

substantiate their argument.

A third possible source for Agulhas Current water is recirculation within the Southwest-Indian Ocean subgyre. Evidence presented by Duncan (1970) gave notice of this possibility. Harris (1972) has shown that the waters of the Agulhas Current off Durban were composed of two main types during the spring of 1964. A small portion was derived from the Mozambique Current (14 %) flowing through the narrows of the channel. The other was composed of recycled water (86 %) which itself has three main sources in the South Equatorial Current, Agulhas Return Current Water recycled west of the Mozambique Ridge and water recycled in a local vortex.

It is important to note that this does not validate the concept of direct inflows from two western boundary currents (Lutjeharms, 1996). Indeed, according to the analysis of Harris the East Madagascar Current proper was not a source. Furthermore, Saetre and Jorge da Silva (1984) have suggested that the Mozambique Channel is populated by a range of eddies of various sizes which dictate the apparently chaotic flow within the channel.

It is now apparent that the Agulhas Current consists mainly of recycled water with smaller contributions from the South Equatorial Current via the separate routes of the Mozambique Channel and the area east of Madagascar. A schematic depicting the essential elements of the above discussion can be seen in Fig. 2.1 (which shows a smaller percentage being recirculated).

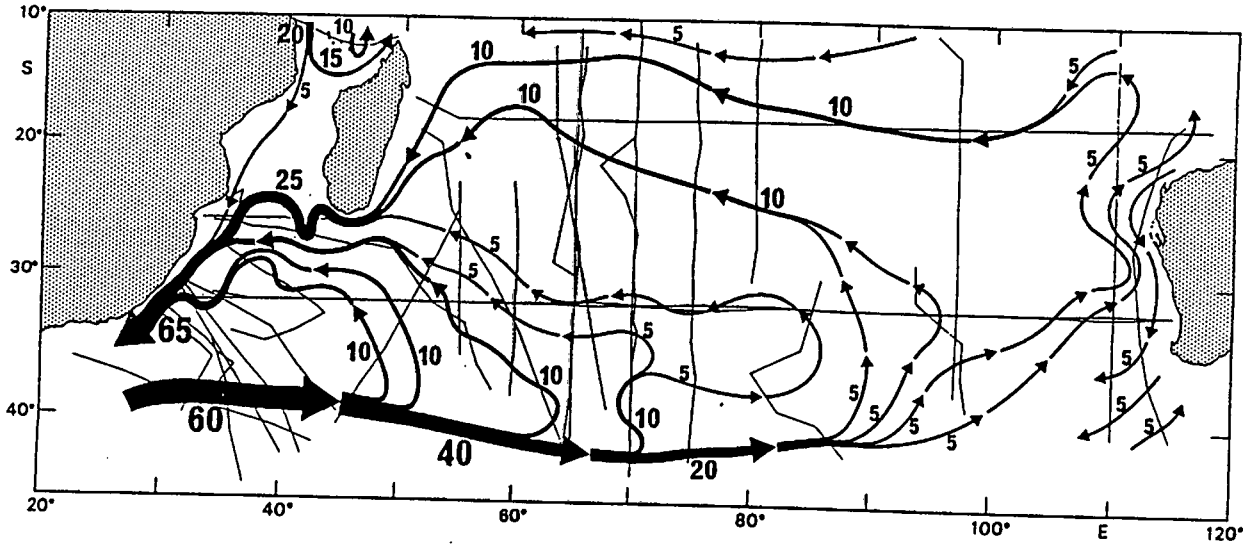

Figure 2.1: Schematic illustration of the flow field in the South Indian Ocean. The volume transport in the upper 1000 m is given in Sverdrups ($10^6 m^3 s^{-1}$). Thin lines denote ship transects from which the flow field was reconstructed (after Stramma and Lutjeharms, 1995).

Having first focussed our attention on the sources of the Agulhas Current, we now turn to

the Agulhas Current proper. In the region of Ponta do Oura, Mozambique these waters are a part of what may be considered to be a fully constituted Agulhas Current.

The volume flux in the upper 1000 m near Port Edward is estimated to be 62×10^6 m^3s^{-1} and increases by 6×10^6 m^3s^{-1} per 100 km downstream (Gründlingh, 1980). For the most part, the continental shelf is narrow (usually about 12 km). Exceptions to this rule occur in the northern part of the Agulhas Current System. North of Durban, in the Natal Bight, the shelf is about 50 km wide. Further north, an even larger offset may be found in the Delagoa Bight. The current follows closely the continental shelf until the latitude of Port Elizabeth. Here the continental shelf widens to form the Agulhas Bank (Fig. 1.1). As a result of the narrow, coast-parallel continental shelf the Agulhas Current demonstrates a nearly invariant flow path which is considered to be quite unusual for a western boundary current (Lutjeharms, 1994). In the upper layers, however, greater variability is observed.

The results presented by Pearce (1977) will be used to provide a general description of the features of the northern Agulhas Current. Pearce (1977) undertook a detailed study of the mesoscale structure and variability of the upper 500 m of the Agulhas Current off the coast of Durban and compared his results with those from other western boundary currents. He has concluded that the thermohaline structure of the Agulhas Current in this region is very similar to other western boundary currents where isotherms dip sharply downward away from the coast (Fig. 2.2). The surface expression of the Agulhas Current is characterized by three distinct zones.

- A western (or inshore boundary) contains cooler shelf water in a cyclonic shear zone of relative high velocity and thermal gradients.
- The location of the velocity core lies seaward of this inshore thermal front in narrow zone, the current core. Speeds in excess of 1 ms^{-1} may be found here.
- An eastern (offshore boundary) is characterized by weak anticyclonic velocity shear with much smaller thermal gradients.

Pearce has estimated the width of the Agulhas Current to be between 90 and 100 km. This compares with values found for the Florida Current (75 km) and East Australia Current (40 - 80 km) (Pearce, 1977). Pearce has also concluded that the current can meander on a scale of the order of tens of kilometres. Similarities with observations of the Florida Current led him to suggest a downstream propagation of the wave-like motion.

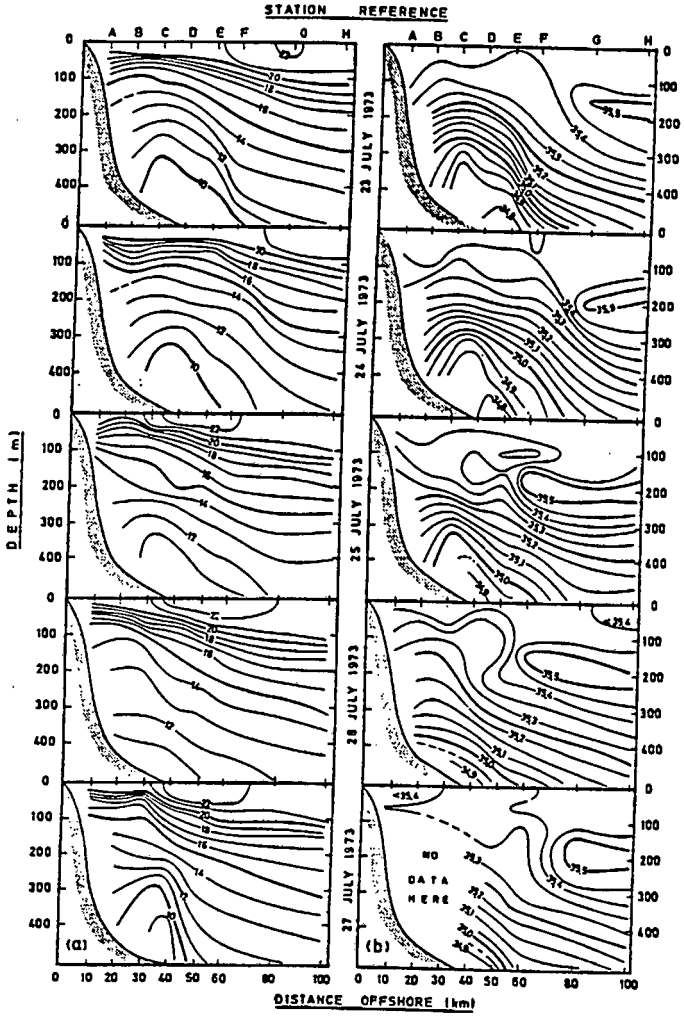

Figure 2.2: Daily vertical sections of temperature (left) and salinity (right) off Durban on the dates shown (after Pearce, 1977).

From just north of Port Shepstone to just south of East London the narrow continental shelf parallels the coast and the current is deemed to be stable. Downstream of Port Elizabeth the presence of a wider, steplike shelf facilitates the growth of small perturbations into substantial meanders (Lutjeharms 1981b). This results in the formation of shear edge features such as eddies, plumes and filaments on the inshore edge of the current.

In its terminal region in the south (Fig. 2.3), the Agulhas Current performs a tight, anticyclonic loop or retroflection in a region shown to be populated by a range of eddies (Bang, 1970). Lutjeharms and van Ballegooyen (1984) have shown that potential vorticity considerations preclude the possibility of a poleward flow of the current beyond the southern reaches of the coast of Southern Africa. A continued poleward flow relies on an increasing depth of the current. Since the depth is limiting in this case, potential vorticity considerations result in the Agulhas Current turning. The retroflected limb of the Agulhas Current, the Agulhas Return Current, follows closely the Subtropical Convergence (STC) as it proceeds eastward, exhibiting high levels of dynamic mesoscale variability and eddy shedding (Lutjeharms and Valentine, 1988) and enhancing the intensity of this thermal front (Lutjeharms, 1985). This swiftly flowing, eastward current carries out a sudden northward meander upon reaching the Agulhas Plateau which may be repeated over other topographic features (Lutjeharms, 1996) until it becomes part of the South Indian Ocean Current.

It is most likely that the flow characteristics of the Agulhas Current upstream of the Agulhas Retroflection area are instrumental in modulating the behaviour of the current in this region (Lutjeharms, 1994). This in turn has implications for South African climate (Walker, 1990) and interocean exchange of thermocline water (Gordon, 1986).

The Agulhas Retroflection is not stable. Lutjeharms (1981a) has used satellite imagery to demonstrate the inherent instability of the loop, its coalescence, and resultant ring formation with an average diameter of 324 km (Lutjeharms, 1981b). Of course, not all of the water reaching the retroflection is involved in the formation of Agulhas Rings. Most of this water flows eastward as the Agulhas Return Current. Nevertheless, the quantities of water involved in ring formation represents an enormous amount of energy (Olson and Evans, 1986).

Agulhas Rings are closed loops of warm Agulhas water which circulate independently of the mother current. Rings exhibit a distinct annulus-type water distribution at the sea surface shortly after spawning and should not be confused with eddies. Gordon (1986) has suggested that the exchange of thermocline water between the Southwest Indian and Southeast Atlantic oceans completes the global thermohaline circulation.

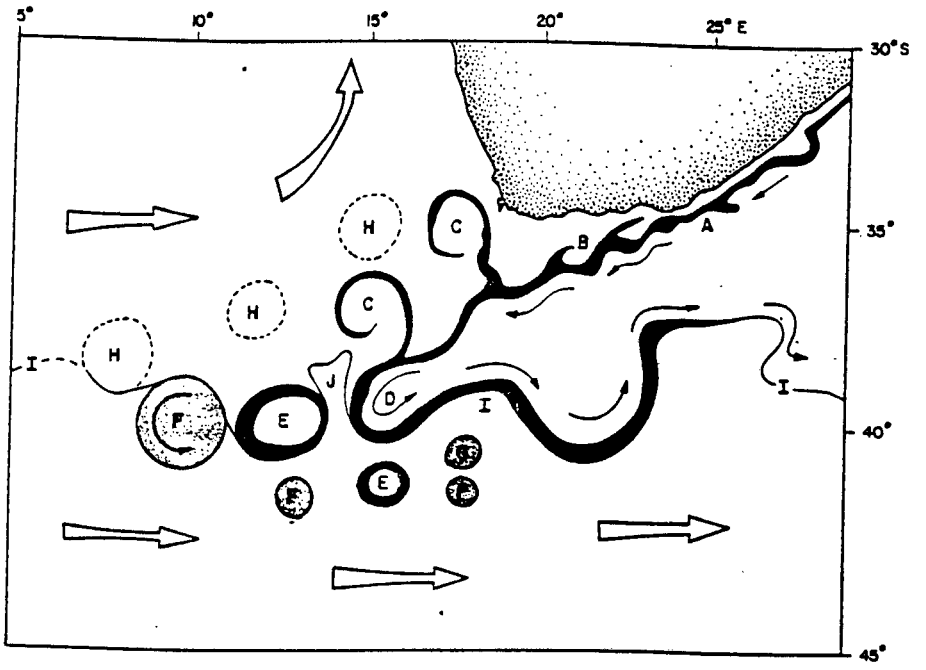

Figure 2.3: The Agulhas Current Retroflection and associated features (after Lutjeharms and van Ballegooyen, 1988a). Features are: A, the narrow, well-defined surface expression of the Agulhas Current adjacent the narrow continental shelf: B, meanders in the current path next to the Agulhas Bank; C, Agulhas rings delineated by warm Agulhas Current filaments; D, the Agulhas retroflection loop; E, newly spawned Agulhas rings of which surface features are still identifiably rings; F and H, older Agulhas rings in various stages of decay; G, a warm eddy south of the subtropical convergence; I, the Subtropical Convergence; J, wedge of cold Sub-Antarctic water.

Until recently (Lutjeharms and van Ballegooyen, 1988a), the frequency of ring-shedding, and the mean location and behaviour of the retroflection was unknown. High rates of surface cooling of newly spawned Agulhas rings and eddies have been inferred (Walker and Mey, 1988) such that their surface expressions may decay within a two month period (Lutjeharms and van Ballegooyen, 1988a). A conceptual model of Agulhas Ring formation based on satellite imagery is given by Lutjeharms and van Ballegooyen (1988a). The Agulhas Retroflection lies between 20° and 16° E. A characteristic westward progradation of its westernmost edge is demonstrated with an average period of 39 days. Each progradation event is accompanied by the growth and intrusion from the south of a wedge of cold Sub-Antarctic Surface Water which separates the newly-formed ring from the Agulhas Retroflection loop (Fig. 2.4).

Rings shed at the Agulhas retroflection may move northwestwards (Duncombe Rae, 1991) or southwards whereupon crossing the STC they generally drift eastwards (Lutjeharms and Valentine, 1988). The rapid decay of their surface signature makes it difficult to provide a reliable estimate of their distribution using thermal infrared satellite imagery although overall lifetimes of two years (Lutjeharms and van Ballegooyen, 1988a) and 3 - 4 years (Byrne et al., 1995) have been suggested. Although the shedding of rings at the retroflection is not unusual for other western boundary currents, the rate of shedding of 9 rings per year for the Agulhas Current is considered unusual (Lutjeharms and van Ballegooyen, 1988a). The large diameter of Agulhas rings (average 342 km) suggest that such features may introduce considerable mesoscale variability into air-sea transfer processes in the Agulhas Retroflection Region (ARR) (Walker and Mey, 1988). Lutjeharms and van Ballegooyen (1988a) have also suggested that the Agulhas Retroflection Region may in fact be quite congested with both rings and eddies in various stages of decay. This will result in considerable sea surface temperature variability in the mesoscale. Quite apart from the dynamic nature of the Agulhas Retroflection itself, this situation suggests that mesoscale atmospheric variability may in fact be an inherent part of this region (Guymer et al., 1983).

The mechanism(s) which precipitate the formation of a ring at the retroflection is (are) unclear, although upstream perturbations to the flow path of the current that progress downstream, are possible candidates.

It was mentioned previously that inshore shear edge perturbation features are known to develop downstream of Port Elizabeth. In contrast to these shear edge features which originate due to localized instability, solitary, intermittent excursions of the Agulhas Current such as observed by Pearce (1977), appear to emanate upstream of Port Elizabeth, in the vicinity of

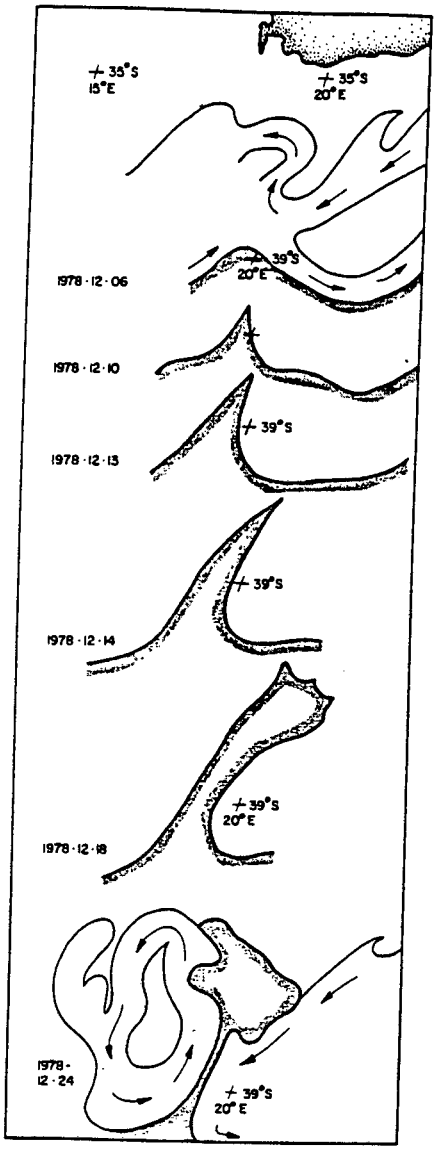

Figure 2.4: The shedding of an Agulhas Ring is preceded by the intrusion from the south of a wedge of cold Subantarctic Surface water (after Lutjeharms and van Ballegooyen, 1988a).

the Natal Bight area (Lutjeharms and Roberts, 1988). These excursions of the Agulhas Current were named the Natal Pulse for their assumed inception area in the Natal Bight and are an exception to the characteristically stable flow observed north of Port Elizabeth.

Results from investigations using satellite remote sensing (Lutjeharms and Roberts, 1988) confirm that the northern Agulhas Current is subject to these large, intermittent, solitary meanders which are spawned as cold core, cyclonic trapped lee eddies in the Natal Bight. Their downstream propagation on the inshore edge of the current may last for up to 8 weeks, they have an average diameter of greater than 170 km and are evident along some part of the Agulhas Current for nearly 20% of the time. While it has been suggested (Lutjeharms and Roberts, 1988) that the adsorbtion of shoreward-moving deep sea eddies in the area of the northern Agulhas Current (see eg. Gründlingh, 1988) might draw in water from the current and initiate downstream propagation of a Natal Pulse, Schumann (1981) has also shown the decisive role played by the wind.

It is not clear whether the sea-surface temperature variability associated with a Natal Pulse (order of 2 - 3 °C, Lutjeharms and Roberts, 1988) implies that such a feature might enjoy small-scale atmospheric variability within its domain. It has been shown that a pulse may extend its influence in a dramatic way by precipitating an early retroflection of the Agulhas Current (Lutjeharms and van Ballegooyen, 1988b). It is possible that the Natal Pulse modulates the behaviour of the retroflection and the process of ring-shedding in this way. This reduces the amount of water available to participate in the normal retroflection, the accompanying ring shedding process, and the completion of the global thermohaline circulation (Lutjeharms, 1994).

Clearly the Agulhas Current is highly dynamic. The decisive role that it may play in the transfer of water, heat and salt between the two ocean basins will continue to drive interest and oceanographic research in this area.

How does the Agulhas Current influence climate, in particular Southern African climate, and how does climate influence the Agulhas Current? These questions may be investigated as ocean-atmosphere coupling mechanisms (Walker, 1990) and are discussed in the next chapter.

Chapter 3

Air-sea interaction over the Agulhas Current

In order to investigate potential ocean-atmosphere coupling mechanisms one may begin by looking at the boundary layer of the atmosphere.

The boundary layer of the atmosphere is that lower part of the atmosphere that responds to surface forcings on time scales on the order of an hour or less (Stull, 1988). Over the oceans, the boundary layer is referred to as the marine atmospheric boundary layer (MABL). These terms will be used interchangeably to describe the boundary layer over the ocean. It is clear that any role that the Agulhas Current may have to play, depends firstly on the air-sea transfer processes that modify the MABL, and secondly how the MABL interacts with the atmospheric circulations that control the daily weather, and ultimately the climate.

Air-sea interactions work both ways, on many temporal and spatial scales, and are interrelated. Thus it is increasingly becoming the trend to treat the ocean-atmosphere system as a *coupled* system in air-sea interaction investigations (eg. Charnock and Businger, 1991 and Webster and Lukas, 1992) and in simulations of global climate (eg. Foreman ,1990; Cattle and Gordon, 1990).

Recently, researchers have undertaken numerous air-sea interaction investigations in Southern African waters with both a climatological (Walker and Mey, 1990; Walker, 1990; Jury and Levy, 1993; Jury et al., 1993) and a meteorological (Jury and Courtney, 1991; Jury, 1993; Jury, 1994; Jury and Walker, 1988; Mey et al., 1990) emphasis.

Climate studies have, of neccessity, tended to treat air-sea interactions over the adjacent oceanic region as a black box. This is due to the fact that too few dedicated air-sea interaction

studies have been undertaken with the result that a conceptually reliable and useful model has yet to be proposed. As shown below there are large knowledge gaps in our understanding of ocean-atmopshere coupling mechanisms in the oceanic region adjacent to the subcontinent.

In the following section the current knowledge on air-sea interaction involving the Agulhas Current is reviewed. It begins with a review of the meteorological studies that have been undertaken and ends with a discussion of how these have been related to the climatology of the region. Despite the high standard of research in this area, there are still many unknowns. In particular, the boundary layer over the Agulhas Current system has received little attention. It is the objective of this thesis to begin to fill this gap.

What then is the nature of air-sea processes operating in the Agulhas Current System?

Differences in sea surface temperature (SST) between the cool shelf waters and the warm Agulhas Current (Pearce, 1977) offer the possibility of a semi-permanent mesoscale circulation system that can interact with transient weather systems (Jury, 1993). Indeed satellite images frequently show the presence of a line of deep cumulus clouds organized in the alongshore direction over the Agulhas Current either as singular cloud lines or as cloud streets (Lutjeharms et al., 1986). A SST front manifests itself as an atmospheric thermal front aligned with the axis of the SST front (Friehe et al., 1991).

Aircraft observations (Jury and Courtney, 1991) along a NW - SE cross-section of the northern edge of the Agulhas Current near the eastern Agulhas Bank during uniform, light, zonal (westerly) flow were composited to elucidate the mean boundary layer structure (Jury, 1993). The flight path covered a SST front of 8 °C $(40\text{km})^{-1}$.

For *zonal westerly flow* (airflow from the cooler shelf waters to the Agulhas Current), typical of the winter season, the following results were obtained (Jury and Courtney, 1991; Jury 1993).

- The surface heat and momentum fluxes increased by a factor of 5.
- A warming and moistening of the boundary layer had implications for a subsequent deepening over the Agulhas Current (the latter not being explicitly demonstrated).
- Airflow accelerates over the front and decelerates downstream resulting in divergence, subsidence, clear weather formation and convergence, convection and cumulus formation over the front and current respectively.
- Mixing through the boundary layer is accomplished by convective eddies of some 3 km horizontal extent.

- A low-level jet exceeded geostrophic values by about 50 % and indicates the presence of a thermal front in the atmosphere.

- These features are quasi-stationary.

- A thermal internal boundary layer (TIBL) usually, although in this case not, associated with a clearly defined top (Stull, 1988; p 600) is defined by the vertical wind variances (i.e. vertical gustiness). The depth of the TIBL increases with fetch downstream.

Schumann (1989) questioned the relationship between wind speed and pressure and particularly whether geostrophy applies to the South African coastline. Jury's (1993) derivation of the surface fluxes was obtained from the lowest aircraft flight level at 100 m. A question arises as to whether these measurements were made within the surface layer. Within this layer fluxes vary vertically by less than 10 % (Stull, 1988). Bulk aerodynamic flux calculations may only be applied to measurements made within the surface layer. Even with appropriate adjustments to the transfer coefficients bulk aerodynamic flux calculations are unreliable when measurements are made far from the surface. Jury (1993) did not include the stability dependence on moisture and used invariant transfer coefficients for the surface heat fluxes. Model-simulated and observed thermodynamic structures did not agree well (Jury, 1993; Figures 6 and 7). Whilst the model-simulated wet-static energy showed vertically stratified and well-mixed structures over the inshore region and current respectively, the observed, composite equivalent potential structure was always stratified, with an upslope toward the current. A comparison of wet-static energy and equivalent potential temperature is not useful as wet static energy utilises the assumption that any kinetic energy is locally dissipated into heat whilst the equivalent potential temperature does not use this assumption (Stull, 1988, p 545). If indeed enhanced pressure gradient and baroclinic effects are responsible for the low-level jet as postulated by Jury (1993) then its alignment over the axis of warmest water is unusual. Instead its presence might be expected to coincide with the strongest SST gradient where the former processes are most rigorous.

The meteorology of the Agulhas Bank is in fact highly variable over time, alternating between easterly and westerly flow. Easterly flow is required to initiate upwelling near the surface (Schumann et al., 1982). A direct consequence is that alternating wind stress may partially control the surface expression of the Agulhas Current and related SST front in the region. This has implications for the secondary circulations observed by Jury (1993). Transient anticyclones initiate shallow easterly flow whose characteristics within the boundary layer are quite unlike the westerly wind regime (Jury, 1994).

During easterly flow the airmass has already undergone modification over the warm Agulhas Current. Composite aircraft results for a single level across the Agulhas Current in this region distinguish the characteristics of *easterly flow* (Jury, 1994).

- Winds increase sharply toward the Agulhas Current (and the coast) whilst rotating clockwise toward the coast. The inshore zone is generally characterized by light winds.

Moving south of the Agulhas Bank, the Agulhas Current enters the retroflection region.

It is well known that for the globe as as whole, maximum oceanic heat losses to the atmosphere occur over western boundary currents at mid-latitudes (Budyko, 1963; cited in Walker and Mey, 1988). It is to be expected that the Agulhas Current will experience greatest energy losses to the atmosphere in that region where high SSTs are continually exposed to cold air outbreaks. The Agulhas Retroflection area is such a region. Walker and Mey (1988) have used VOS (Voluntary Observing Ship) data to construct a heat flux climatology for this region. Unlike the Gulf Stream in the northern hemisphere which exhibits a pronounced annual heat flux cycle with maximum losses in winter (Bunker, 1976; cited in Walker and Mey, 1988) the Agulhas Retroflection Region is continually exposed to cold, unsaturated, maritime air embedded within the westerlies (Walker and Mey, 1988). Their results are outlined below.

- A high heat flux core (200-225 Wm^{-2}) within the Agulhas Retroflection Region is found at 37° - 41° S, 16° - 22° E.
- The latent heat flux exceeds the sensible heat flux by up to 90%.
- A weak, semi-annual heat flux cycle shows maximum losses in winter and spring.
- Spatial heat flux gradients are more pronounced in summer. This means that locally, cyclogenesis may not be as seasonally dependant as in the northern hemisphere.
- Spatial heat flux gradients are determined primarily by SST variability.
- Magnitudes of SST (and heat flux) variability on an interannual cycle exceed those of the intrannual cycle.

Questions arise as to the treatment of the bulk flux calculations (Walker and Mey, 1988). Transfer coefficients of C_H=1.2×10^{-3}, C_E=1.3×10^{-3} and $C_H = C_E$=0.85×10^{-3} were used for unstable and stable conditions respectively. Use of nearly invariant transfer coefficients (varied only on the type and not the degree of stability), exclusion of the moisture dependence of stability

and bulk calculations based on climatic averages instead of bulk averages raises doubts about their conclusions. The assumption that bulk fluxes derived from climatic means are equivalent to climatic means of bulk fluxes merited futher attention. This also raises doubts about the relative differences (eg. spatial gradients) emphasised by Walker and Mey (1988).

Nevertheless, on the basis of these findings it was concluded that heat loss from the ocean to atmosphere in this region was an important climatic factor (Walker and Mey, 1988). Subsequent investigations (Jury and Walker, 1988; Mey et al., 1990) have attempted to quantify and understand these exchange processes.

Meteorological observations from an aircraft survey in the retroflection region have shown the response of the MABL to a SST front of 6 °C at the edge of the Agulhas Current (Jury and Walker, 1988). Significant boundary layer modification was demonstrated as the cool westerly flow encountered the warm current. A number of processes contributing to MABL modification were shown to be operating simultaneously on this occassion.

- Turbulent heat fluxes were enhanced over the warmer water.
- Divergence in the near-surface horizontal winds occurred. (This was attributed to daytime thermal entrainment onto the continent (sea breeze)).
- The surface layer wind accelerates over the SST front in a sea breeze like fashion.
- A mesoscale sea-breeze structure existed when synoptic-scale forcing was weak and intitiated a singular N-S cloud line.
- A boundary layer height growth and warming rate of $60 mC^{-1}$ (SST) and $1°C\ (100\ km)^{-1}$ was found.

Jury and Walker (1988) did not provide an explanation of how the above warming/growth rates were derived. Presumably they are based on the slopes of the temperature and dewpoint profiles (Jury and Walker, 1988, Figure 6). It is also not clear whether the quoted rates are based on maximum, minimum or average slopes. If they reflect the temperature and dewpoint slopes then vertical resolution and horizontal sampling distances are important considerations. A more reliable boundary layer growth/warming rate statistic is proposed in Chapter 5.

Whilst daytime thermal entrainment has been proposed as a mechanism for divergence of near-surface horizontal winds, the structure observed (Jury and Walker, 1988; Figures 3 and 4) closely resembles the expected anticyclonic wind-field structure. Jury and Walker (1988) also

proposed that the MABL growth characteristics are influenced by synoptic scale divergence and subsidence of transient anticyclones. which serve to constrain the vertical extent of eddies.

Since lowest aircraft data were measured at a height of 70 m, these data were interpolated to 10 m values assuming a neutral atmosphere, before deriving bulk fluxes. Transfer coefficients of C_H=1.2 $\times$ 10^{-3}, C_E=1.5 $\times$ 10^{-3} and $C_H = C_E$=0.85 $\times$ 10^{-3} were used for unstable and stable conditions respectively. Poor treatment of stability (the moisture effect was excluded), use of nearly invariant transfer coeffecients (varied only on the type and not the degree of stability), and uncertainties regarding 10 m interpolated data are weaknesses which limit the usefulness of their description of the surface heat fluxes.

A more descriptive study within the greater Agulhas Retroflection Region (Mey et al., 1990) has shown that under a *westerly wind regime* surface heat flux processes are enhanced under the simultaneous occurrence of strong winds and a cold air outbreak (a maximum of 828 Wm^{-2} was found). Their results for *westerly zonal flow* are outlined below.

- The MABL is characterized by strong low-level baroclinicity and low static stability.
- Surface lapse rates are superadiabatic as a result of surface warming.
- Dramatic increases in wind speed over the ARR-STC SST front are associated with increased turbulent heat flux over the warm water.
- For the case where the wind blew *along* the ARR-STC front a jetlike flow parallel to the front and observed vertical wind shear were both closely related to the meridional gradient in SST.
- When a zonal wind blew *perpendicular* to the SST front (from cold to warm), marked vertical wind shear was replaced by a boundary layer in which winds were well-mixed.

Bulk fluxes were derived from three-hourly, shipboard observations (Mey et al., 1990). This is less than ideal as bulk flux derivations are intended for bulk averaged variables. Three-hourly observations are instantaneous readings once every three hours and are a poor substitute. The air-sea flux parametrization scheme was identical to that of Walker and Mey (1988). No data were available for intercomparison. A maximum heat loss of 828 Wm^{-2} compares with values found for the Gulf Stream (Bane and Osgood, 1989). Slowly ascending radiosondes were released to elucidate the boundary layer structure. The boundary layer top was then defined by a sudden change in slope of the dewpoint isotherm (Mey et al., 1990). However, at the time of the study, radiosonde ascents (undertaken by the South African Weather Bureau) were designed for

operational forecast purposes only. This meant that only data from specific pressure levels (about 10 levels within the first 3000 m) were recorded, regardless of the ascent rate. This, coupled with an inadequate definition of the boundary layer height weakens the argument that boundary layer deepening was observed. The subsidence inversion height was erroneously identified as the boundary layer top and the study failed to demonstrate low static stability as the lapse rate of most vertical profiles did not exceed the dry adiabatic lapse rate (Mey et al., 1990; Figure 6).

Mey et al. (1990) argued that the observed processes may operate to enhance cyclogenesis by enhancing low-level baroclinicity and increasing the "tilt" of a westerly trough (Holton, 1979, p 126; Mey et al., 1990). Furthermore the destabilized MABL is a source of energy to the region of frontal uplift. Whether this area sustains cyclogenesis remains to be tested, nevertheless, the above discussion highlights the climatic importance of the Agulhas Retroflection Region.

Under an *easterly wind regime* air-sea transfer processes over the ARR and the Agulhas Current proper were quite unlike the *westerly* scenario (Mey et al., 1990).

- The airmass had already undergone modification over the warm current.
- Downward heat fluxes had implications for low-level stability and reduced surface wind stress.
- This situation is associated with a ridging (transient) anticyclone.

Having established some of the features within the boundary layer of the Agulhas Current over parts of its domain, various authors (eg. Walker, 1990; Jury et al., 1993) have used this information to construct a climatology of atmospheric control and interaction by the Agulhas Current.

As the Agulhas Current flows south from its source region of mostly subtropical atmospheric influence, it enters into a region whose atmospheric controls become increasingly dominated by mid-latitude influences (Preston-Whyte and Tyson, 1988). Coastal summer conditions are dominated by transient anticyclones which initiate shallow sub-tropical easterly flows. In winter, topographically trapped coastal lows track anticlockwise along the coast from west to east, often preceding mid-latitude westerly depressions whose influence is increasingly felt southwards.

Jury et al. (1993) have undertaken a statistical study of the influence of the Agulhas Current on summer rainfall along the southeast coast of the subcontinent between 28° - 34° S and 26° - 33° E in the transition region of sub-tropical/temperate influence.

- They flound a strong correlation between adjacent coastal rainfall and SST (r = +0.88), and shelf-width (r= -0.92).

- Rainfall was found to decrease in a NE-SW gradient in conjunction with a NE-SW decline of maximum sea-surface temperature within the core of the current.

- These results indicate the influence of the proximity and temperature of the warm Agulhas Current adjacent to the coast, on the local rainfall.

Jury et al. (1993) provided a conceptual in which essentially two mechanisms are thought to produce alongshore variations in coastal rainfall. They are

- the modification of onshore moving air by surface heat fluxes, and

- the interaction between transient weather systems and the embedded mesoscale circulation over the Agulhas Current.

The former process, however, has not been studied in this region and moreover the the latter possibility (eg. secondary circulations) has only been observed for westerly flow (Jury, 1993).

Under *strong synoptic conditions* the following model may be appropriate (Jury et al., 1993). Where the shelf is narrow, the Agulhas Current flows close to the coast. If the shelf is narrow or wide, the fetch length over the relatively cooler shelf waters is limited or increased respectively. Recall that observations (Jury and Courtney, 1991; Jury, 1993) have shown the sharp decrease in surface heat fluxes in this inshore zone. The resultant increase in stability has implications for moisture uptake and wind stress. This feature is complemented by the fact that where the shelf is narrow the escarpment rises steeply along a narrow coastal plain. Where the shelf is wide the escarpment rises gently along a wide coastal plain. Where the shelf is narrow, orographically forced convection therefore may provide a complementary influence.

Jury (1993) has suggested that quasi-stationary, secondary convergent circulations are embedded within the Agulhas Current. Under light winds associated with *gentle synoptic forcing* or a more *alongshore component of flow* sustained convergence over the surface heat core is complemented by a subsiding cell near the front (Fig. 3.1). Jury et al. (1993) have postulated that the position of the subsiding limb is indirectly influenced by shelf width. Where the shelf is wide, the quasi-stationary zone of subsidence is located on the inshore edge of the current and suppresses rainfall (Fig. 3.1, top panel). Where the shelf is narrow, the steep orographic upslope (and subsequent uplift) may counteract subsidence (Fig. 3.1, lower panel). The results indicate the possible role played by the Agulhas Current in air-sea interactions in this region, leading

to inputs of heat and moisture into the sub-tropical airmass, and the modification of transient weather systems.

It remains to be shown that the quasi-stationary circulation features observed by Jury (1993) occur also during the summer rainfall months when airflows are predominantly easterly. The analysis of Jury (1993) occurred during westerly flow associated with transient mid-latitude depressions, systems known to be inherently baroclinic (Holton, 1979). Easterly airflows are associated with transient anticyclones and constitute an essentially barotropic environment quite unlike that of westerly flow.

Walker (1990) has examined statistical relationships between South African summer rainfall and SST variability in the surrounding oceanic current regimes. Her analysis includes the entire summer rainfall region (Fig. 3.2). Those results pertaining to the Agulhas Current circulation system are discussed below.

Wetter summers occurred with relatively higher SSTs in the Mozambique/Agulhas Current region. The ocean warming along the east coast and southern reaches of the Agulhas Current System is accompanied by stronger easterly winds in the South Indian Ocean especially in the area of Madagascar where large north-easterly anomalies were found. This suggests that the Indian Ocean Anticyclone is displaced polewards and westwards of its mean summer position. A concomitant poleward shift of the wind stress curl zero line in turn has implications for the Agulhas Current and will be discussed later. In particular the waters of the Agulhas Current may penetrate directly westward into the Southeast Atlantic Ocean. Walker (1990) has discussed ways that air-sea interactions may operate under these conditions and has outlined two mechanisms that may enhance summer rainfall. They are

- increased moisture convergence over the interior and
- tropical-temperate trough formation.

The simultaneous occurrence of a warmer Agulhas Current (hence a warmer, moister boundary layer) and stronger onshore winds increases moisture convergence over the tropical and sub-tropical interior (Fig. 3.2, top panel). Further south, cyclogenesis occurs (Fig. 3.2, top panel) in association with intensified SST gradients in the ARR and resultant differential temperature advection (Holton, 1979). The highly dynamic nature of the boundary layer processes in the ARR has been discussed earlier. On a synoptic scale it is postulated that the tendency for intensification of mid-latitude low-pressure systems in the ARR might facilitate the formation of tropical-temperate troughs (Fig. 3.2, lower panel). These troughs are aligned in a NW-SE

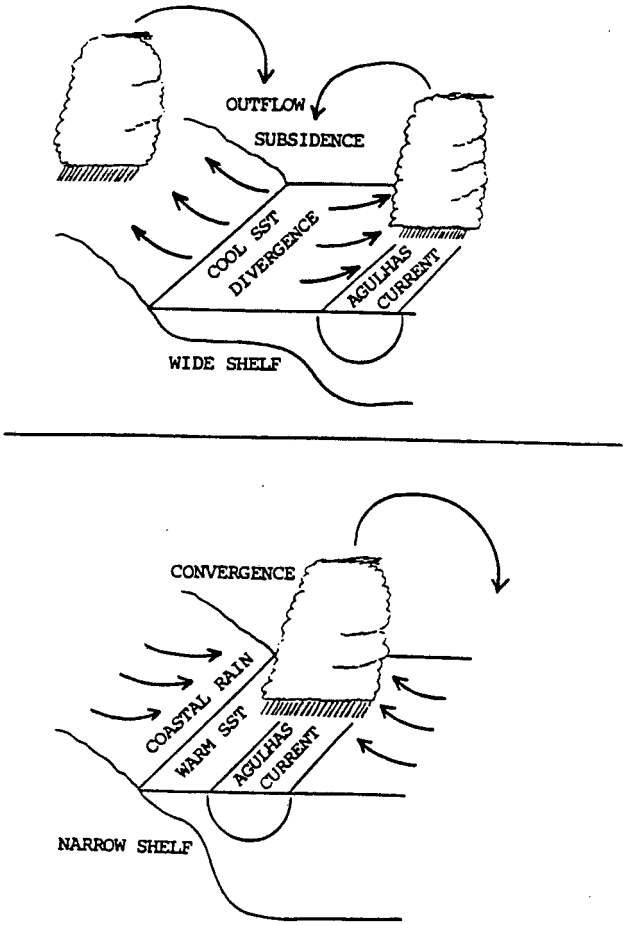

Figure 3.1: Schematic diagram of contrasting secondary mesoscale circulations and associated convection for wide (top panel) and narrow (bottom panel) shelf scenarios according to the hypothesis proposed by Jury et al. (1993).

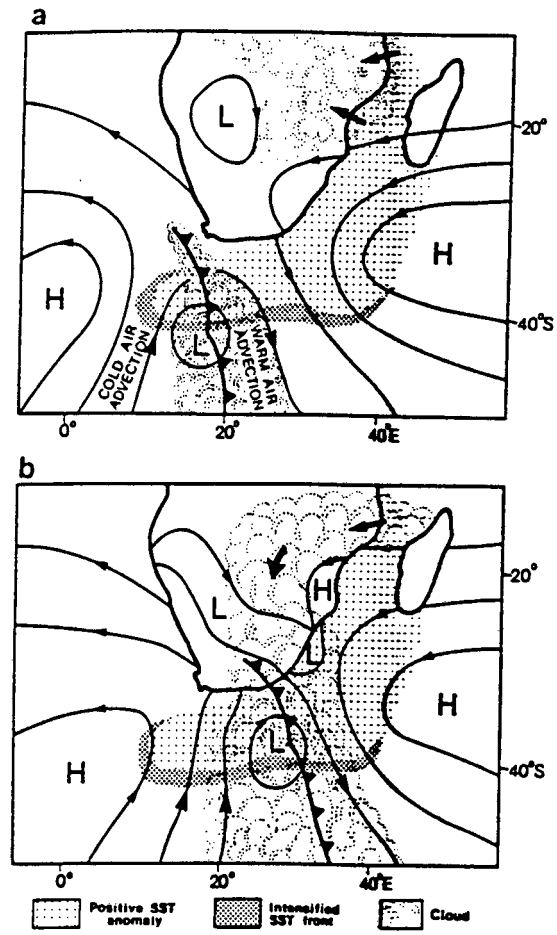

Figure 3.2: Schematic representation of enhanced tropical end extra-tropical circulations associated with SST anomalies in the Mozambique/Agulhas and Agulhas Retroflection regions. Abnormally moist tropical air fuels convection over the interior whilst further south abnormally warm waters and high SST gradients in the retroflection region enhance local cyclogenesis (top panel). Surface convergence and upper air convergence intensifies through latent heat release as tropical and temperate circulations are coupled, producing cloud bands across the interior (lower panel) (after Walker, 1990).

direction across the interior and are responsible for between 50 % and 90 % of South Africa's rainfall during most months (Harrison, 1984). The tendency is for the contribution of this synoptic type to increase during wetter (summer) months. Tropical-temperate troughs are associated with cloud bands which connect tropical and temperate circulations (Preston-Whyte and Tyson, 1988; Harrison, 1984). This system provides a conduit for the poleward transfer of momentum and energy.

Walker's postulation that stronger onshore advection of warmer, moister air under large-scale, enhanced easterly circulation may enhance rainfall through increased moisture convergence over the interior is supported by the findings of Jury et al. (1993) for the coastal regions where highest SSTs are associated with highest levels of summer rainfall. It remains to be shown, however, that Agulhas Current *warm events* in the ARR (Walker, 1990) are indeed related to enhanced local cyclogenesis and to increased tropical-temperate trough formation. The former is likely to be a prerequisite for the latter. Since interannual SST variability in the ARR exceeds the intra-annual variability (Walker and Mey, 1988) this region is expected to play a role on a climatic as well as synoptic scale. Boundary layer processes in this region may even impact beyond South African climate. Apart from the role in modulating South African rainfall, such processes are likely to play a small role in the global atmospheric circulation of the southern hemisphere. On a global scale it may modulate the atmospheric exchange of momentum and energy between the tropics and the high-latitudes by virtue of its influence on cloud band formation. It is primarily this exchange which drives the global atmospheric circulation.

It is apparent therefore that the air-sea interactions over the Agulhas Current may influence South African climate in two ways (Walker, 1990; Jury et al., 1993).

- Deepening, moistening and warming of the boundary layer has implications for moisture convergence and rainfall.

- Local cyclogenesis in the ARR may favour tropical-temperate trough formation.

How does climate in turn, influence the Agulhas Current?

The relationship between the Agulhas Current circulation and the large scale atmospheric circulation is not well determined. As a result, varying interpretations of these couplings may lead to contradictory conclusions being drawn on how the Agulhas Current operates under different climatic regimes and vice versa. This has implications for the robustness of climate predictions which involve the Agulhas Current. It is therefore vitally important to understand the full set of ocean-atmosphere coupling mechanisms in the Southwest Indian Ocean subgyre.

Results from a study into drought episodes in the eastern Cape watershed (Jury and Levey, 1993) reveal a case in point. Walker (1990) attributed Agulhas Current warmings to an abnormally strong easterly wind forcing in the South Indian Ocean (northeasterly wind anomaly in the Agulhas Current source region) which was said to cause a poleward shift of the *wind stress curl zero line* and increase poleward flow in Agulhas Current surface layers. Modelling results (de Ruijter 1982; de Ruijter and Boudra, 1985) show that a poleward shift in the wind stress curl zero line can lead to a "coupling" of the Southeast Atlantic and Southwest Indian Oceans as a result of the Agulhas Current extending westward of its mean retroflection position. Walker (1990) has suggested that the resultant positive SST anomalies enhance summer rainfall over the interior.

The eastern Cape watershed is a coastal region located at the south-eastern extremity of the subcontinent. It lies within the transition zone of convective, sub-tropical summer rainfall regime to the northeast and stratiform, mid-latitude winter rainfall regime to the west. Jury and Levey (1993) found that dry periods in this area generally occur with abnormal north-easterly wind forcing in the Southwest Indian Ocean which is postulated to increase the volume transport of the Agulhas Current, thereby causing an early retroflection (Lutjeharms and van Ballegooyen, 1984). The result is that adjacent SSTs (i.e. in the retroflection region) are some 3 °C lower during drought periods in the eastern Cape watershed.

How does this contradiction arise? Walker (1990) claims that easterly wind anomalies in the Southwest Indian Ocean cause an abnormally warm, westward extension of the Agulhas Current whilst Jury and Levey (1993) relate abnormal easterly wind forcing to an early retroflection and cooler SSTs in the ARR. Both cite valid, although somewhat speculative, arguments for the behaviour of the Agulhas Current. Both attempt to relate the behaviour of the Agulhas Current to rainfall and climate, although admittedly on somewhat different spatial scales.

It is likely that the Agulhas Current is essentially decoupled from the circulations in the Mozambique Channel and directly east of Madagascar (Lutjeharms et al., 1981; Saetre and Jorge da Silva, 1984). Since the Agulhas Current displays no seasonality (Pearce and Gründlingh, 1982) atmospheric circulation anomalies (eg. abnormal easterly wind forcing) in the Agulhas Current source regions of the Mozambique Current and east of Madagascar may have very little effect on the behaviour of the Agulhas Current even in the surface layers. Recall that the Agulhas Current forms the western boundary of a larger wind-driven subgyre in the South Indian Ocean (Stramma and Lutjeharms, 1995). Lutjeharms and van Ballegooyen (1984) have shown that an increased volume transport may precipitate an earlier retroflection. Modelling results (de

Ruijter 1982; de Ruijter and Boudra, 1985) have demonstrated the influence of the wind stress curl zero line on the degree of westward extension of the Agulhas Current. However, no clear relationship between these factors (viz. easterly wind forcing, the position of the wind-stress curl zero line and volume transport) has yet been found.

The question of the influence of climate (large scale atmospheric circulation) on the Agulhas Current is therefore unanswered. Caution should be exercised if conclusions regarding climate are to be drawn from speculated deviations of the Agulhas Current related to atmospheric circulations.

Chapter 4

Research objectives

It is worthwhile emphasising that to date our knowledge of air-sea interaction mechanisms over the Agulhas Current has been gleaned from just *three* meteorological experiments (Jury and Walker, 1988; Mey et al. 1990; Jury and Courtney, 1991). This lack of knowledge is reflected in the summary below.

- Surface heat and momentum fluxes have been poorly described.
- Quantification of moisture uptake has been ignored.
- The characteristics of the MABL of the northern Agulhas Current are unknown.
- The dramatic MABL response to *westerly flow* has been adequately demonstrated whilst the response to onshore moving, *easterly*, tropical/sub-tropical air originating seaward of the Agulhas Current is poorly documented.
- The extent to which modification of *easterly flow* contributes to moisture convergence over the interior is unclear. Is abnormal easterly wind forcing more important? In other words, separation of kinematic and thermodynamic processes is difficult. Again it is clear that moisture uptake needs quantification.
- Mesoscale circulations are embedded over the Agulhas Current under *westerly* and possibly under *gentle alongshore flow*. This has not been tested under *easterly flow* or strong synoptic forcing.
- The response of the Agulhas Current to atmospheric circulation anomalies is not understood.

The importance of air-sea interactions on the weather and climate of the subcontinent has merited the introduction of a dedicated research programme (Rouault and Lutjeharms, 1994). An understanding of the boundary layer over the Agulhas Current is a first step toward understanding how air-sea interactions in this region affect the local weather and climate. In studies to date surface fluxes have been poorly described, and with the exception of Jury and Courtney (1991) and Jury (1993), a poor quantative description of the boundary layer structure and modification has been given.

Therefore, an accurate description of the surface fluxes of heat, moisture and momentum and a quantitive description of the boundary layer (especially of moisture uptake) is deemed to be an important component of this new research venture.

This thesis attempts to quantify the nature of *air-sea interactions* and the *boundary layer over the Agulhas Current.*

In Chapter 5 the data and methodology is described. The results are presented in Chapter 6. The latter has been separated into a discussion on the Agulhas Retroflection Region and the Agulhas Current. Since the Agulhas Retroflection Region has previously been the subject of extensive study this region is only discussed briefly and is used to introduce some concepts that will be applied to the Agulhas Current. Finally, the results are summarized in Chapter 7.

Chapter 5

Data and methods

Data from three South African meterological research cruises will be considered. The three cruises are the 1994 Marion Island Relief Cruise, 1995 Marion Island Relief Cruise and the Agulhas Current Air-Sea Exchange Experiment (ACASEX) cruise (Rouault et al., 1995). The first two cruises are part of a routine annual program to supply the SAWB meteorological base on Marion Island whilst the third was a dedicated meteorological research cruise.

Henceforth the three cruises will be referred to as M94 (1994 Marion Island Relief Cruise), M95 (1995 Marion Island Relief Cruise) and ACASEX. The data were collected aboard two (R/V SA Agulhas and R/V Algoa) of three research vessels of the Department of Environmental Affairs and Tourism (DEAT). M94 and M95 aboard the R/V SA Agulhas covered the Agulhas Retroflection Region and ACASEX aboard the R/V Algoa covered the Agulhas Bank and southern Agulhas Current. The overall area spans the Agulhas Retroflection Region, the Agulhas Bank and the Agulhas Current south of East London.

Due to the rapid eastward tracking of synoptic systems, a problem of synoptic non-stationarity arises. If a specific feature or interaction is to be investigated then the problem may be partially overcome by considering "stationary" synoptic conditions or small time intervals. In these cases a time series will be considered to constitute a series in space.

Data and instrumentation in this study can be categorized in two groups, namely *surface* and *upper-air* data.

5.1 Surface data

5.1.1 Data and Instrumentation

The fleet of DEAT vessels is equipped with a number of physical devices which measure a variety of useful geophysical information. A Data Distribution System (DDS) samples these data at 1 second intervals. The values obtained are averaged over 1 minute and stored with relevant information such as time, date, latitude and longitude. Whilst automatic measurement does not necessarily represent any technological advance, it has enabled the collection of high resolution data that has been used for the first time in an air-sea interaction study for this region. Such high resolution data will be shown to be an improvement over the traditional 3-hourly meteorological observations employed in previous studies such as in Mey et al. (1990).

Parameters of particular interest are air pressure, wind speed, wind direction, air temperature, sea surface temperature and air humidity.

Three-hourly surface observations were undertaken on the M94 and M95 cruises by the South African Weather Bureau. These data are used for comparative purposes.

5.1.1.1 Wind speed and direction

Wind speed and direction were sampled at 1 seconds intervals, averaged over 1 minute and stored. This represents a wind vector relative to the mean ship motion. Therefore wind vectors were simultaneously readjusted against the ship movement vector to obtain an absolute wind vector (i.e. relative to the ground).

An Aerovane-type anemometer (Fitschen and Gay, 1979) was used to measure the wind speed and direction. Two types of Aerovanes were used. This information is summarized below together with the manufacturer's accuracy specifications. Whilst it may be considered that this type of anemometer is less influenced by atmospheric turbulence, possesses low inertia and pursues wind direction well (with little swing) there are uncertainties about its performance at low wind speeds (starting speed of less than 2 ms^{-1}) and response to ship's roll. A problem exists on the R/V Algoa whereby the gyrocompass stabilises only after a few minutes during sharp changes in the ship's direction. Hence there is a bias in the calculation of the absolute wind speed during these periods.

Table 5.1: Instruments used in this study

MAKE AND MODEL	PARAMETER	DATASET	ACCURACY
KOSHIN-VANE KA-101	WIND SPEED, DIRECTION	M94	1 ms^{-1}, 5 °
FURUNO FW-200	WIND SPEED, DIRECTION	ACASEX	1 ms^{-1}, 5 °
AANDERA 3145	AIR TEMPERATURE	M94,ACASEX	0.1 °C
PT-100	AIR TEMPERATURE	M95	0.1 °C
VAISALA HMP35D	RELATIVE HUMIDITY	M94,M95,ACASEX	1%
AANDERA 2810	AIR PRESSURE	M94,M95,ACASEX	0.2 hPa
SEACAT SBE 3	SST	M94,M95,ACASEX	0.01 °C

5.1.1.2 Air temperature

An Aandera 3145 platinum resistance sensor (M94, ACASEX) and a standard PT100 sensor (M95) were utilised for the DDS data (Table 5.1). The air temperature probes were housed in radiation shields.

Three-hourly observations of dry and wet-bulb temperatures were made by the South African Weather Bureau from two Yellow Springs Instruments (YSI) platinum resistance thermistors (Table 5.2) each housed in a Stevenson Screen. The Stevenson screen is a slatted white wooden box which is also designed to eliminate radiation errors. Resultant errors on the temperature sensors are associated with poor ventilation, ship exhaust heat contamination and sea spray contamination of the wet bulb temperature. Errors in results from psychrometers arise especially from errors in the wet-bulb temperature as a result of heat conduction, ventilation and sea salt contamination which tend to influence this sensor more (Fitschen and Gay, 1979).

Table 5.2: Instruments used for SAWB observations

MAKE AND MODEL	PARAMETER	DATASET	ACCURACY
YSI 44203	AIR TEMPERATURE	M94,M95	0.2 °C
YSI 44203	WET BULB TEMPERATURE	M94,M95	0.2 °C
VAISALA PA 11	AIR PRESSURE	M94,M95	0.3 hPa

5.1.1.3 Relative humidity

This was supplied by a Vaisala HMP35D relative humidity (RH) sensor housed in a radiation shield. This intrument utilises a HUMICAP, a thin-film capacitive sensor that has become a research standard Mesiä (1993).

5.1.1.4 Air pressure

Air pressure was supplied by an Aandera 2810 air pressure sensor.

5.1.1.5 Sea surface temperature

This was supplied by a Seacat SBE 3 located at the ship's water intake.

5.1.2 Methods

5.1.2.1 Humidity

Whilst the saturation water vapour pressure, es, is usually considered to be strictly a function of temperature, Buck (1981) described a small pressure enhancement effect. The enhancement correction, called the enhancement factor is made to correct for the very small pressure effect on water vapour. Buck (1981) suggested a suite of enhancement factors for varying meteorological ranges of interest. Bolton (1980) suggested a formulation for the saturation vapour pressure

$$es(T_a) = 6.112 \exp\left(\frac{17.67 T_a}{T_a + 243.5}\right)$$

(air temperature T_a in °C) is sufficiently accurate for most meteorological purposes.

The most appropriate enhancement factor (i.e. for the temperature range −20 to 50 °C) (Buck, 1981; Table 2) does not always encompass the full range of temperatures during rawinsonde ascents. At the surface where measurement errors may be large (eg. Fitschen and Gay, 1979) the achieved error reduction is insignificant. Therefore the formulation of Bolton (1980) is preferred over that of Buck (1981).

The water vapour pressure, e, in pascals is then found by

$$e = es(T_a)\frac{RH}{100}$$

where RH is the relative humdity.

The *mixing ratio*, r, in kg.kg^{-1} is the ratio of the mass of water vapour to the mass of dry air, and reduces to

$$r = 0.622\frac{e}{P - e}$$

(P in pascals) The specific humidity, q, in kg.kg^{-1} is the ratio of the mass of water vapour to the mass of moist air given by

$$q = 0.622\frac{e}{P - 0.378e}$$

The psychrometer-like arrangement of the SAWB is also used to calculate the water vapour pressure from

$$e = es(T_w) - 0.000660(1 + 0.00115T_w)(T_a - T_w)P$$

(P in pascals and T_a and T_w, the dry and wet-bulb temperature in $°C$) (Fitschen and Gay, 1979).

5.1.2.2 Surface fluxes of sensible, latent heat and momentum

Turbulent fluxes of momentum, sensible and latent heat are not measurable parameters but are derived from meteorological observations (wind speed, air and sea temperature and air humidity). The simplest method used to obtain the vertical turbulent fluxes of momentum heat and moisture at the surface of the marine atmospheric boundary layer is the *bulk aerodynamic method.* The turbulent fluxes are estimated with transfer coefficients which relate the fluxes to the means of routinely measured variables.

The bulk formulae for wind stress, sensible heat and water vapor fluxes are:

$$\tau = \rho_a C_D (U - U_s)^2 \tag{5.1}$$

$$Q_H = \rho_a c_p C_H (U - U_s)(T_s - \Theta) \tag{5.2}$$

$$Q_E = \rho_a C_E (U - U_s)(q_s - q) \tag{5.3}$$

where U, Θ and q are mean wind speed, potential temperature and specific humidity respectively measured at some reference height z_r. U_s is the sea surface current speed measured by an Acoustic Doppler Current Profiler (Rouault et al., 1996), $U - U_s$ is the magnitude of the wind speed relative to the sea surface (DeCosmo et al., 1996, p 12002; Geernaert et al., 1986, p 7671). C_D is the drag coefficient. C_H and C_E are the dimensionless Stanton and Dalton numbers, also called transfer coefficients for heat and water vapor. ρ_a is the air density. c_p is the specific heat of air at constant pressure.

$$\Theta = T_a + 0.0098 z_r \tag{5.4}$$

where T_a is the air temperature at z_r.

$$q_s = 0.98 q_{sat}(T_s) \tag{5.5}$$

T_s and q_s are mean sea surface temperature and specific humidity (assumed to be saturated) at the sea surface, qs is calculated from q_{sat} the saturation specific humidity at the surface: The factor 0.98 is introduced to account for the reduction in water vapor pressure due to salinity (Fairall et al., 1996).

In the lower part of the marine atmospheric boundary layer, the surface layer, (a few tens of meters), the turbulent fluxes are considered to be constant and the average values of wind speed, temperature and water vapor are expected to vary logarithmically with height. Thus the surface fluxes and scalar quantities for the surface layer can be derived from measurement of the meteorological parameters at only one height within this layer. The vertical profiles of wind velocity, temperature, and humidity above the oceans in the constant flux layer are (Stull, 1988):

$$\overline{U}(z) - U_s = \frac{u_\star}{\kappa}\left(\ln\frac{z}{z_0} - \phi_m\left(\frac{z}{L}\right)\right) \tag{5.6}$$

$$\overline{T}(z) - T_s = \frac{T_{v\star}}{\kappa}\left(\ln\frac{z}{z_{0T}} - \phi_T\left(\frac{z}{L}\right)\right) \tag{5.7}$$

$$\overline{q}(z) - q_s = \frac{q_\star}{\kappa}\left(\ln\frac{z}{z_{0q}} - \phi_q\left(\frac{z}{L}\right)\right) \tag{5.8}$$

where κ is the Von Karman constant and taken to be 0.4. $u_\star$, $T_\star$, $q_\star$ are the friction velocity and scaling parameter for temperature and water vapor. $u_\star$ is called the friction velocity, z_{0T} and z_{0q} are calculated as a function of the Reynolds number according to Liu et al. (1979) and modified by Fairall et al. (1996). z_0, the roughness length, reflects the roughness of the sea, and is related to the wave field using the relation of Smith (1988)

$$z_0 = 0.011u_\star^2/g + 0.11\nu/u_\star.$$

ϕ_m, ϕ_T, ϕ_q are determined empirically as a function of the stability parameter, $\zeta = z/L$. L is the Monin-Obukhov length.

$$L = \frac{T_v u_\star^2}{\kappa g(T_\star + 0.61Tq_\star)} \tag{5.9}$$

The stability parameter is analogous to the Richardson number, which is the ratio of the work done by the buoyant force to the rate of shear production of turbulent energy. It takes into account both the temperature and *moisture* dependence of air parcel buoyancy and is affected by the friction velocity, $u_\star$. The stability influences the vertical exchange of energy and momentum and thereby the vertical wind distribution in the boundary layer. The turbulent fluxes can be related to the scaling parameters $u_\star$, $T_\star$, $q_\star$ using the Monin-Obhukov similarity theory (Stull, 1988).

$$\tau = \rho_a u_\star^2 \tag{5.10}$$

$$Q_H = -\rho_a c_p u_\star T_\star \tag{5.11}$$

$$Q_E = -\rho_a L_V u_\star q_\star \tag{5.12}$$

L_v is the latent heat of vaporisation. Using the former equation one can express the transfer coefficients in the bulk formulation as:

$$C_D = \kappa^2 / \left(\ln \frac{z}{z_0} - \phi_m(\zeta) \right)^2 \tag{5.13}$$

$$C_H = \kappa^2 / \left(\left(\ln \frac{z}{z_{0T}} - \phi_T(\zeta) \right) \left(\ln \frac{z}{z_{0T}} - \phi_m(\zeta) \right) \right) \tag{5.14}$$

$$C_E = \kappa^2 / \left(\left(\ln \frac{z}{z_{0q}} - \phi_q(\zeta) \right) \left(\ln \frac{z}{z_{0q}} - \phi_m(\zeta) \right) \right) \tag{5.15}$$

One can calculate the surface fluxes using equation (5.1), (5.2), (5.3) and (5.13), (5.14), (5.15) with an iterative process, starting with an arbitrary value of the flux corresponding to neutral atmospheric stability to obtain an estimate of the Monin-Obukhov length (5.9) and the stability parameter. From this, the transfer coefficients and the fluxes are recalculated and reentered into the iterative process. A solution is obtained after a few iterations. The algorithm developed by Fairall et al. (1996) for the TOGA-COARE experiment is used here. It includes a separate module to calculate the real sea surface temperature (skin temperature) from the measured sea surface temperature which is usually the temperature of the ship intake a few metres below the surface. Scenarios such as light winds, actively convective regimes and rain which are not covered by traditional bulk models, are accounted for in this algorithm.

The parameters necessary for the bulk flux calculations were averaged over 10 minutes before applying the bulk formulae. Estimation of fluxes with the bulk method shows great variability depending on the accuracy of the measurement devices, the flow distortion generated by the ship and the accuracy of the exchange coefficients used (Blanc, 1985; Blanc, 1987). The accuracy of a bulk-derived $u_\star$ and roughness length may be questionable in regions of strong surface currents. Current speeds of up to 2 ms^{-1} were measured during ACASEX (Rouault et al., 1995).

5.2 Upper-air data

5.2.1 Data and Instrumentation

Stull (1988) has defined *radiosondes* as free balloons that measure temperature, humidity and pressure only whilst *rawinsondes* also provide wind information via a tracking system. This definition will be used.

Boundary layer characteristics in this study are provided by rawinsonde ascents. Whilst rawinsondes provide high vertical resolution compared to aircraft they will sample the local mixed layer top (not necessarily equal to the average mixed layer top) (Stull, 1988; p 474). Furthermore a rawinsonde does not necessarily represent a vertical spot measurement as it will advect with the mean wind.

The Vaisala RS80 Omega Sounding System provided the vertical profiles of *wind speed* and *direction*, *temperature* and *relative humidity*. During M94 rawinsonde ascents were undertaken on a twelve-hourly basis (twice-daily). During M95 ascents were released aproximately three to six-hourly. During ACASEX ascents were chosen to coincide with the region of interest.

It is unfortunate that, until 1995, the system of rawinsonde data capture used was designed for operational forecast purposes only. The result has been a vertical spatial data sparseness (about 10 values for the first 3000 m) which was suitable for forecast purposes but less than ideal for investigating boundary layer dynamics. In most cases, however, the data have been sufficient to delineate the surface layer, the inversion height and the mean characteristics of the atmospheric mixed layer. This low resolution data applies only to M94. Thereafter, we were able to persuade the SAWB to modify their data capture system. The refinement has since been implemented and vertical resolution is now on the order of 4 mb (roughly 50 m to 60 m).

Rawinsonde wind data from M95 and ACASEX was rejected. M95 wind data was found to be unrealistic (due to a software problem). During ACASEX water entered the housing enclosing the tracking antenna pre-amp with the result that the tracking signal could not be received.

5.2.2 Methods

5.2.2.1 Virtual Potential Temperature

Buoyancy is one the driving forces for turbulence in the boundary layer. The virtual temperature of a moist air parcel is the temperature of a dry air parcel which has the same density. It takes into account the water vapour effect on air parcel density. Thus variations of virtual temperature can be studied in place of variations in density. The study of virtual potential temperature is not just an attractive but necessary means of describing the structure of boundary layer (Stull, 1988).

The virtual potential temperature (in Kelvin) for unsaturated air is (after Stull, 1988; Appendix D)

$$\theta_v = \theta(1 + 0.61r)$$

and for cloudy air

$$\theta_{vc} = \theta(1 + 0.61r - r_L)$$

where the liquid water loading r_L, the ratio of the mass of *liquid water* to the mass of dry air, serves to reduce the virtual potential temperature.

The potential temperature θ is defined by

$$\theta = T_K \left(\frac{P_0}{P}\right)^{0.286}$$

where T_k is the air temperature in Kelvin, P_0 and P the air pressures in pascals at the surface and reference level P. Potential temperature is conserved during dry adiabatic processes. An air parcel sinking dry adiabatically from some reference level P will warm according to the dry adiabatic lapse rate before attaining a temperature θ at P_0 (Preston-Whyte and Tyson, 1988; p 21).

The (unsaturated) virtual potential temperature will be used to describe the nature of the boundary layer. The cloudy virtual potential temperature will be used to compare model cloud densities to the environmental density. The mixed layer (with top z_i) will be defined as the layer above the surface where the virtual potential temperature profile is approximately adiabatic. The convective boundary layer (CBL) is defined (after Betts and Albrecht, 1987) as the layer above the surface that is convectively coupled to the surface. This includes the surface layer, mixed layer and entrainment zone.

5.2.2.2 Equivalent Potential Temperature

The equivalent potential temperature, θ_e, is especially useful as a tool in conserved variable analysis and diagnosing the origin of airmasses (Betts and Albrecht, 1987, Section 5.2.2.4). This is defined by Holton (1972) as the final temperature attained when a parcel is lifted dry adiabatically to its saturation level, then pseudo-wet adiabatically until all its condensate has precipitated before finally descending dry adiabatically to the surface. θ_e is the final temperature of an air parcel if it is lifted until all of its water vapour is given up to latent heat and it is then brought to the surface.

The method of Bolton (1980) will be used to calculate θ_e. The *lifting condensation level*, T_L the temperature an air parcel would attain when lifted dry adiabatically to its condensation level is found by

$$T_L = \frac{1}{\frac{1}{T_K - 55} - \frac{\ln(RH/100)}{2840}} + 55$$

The equivalent potential temperature is then

$$\theta_e = \theta \exp\left[\left(\frac{3.376}{T_L} - 0.00254\right) \times r\left(1 + 0.81 \times 10^{-3} r\right)\right]$$

5.2.2.3 Boundary layer quantification

In order to describe the mean scalar quantities of the boundary layer the following two properties are defined (after Katsaros et al. (1994))

$$\overline{\theta}_e = 1/z_i \int_0^{z_i} \theta_e(z)\, dz$$

$$\overline{q} = 1/z_i \int_0^{z_i} q(z)\, dz$$

where z_i is the mixed layer height. When the boundary layer was not actively convective, a residual layer (Stull, 1988; p 14) was identifiable. The top of the residual layer was then taken as the limit of integration. When the boundary layer was stable there was no defined boundary layer top. In this case the inversion was chosen as the limit of integration.

Changes in $\overline{\theta}_e$ and $\overline{q}$ along an atmospheric trajectory over short time intervals are due to turbulent surface fluxes and entrainment.

5.2.2.4 Conserved variable analysis

A conserved variable diagram is a plot of one conserved variable against another (Stull, 1988; p 548). A particularly useful conserved variable diagram is the $\theta_e - r_T$ plot (Betts and Albrecht, 1987, Figure 5.1). For unsaturated air, this reduces to a $\theta_e - r$ plot. Mixing lines are straight lines on this diagram, advective processes do not move parcel points and radiative and precipitation processes are easily identifiable (Betts and Albrecht, 1987; p 85).

Betts and Albrecht (1987) have discussed how mixing, precipitation and radiative cooling move parcel points on this diagram. Precipitation moves parcel points to a lower r_T at constant θ_e, the radiative process does not change r_T but radiative cooling will move a point to a lower θ_e at constant r_T. Mixing lines are straight lines on this diagram.

The convective boundary layer profiles were classified according to synoptic conditions and composited. A simple averaging technique was used which has the effect of eliminating kinks but also smoothing repeated features.

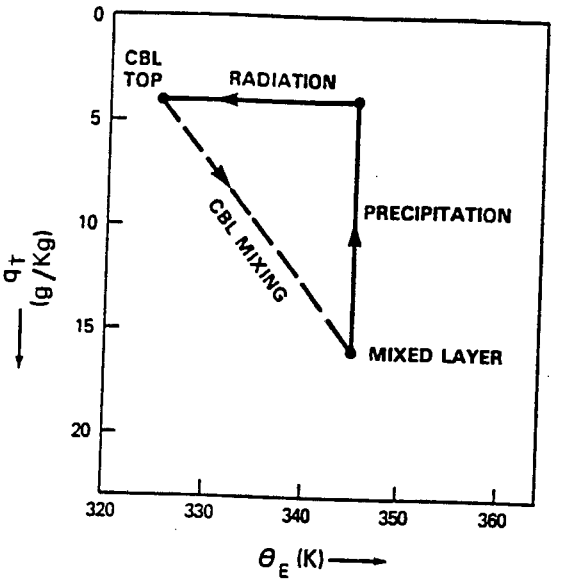

Figure 5.1: Schematic of $\theta_e - r$ diagram showing mixing line, effect of precipitation and radiative cooling on an air parcel saturation point (after Betts and Albrecht, 1987). The authors have used the symbol q for the mixing ratio.

5.2.2.5 Convective available potential energy

Cloud convective available potential energy was calculated to illustrate potential cumulus formation and decay. The cloud convective available potential energy (CAPE) is (Stull, 1988)

$$CAPE = \int_{z=z_{LFC}}^{z_{LOC}} \frac{g}{\theta} \Delta\theta_v(z)\, dz$$

where

$$\Delta\theta_v = \theta_{vcloud} - \theta_{venviron}$$

The cloud temperature can be estimated by assuming dry adiabtic ascent from the surface until the lifting condensation level, T_L (a good approximation for cloud base), and wet adiabatic ascent thereafter until the limit of convection (LOC). The mixing ratio was considered to be everywhere saturated within the cloud. The liquid water mixing ratio, r_l was calculated from the liquid water mixing ratio lapse rate $\Gamma_l = \frac{dr_l}{dz}$ (Albrecht et al., 1990).

$$\Gamma_l = -\frac{dr_s}{dz} = \frac{(0.622 + r_s)\, r_s L_v}{R_d T a^2} \Gamma_W - \frac{r_s P}{P - e_s} \left(\frac{g}{RdT_a} \right)$$

L_v is the latent heat of vaporisation. R_d is the specific gas constant for dry air and Γ_W is the wet adiabatic lapse rate calculated from Betts and Bartlo (1991). The liquid water mixing ratio may be assumed to vary linearly with height for thin clouds (Albrecht et al., 1990).

$$r_l = \Gamma_l (z - z_B)$$

For deeper clouds this assumption is unreasonable. Therefore the liquid water content was calculated as an integral.

This gives a theoretical upper limit on CAPE. However, many convective thermals have undiluted cores allowing the actual cloud base to be close to the lifting condensation level calculated from surface-layer air (Stull, 1988; p 551). Calculation of CAPE is highly sensitive to the humidity of the air parcel at its initial level since this affects the value of T_L and the resultant air parcel trajectory.

5.2.2.6 Precipitable water content

The precipitable water content (also known as the total water path) was analysed to determine synoptic variations and the contribution of the moisture in the boundary layer to this quantity. The water vapour path (given in metres) is

$$(\Delta z)_v = \frac{1}{\rho_l} \int_0^{ztop} \rho_a(z)\, r(z)\, dz$$

where ρ_l and ρ_a are the densities of water and dry air respectively. The latter is a "partial density" (Stull, 1988).

$$\rho_a = \frac{P - e}{R_d T_a}$$

Boundary layer estimates of $(\Delta z)_v$ were obtained by choosing $ztop = z_i$.

The liquid water path (given in metres) is

$$(\Delta z)_l = \frac{1}{\rho_l} \int_0^{ztop} \rho_a(z)\, r_l(z)\, dz$$

where r_l is the liquid water mixing ratio obtained assuming wet adiabatic ascent above cloud base. Following Betts and Albrecht (1988), cloud base was chosen as the saturation level of air at the base of the mixed layer. Cumulus clouds have a liquid water profile that is rarely adiabatic. Observations for these clouds show that the true liquid water content occurs as a fraction of its adiabatic value (Warner, 1970). Therefore the liquid water profile, r_l, was adjusted to a fraction of its adiabatic value using Warner (1970, Table 1).

Chapter 6

Results and Discussion

6.1 Intercomparison of results

Before describing the surface turbulent fluxes it is necessary to determine the degree of confidence that may placed in each dataset. An intercomparison of the automatic data with the additional measurements made during M94, M95 and ACASEX led to the rejection of M95 surface data. Here the values obtained from the automatic measurement are compared with those of the manned SAWB operation (M94 and M95) and with other measurements (ACASEX).

6.1.1 M94

The parameters of air temperature, relative humidity and wind speed are compared. It should be noted that the SAWB relative humidity is an indirect comparison and is dependent on the accuracy of the SAWB dry and wet-bulb temperatures. Since there is a mismatch of time scales (i.e. 1 minute vs 3 hours) the automatic (DDS) data is averaged for a ten minute period. Ten minutes averaging periods are chosen to coincide with those times corresponding to SAWB observations (i.e. once every 3 hours). The resultant data set is small (n=57) and statistically limited. The results are shown in Figure 6.1 (data plotted as crosses). Root mean squared (RMS) differences of air temperature (Δ_{Ta}), relative humidity (Δ_{RH}) and wind speed (Δ_U) are 0.5 °C, 8% and 1.4 ms^{-1}. Investigating the differences as possible calibration drifts yielded no clear results. Wind speed values for the SAWB and DDS are derived from the same instrument (Koshin-Vane) and yet discrepancies of over 4.5 ms^{-1} are apparent. This is not a problem of averaging as a comparison of instantaneous values for all parameters (Figure 6.1, data plotted as circles) yields similar results. The problem is one of sampling. Although SAWB values are

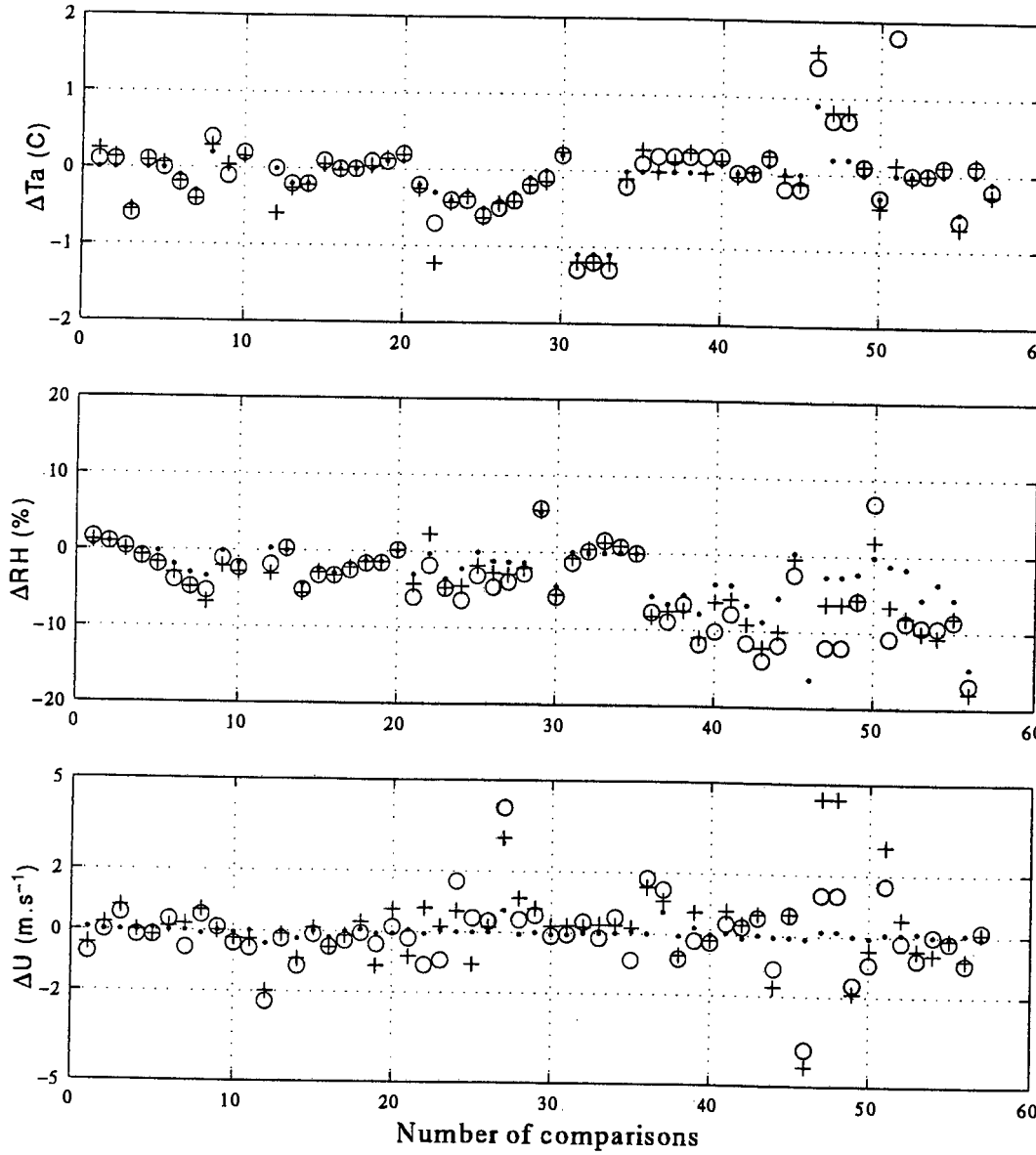

Figure 6.1: Comparison of DDS and SAWB values - M94. The comparisons are plotted as differences (DDS value - SAWB value). From top to bottom: ΔT_a, ΔRH and ΔU. Instantaneous ($\circ$), bulk ($+$) and minimum possible ($\cdot$) differences are shown.

intended to be representative of mean conditions they are instantaneous values. In order to demonstrate this, for each SAWB reading a twenty minute window of DDS data (10 minutes either side of the SAWB reading) was constructed. Each DDS reading within this window was compared to the SAWB reading to yield a minimum possible difference. This was done for all SAWB readings. This minimum possible difference is plotted (as dots) in Figure 6.1. Root mean squared differences in T_a, RH and windspeed reduce to 0.5 °C, 6% and 0.2 ms^{-1} respectively. This discussion demonstrates discrepancies between actual bulk-averaged data and instantaneous data meant to be representative of bulk averages.

Since relative humidity differences cannot be explained as a sampling problem this was investigated further. Figure 6.2 shows a comparison of vapor pressures.

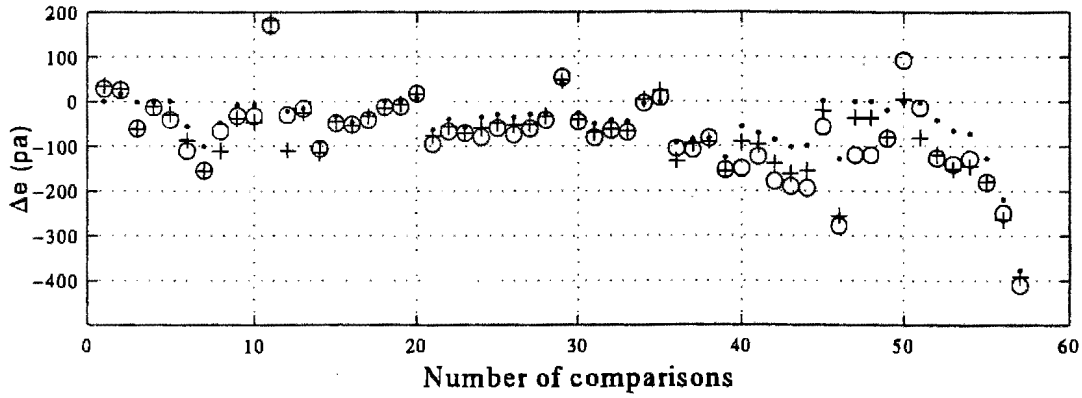

Figure 6.2: Comparison of DDS and SAWB vapor pressures - M94. The comparisons are plotted as differences (DDS value - SAWB value). Instantaneous (o), bulk (+) and minimum possible (·) differences are shown.

RMS(Δ_e) is reduced from 117 pascals (pa) (1 minute instantaneous comparison) to 82 pa using the sliding window comparison. In general vapor pressure calculated from the Vaisala RH shows an underestimation relative to the vapor pressure calculated from the SAWB dry and wet-bulb temperatures (psychrometer). The scatter in vapor pressure is seen to increase toward the end of the record. Data for n$\geq$50 corresponds to the end of the cruise and was not considered for analysis. By excluding data for n$\geq$50 RMS(Δ_e) is reduced again from 98 pa (1 minute instantaneous comparison) to 58 pa using the sliding window comparison. Whilst a RMS(Δ_e)=58 pa is a vast improvement it is clear that random sampling errors cannot explain the large Δ_e values.

Errors in vapour pressure calculated from a psychrometer may arise from several sources

(Fitschen and Gay 1979). Errors in air pressure may cause small errors in the vapor pressure. A comparison of ambient air pressure showed close agreement apart from some obvious random errors in the SAWB air pressure. These could be identified easily (for example an air pressure of 1016.0 hPa was recorded as 1001.6 hPa). Eliminating these errors yielded good agreement. The vapor pressure comparison in Figure 6.2 reflects this correction. Psychrometer errors are mainly associated with wet-bulb temperature errors such as conduction, radiation, poor ventilation and sea salt contamination which all serve to cause the indicated vapor pressure to exceed the true vapor pressure (Fitschen and Gay, 1979). This agrees qualitatively with the relative overestimation of the the vapor pressure and specific humidity by the SAWB psychrometer. Ship heat exhaust contamination is likely to have affected the psychrometer far more due to the positioning of the instruments. Investigation of the vapor pressure discrepancy as a systematic function of poor ventilation and/or an overestimation of wet-bulb temperature gave only a marginal improvement.

The small sample precludes a detailed analysis here. A bulk average comparison of the specific humidity differences gives (for n<50) a RMS(Δ_q)=0.7 gkg^{-1} (which is subject to the sampling errors discussed above).

6.1.2 M95

A comparison of bulk air temperature differences (n=59) (Figure 6.3, data plotted as crosses) shows a large amount of scatter and no discernible pattern. Investigating the discrepancies as random sample errors (Figure 6.3, data plotted as dots) did not show an improvement. Without exception, the automatic air temperature readings show a relative overestimation of the air temperature.

It has been confirmed that for M95 the SAWB air temperature underestimated the true dry bulb temperature (Sidney Marais, South African Weather Bureau; personal communication). This was demonstrated by comparing dry bulb readings of the (original) wet-bulb temperature probe and an additional air temperature probe to the existing dry bulb temperature probe. The existing dry bulb probe was shown to underestimate the air temperature.

This underestimation has been investigated here (not shown) as a possible systematic error as a function of ventilation, ship heat exhaust contamination depending on the wind orientation and of air temperature. A cursory glance at Figure 6.3 indicates that the random scatter mitigates against any such relationship. It is therefore not possible to make any conclusion about the reliability of the automatic air temperature reading (a PT100 probe). The degree

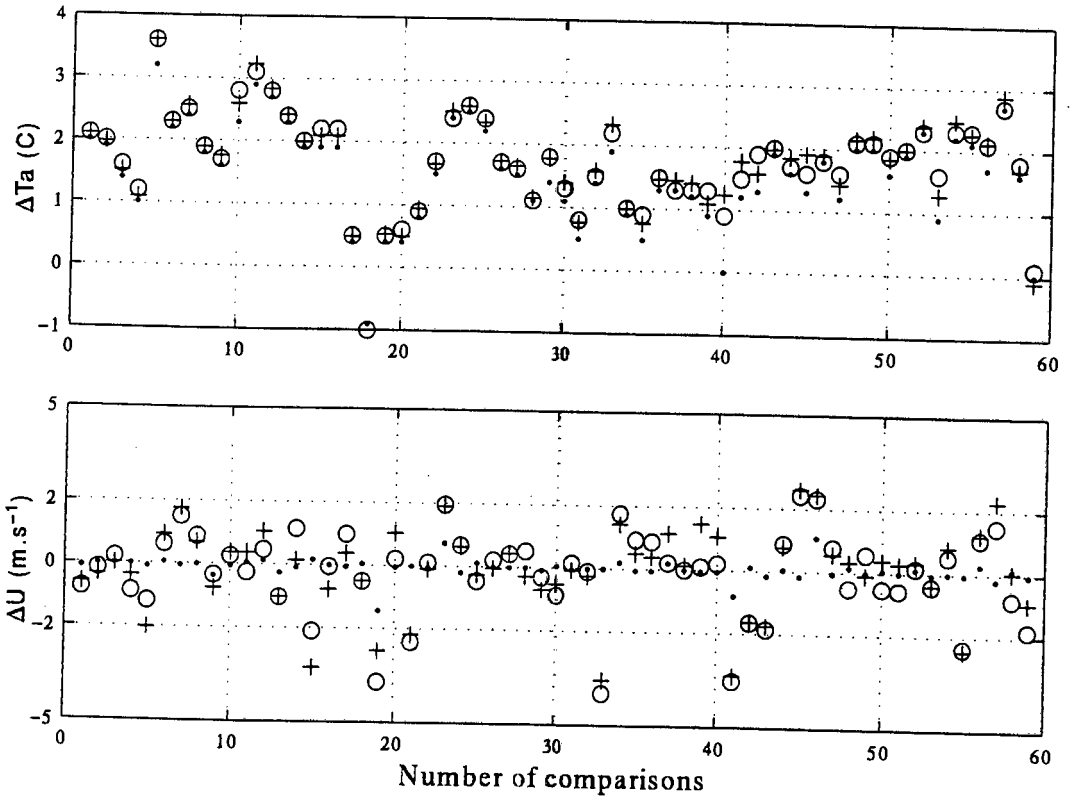

Figure 6.3: Comparison of DDS and SAWB values - M95. The comparisons are plotted as differences (DDS value - SAWB value) from top to bottom: ΔT_a and ΔU. Instantaneous (o), bulk (+) and minimum possible (·) differences are shown.

of scatter suggests that it too may be unreliable. It is for this reason that all air temperature and humidity data from this dataset was rejected with the result that no surface fluxes could be computed.

6.1.3 ACASEX

A variety of instruments were available for comparison during the ACASEX cruise (Rouault et al., 1996). DDS wind speed measured using a Furuno FW-200 aerovane gave good agreement with a GILL Instruments sonic anemometer.

The DDS air temperature was found to exceed the true air temperature by 1.9 °C and could be corrected. The Vaisala relative humidity was compared to that of an Ophir IR-2000 hygrometer. This comparison was complicated by the fact that the IR-2000 air temperature was not stable and tended to drift. An additional difficulty is that the Vaisala is calibrated for relative humidity whilst the IR-2000 is calibrated for absolute humidity. Reasonable agreement was obtained (Rouault et al., 1996).

6.2 Agulhas Retroflection Region

Datasets M94 and M95 are considered here. Schematics of the ship tracks can be found in Figures 6.4 and 6.5.

6.2.1 Meteorological setting.

A variety of synoptic types were encountered during the two cruises. Air-sea transfer processes, boundary layer characteristics and modification under each synoptic type was investigated. The three synoptic situations to be considered are *anticyclonic*, *frontal*, and a *cold-air outbreak*

6.2.2 Air-sea fluxes of momentum, sensible and latent heat

6.2.2.1 Anticyclonic conditions

During the forward leg of the 1994 Marion voyage the ship traversed the Agulhas Retroflection Region (ARR) and Sub-Tropical Convergence (STC) (Figure 6.4). A slow moving, transient anticyclone was displaced unusually far south (Figures 6.6 and 6.7) and provided synoptic conditions that were nearly stationary. Fair weather conditions and easterly to northeasterly winds prevailed. Over the Agulhas Return Current (ARC) cumulus towers were observed. The fluxes

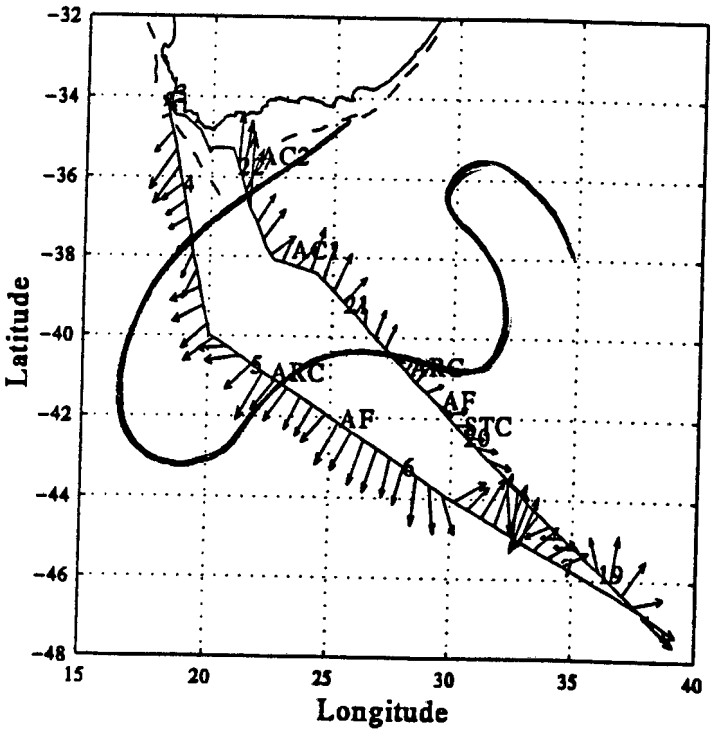

Figure 6.4: M94 - Schematic of the ship track and the geographical disposition of the Agulhas Current as determined from a satellite SST composite. Numbers indicate the ship's position on the eve of those dates. Wind vectors (plotted two-hourly) are shown. Labels denote the positions of atmospheric profiles found in Figures 6.19 and 6.23. Atmospheric profiles at AC1 and AC2 were used to construct the composite in Figure 6.18. Since very few cloud-free days occurred the composite has been constructed from a number of SST images spanning the entire duration of the cruise. The thermal envelope depicted here is thus only approximate.

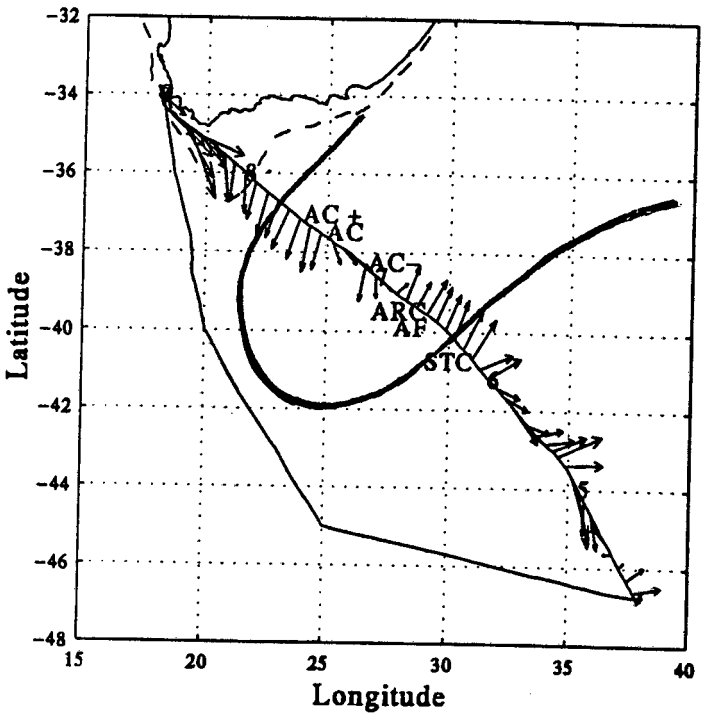

Figure 6.5: M95 - Schematic of the ship track and the geographical disposition of the Agulhas Current as determined from SAWB SST maps (no cloud-free satellite images were available). The thermal envelope depicted here is only approximate. The ship skirted the western boundary of the ARR during the advance leg. Dates for the advance leg are not shown since this portion was not considered for analysis. Labels denote the positions of atmospheric profiles found in Figures 6.21 and 6.22.

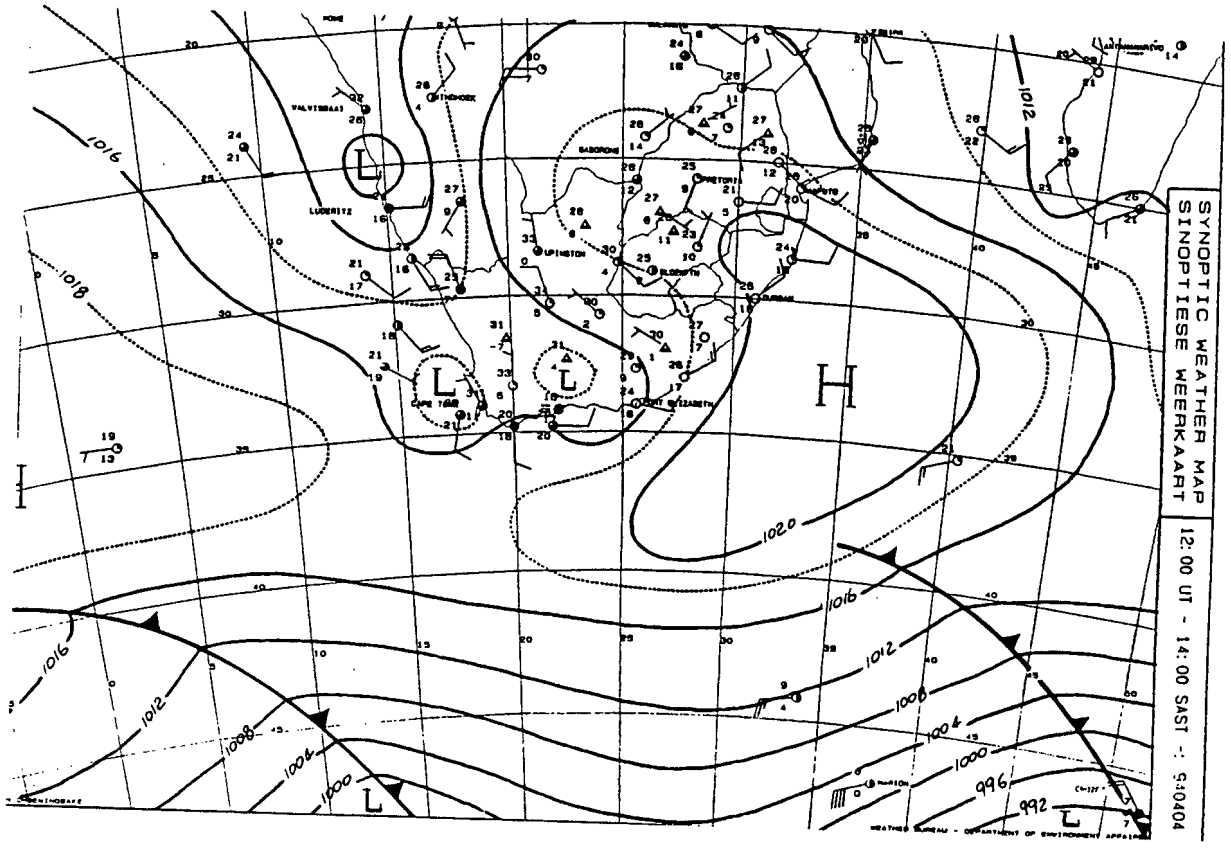

Figure 6.6: SAWB synoptic chart - 4 May 1994.

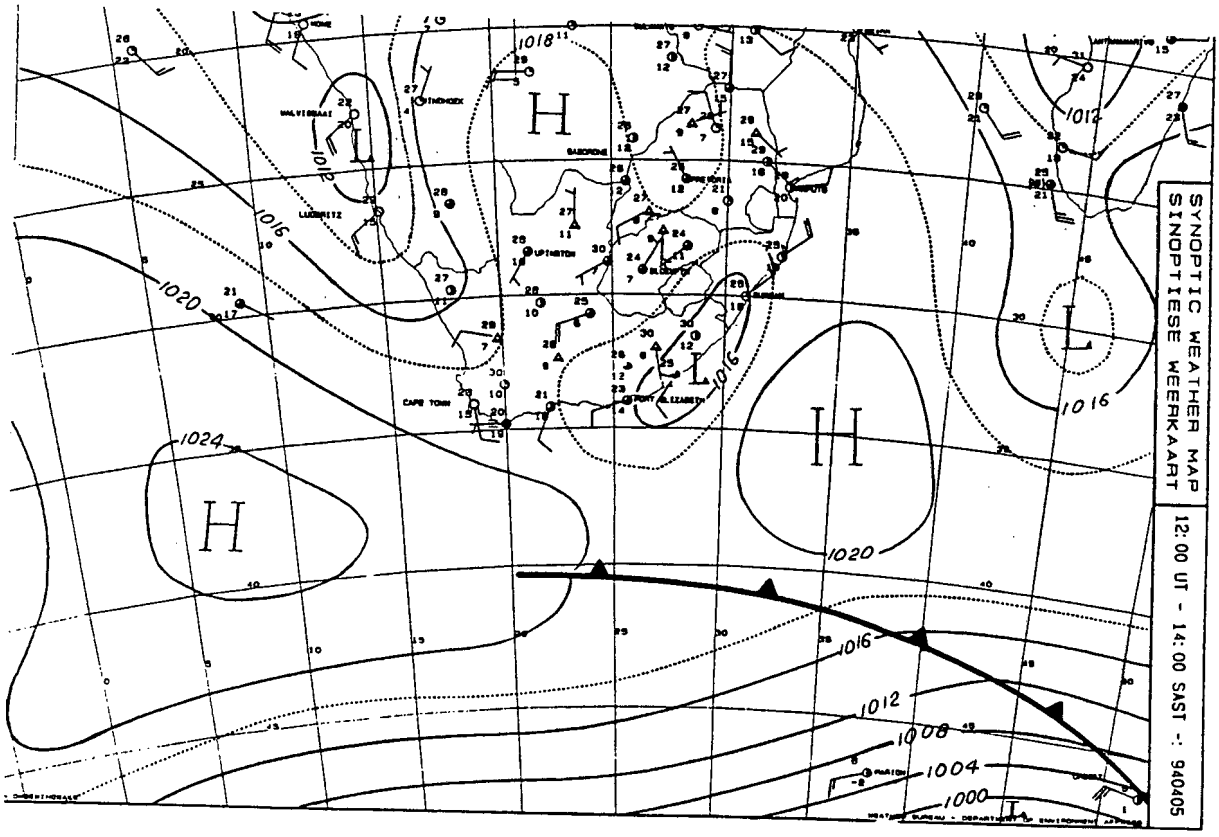

Figure 6.7: SAWB synoptic chart - 5 May 1994.

and forcing parameters of interest are shown in Figure 6.8. A loss from the ocean of sensible and latent heat is plotted as a positive flux. The momentum flux is always downward (plotted here also as a positive flux). Wind speed, air temperature and specific humidity reported at the standard height of 10 m, are calculated from the bulk algorithm The time series begins near the northern border of the ARR and ends at the STC (Figure 6.4).

Surface fluxes demonstrate fairly high short-term variability. Air-sea gradients of T_a, q and U are initially small. Surface heat fluxes increase towards the core of the current and decrease rapidly toward the STC. The latent heat flux is almost exclusively responsible for the total heat flux (Table 6.1) and doubles over the Agulhas Return Current as maximum air-sea gradients of T_a and q are realised. It is likely that this air has only recently been modified by Agulhas Return Current waters (Figure 6.4). The increase in surface fluxes is expected to destabilise the surface layer and mix high-momentum air from above toward the surface. Indeed the response of the wind is abrupt and a tripling of the wind stress occurs. The response is discontinuous and lags the surface heat flux increase. It is however, also possible that this feature is related to a strengthening of the surface pressure gradient (Figures 6.6 and 6.7)

The transition from the Agulhas Return Current to the STC is defined by a broad SST front known as the Agulhas Front (AF). A commensurate decrease in surface fluxes is realised.

An interesting mesoscale feature is defined by a sharp jump in SST on the eve of 5 May. The SST at the core is 20 °C. Assuming that the ship covered the longest possible length then its maximum diameter is estimated at 43 km. This is a conservative estimate at best. Most likely this is an Agulhas Current Retroflection eddy. Eddies in this region have diameters of approximately 200 km (Lutjeharms and Valentine, 1988). Surface fluxes respond dramatically and winds increase by some 5 ms^{-1} and tail off on the periphery of the eddy. The mesoscale response of the wind is aptly demonstrated. Thereafter the SST declines steadily. Surface fluxes beyond the STC do little to destabilise the boundary layer and free convection is minimised.

The strong anticyclonic forcing resulted in low surface heat fluxes (Table 6.1). Averages here refer to that portion of the data sample coinciding with the warm waters of the ARR (i.e north of the Agulhas Front).

Surface stability as given by the Monin-Obhukhov stability parameter $\zeta_{10} = 10/L$, is dominated by the friction velocity u_* and is hence always near-neutral to slightly unstable ($\overline{\zeta}_{10} = -0.37$). It is important to note that ζ is not an absolute measure of instability since it is influenced by the friction velocity u_*.

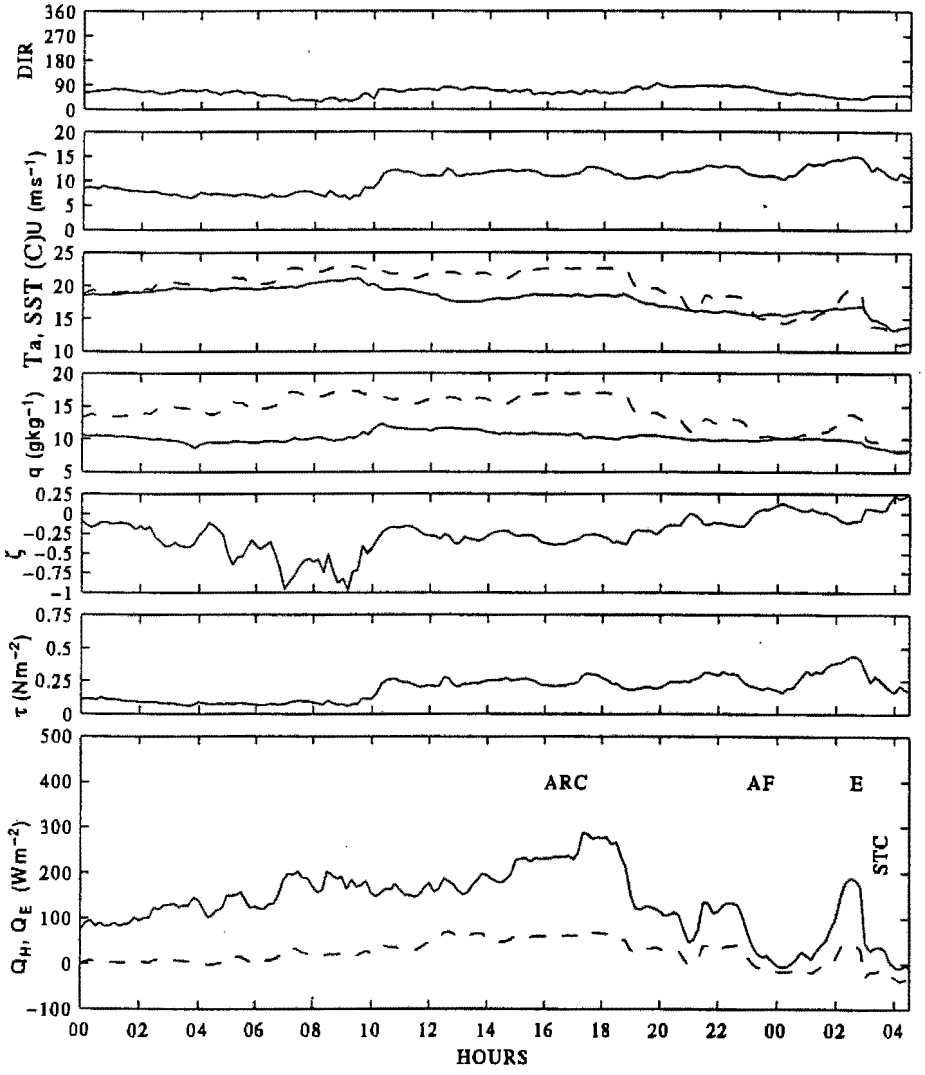

Figure 6.8: Time series of fluxes and parameters of interest for the advance leg - M94. The parameters (from top to bottom) are: wind direction; wind speed (U) at 10 m; air temperature at 10 m (-) and sea surface skin temperature (- -); specific humidity at 10 m (-) and saturation specific humidity at the sea surface (- -); stability parameter, $\zeta_{10} = 10/L$ (-); wind stress(-); latent heat flux (-) and sensible heat flux (- -). The time series begins on 4 May and ends on the morning of 5 May. The positions of the Agulhas Return Current (ARC), Agulhas Front (AF), warm-cored eddy (E) and Subtropical Convergence (STC) are shown.

Table 6.1: Air-sea flux statistics - M94. The quantities dQ_T/dy, and $dSST/dy$ are the horizontal gradients of the total heat flux and sea surface temperature perpendicular to the Agulhas Front and apply only to the anticyclonic and transient frontal cases.

SYNOPTIC TYPE	$\overline{\tau}$	$\overline{Q}_H$	$\overline{Q}_E$	$\overline{Q}_T$	$max(Q_T)$	$\overline{\zeta}_{10}$	dQ_T/dy	$dSST/dy$
	$N.m^{-2}$	$W.m^{-2}$					$W.m^{-2}km^{-1}$	$°Ckm^{-1}$
ANTICYCLONE	0.15	30	164	194	359	-0.37	1.6	0.05
TRANSIENT FRONT	0.06	41	145	186	500	-2.55	3.2	0.07
COLD-AIR OUTBREAK	0.23	109	307	416	628	-0.95	-	-

6.2.2.2 Transient front

During the return leg of the 1994 Marion voyage the ship traversed the Agulhas Front and entered over the Agulhas Return Current (Figure 6.4). Weak meteorological pre-frontal and frontal conditions prevailed (Figure 6.9) on 20 May.

The time series (Figure 6.10) begins in the region of the STC. The transition to the warm Agulhas Return Current is again defined by a number of step-like SST increments superimposed on a more intense Agulhas Front. The wind is from the west and is almost parallel to the Agulhas Front. Short term variability of the fluxes is again apparent. It is clear that mesoscale variations in the surface fluxes correspond to mesoscale undulations in the SST with small superimposed perturbations. Over the main SST front, surface heat fluxes are seen to increase dramatically from a negligible amount to over 200 $W.m^{-2}$. Surface conditions are unstable ($\overline{\zeta}_{10} = -2.55$ with light winds). Despite exhibiting greater variability, mean oceanic heat losses are very close to those for anticyclonic conditions (Table 6.1).

6.2.2.3 Cold-air outbreak

On 21 May strong synoptic forcing saw a ridging anticyclone sweep in cold post-frontal conditions over the ARR (Figure 6.11) in a short-lived "cold air outbreak" during strong southerly flow. Cold-air outbreaks are normally associated with zonal offshore flow of continental air during the post-frontal stage (Bane, 1989). In contrast, cold-air outbreak over the ARR may be associated with strong anticyclonic ridging behind a transient cold front. Considerable heat and moisture uptake occur as air is advected meridionally toward the subcontinent.

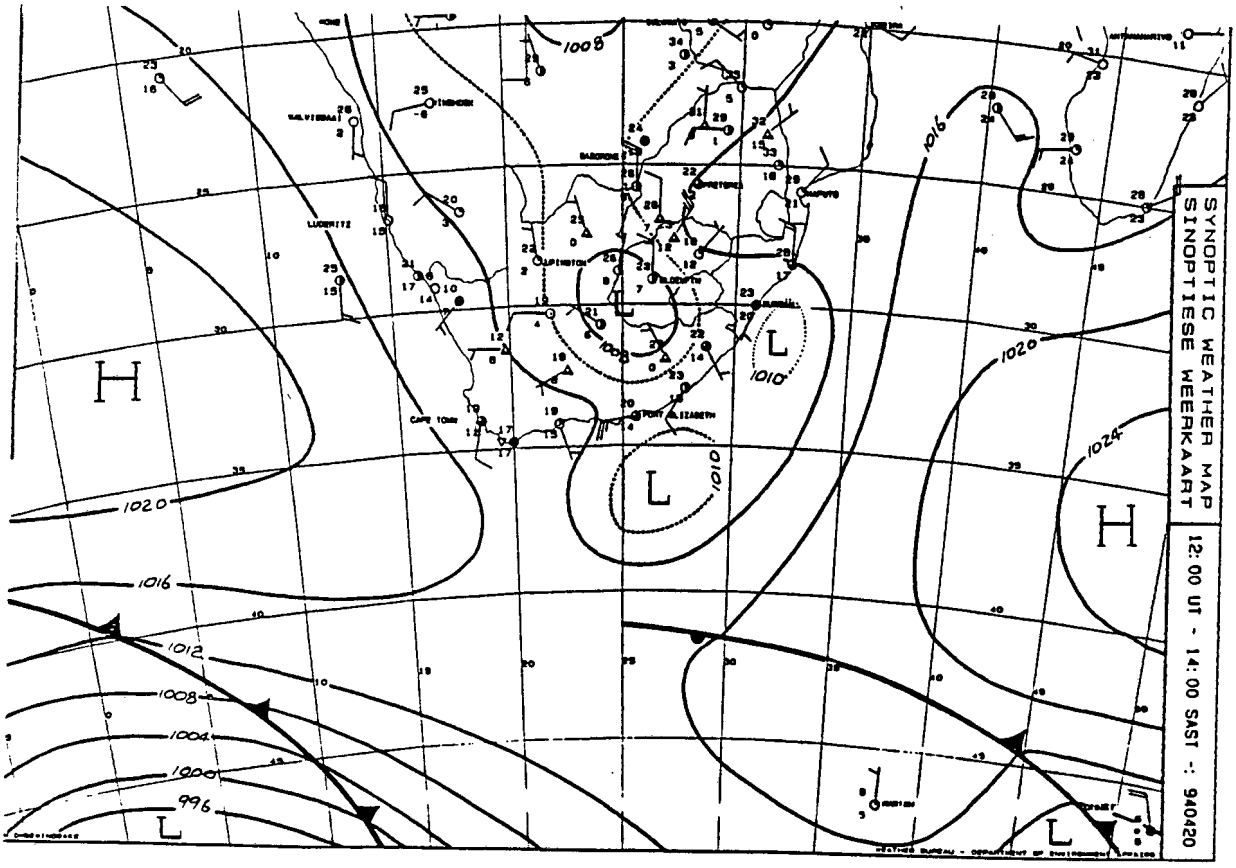

Figure 6.9: SAWB synoptic chart - 20 May 1994.

Discontinuous jumps in the surface heat flux correspond initially to minor SST fronts and are superimposed on the overall increase in fluxes (Figure 6.10). The latter is attributed to the warmer SST and changing airmass characteristics. The gentle decrease of T_a is an indication that the airmass became more sub-polar. The short term variability of the fluxes increases dramatically as large air-sea temperature and humidity differences create a highly thermally unstable environment. It is during this period that maximum oceanic heat losses of 628 W.m^{-2} were attained. Large perturbations in the surface fluxes are unrelated to SST variations.

Turbulent air-sea transfer processes are very different from the previous two cases (anticyclone and transient front). The surface layer is unstable ($\overline{\zeta}_{10} = -0.95$ with strong winds) as free surface convection is intiated.

6.2.3 Convective boundary layer mean thermodynamic structure

The convective boundary layer over the ocean plays an important role in regulating the upward transfer of heat and moisture. (Betts and Albrecht,1987). In this section conserved variable analysis is used to describe the mean thermodynamic structure of the convective boundary layer. The mean thermodynamic structure is expected to be a function of the surface turbulent fluxes and synoptic conditions.

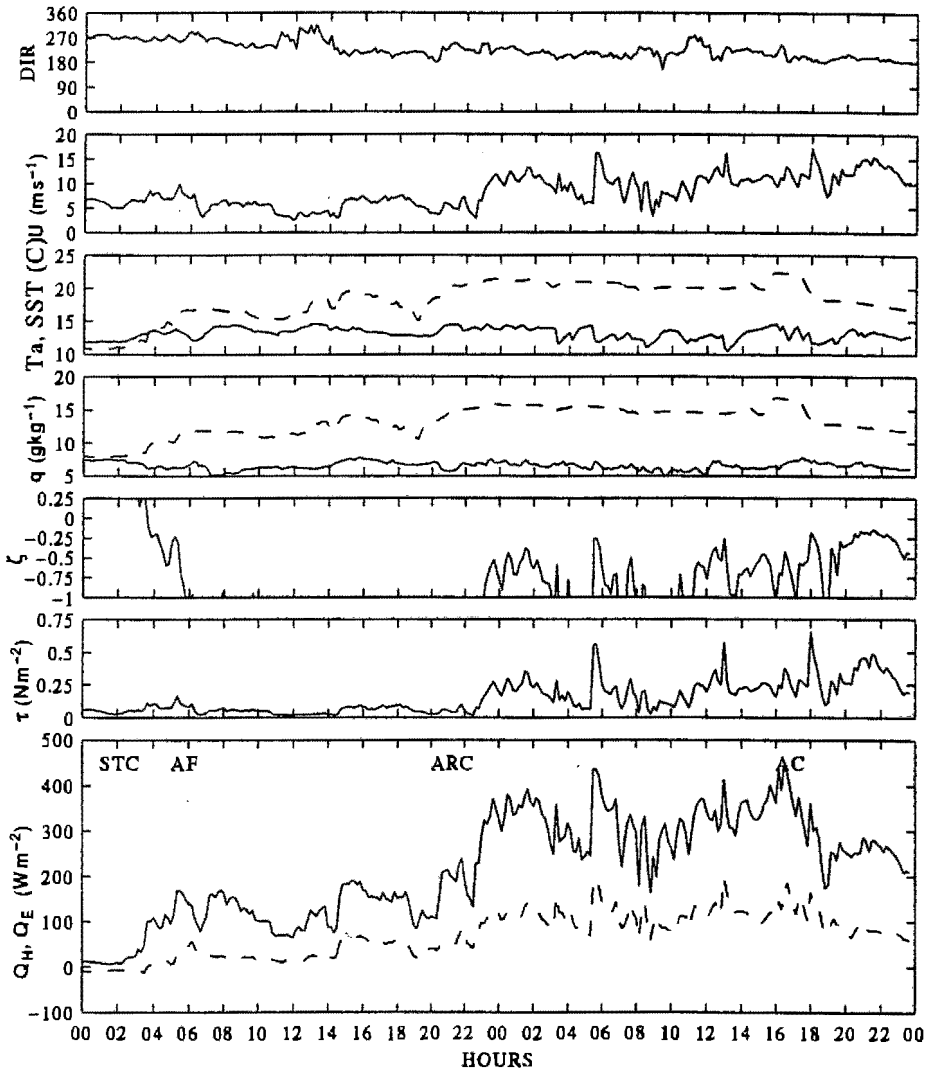

Figure 6.10: Time series of fluxes and parameters of interest for the return leg - M94 - during the transient frontal and cold-air outbreak cases. Parameters as for Figure 6.8. The time series begins on the morning of 20 May and ends at midnight on 21 May. The transient frontal and cold-air outbreak cases correspond to the 20 May and 21 May repectively. The positions of the Agulhas Front (AF), Agulhas Return Current (ARC) and Agulhas Current (AC) are shown.

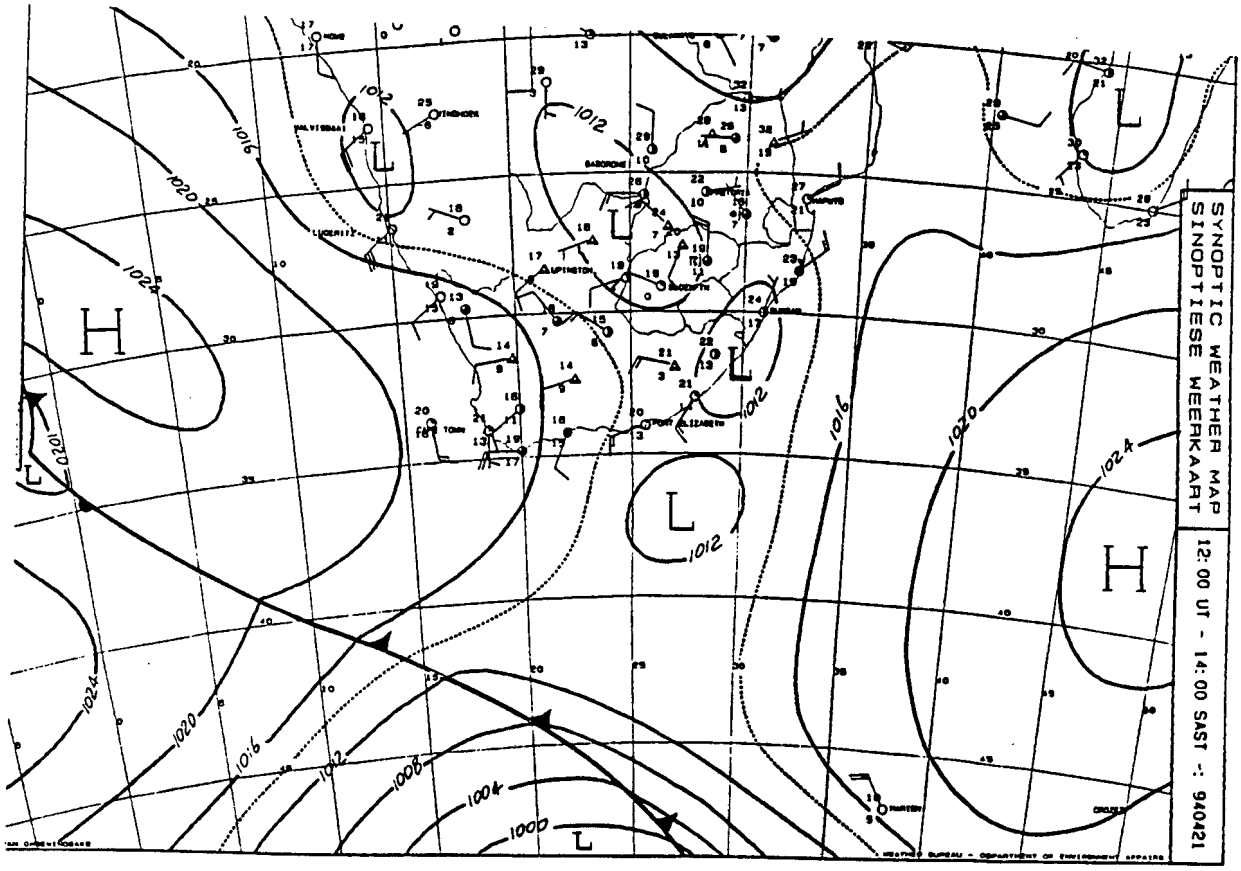

Figure 6.11: SAWB synoptic chart - 21 May 1994

The analysis presented here covers various synoptic stages of *anticylonic* ridging, *frontal* conditions and a *cold-air outbreak*. Whilst conserved variable analysis has proved to be an extremely useful diagnostic tool in the barotropic environment of the tropics (Betts and Albrecht, 1987) this may not necessarily be the case for the baroclinic environment of transient mid-latitude depressions. Data from the return leg of M95 will also be considered here.

6.2.3.1 Anticyclonic conditions

The prevailing wind direction under this synoptic type is determined by the position of the anticyclone. During the return leg of M95 *southwesterly* (Figure 6.12) (6 June) and *northerly* (Figure 6.13) (7 June) airflow of continental origin was encountered.

Composite plots for these and the *easterly* case (4-5 May) are given in Figure 6.14 and 6.15. Large variations occur in the height and nature of the subsidence inversion (Figure 6.14). We recall that a plot of air parcel points that have undergone mixing will fall on a straight line (mixing line) on a $\theta_e - r$ diagram. The convective boundary layer is characterized by a mixing line from the surface to the inversion where a $\theta_e - r$ kink is found (Figure 6.15). The convective boundary layer height (marked CBL) in Figure 6.15 was independently determined from the θ_v profile and therefore gives an unambiguous interpretation of this kink. Owing to the vertical

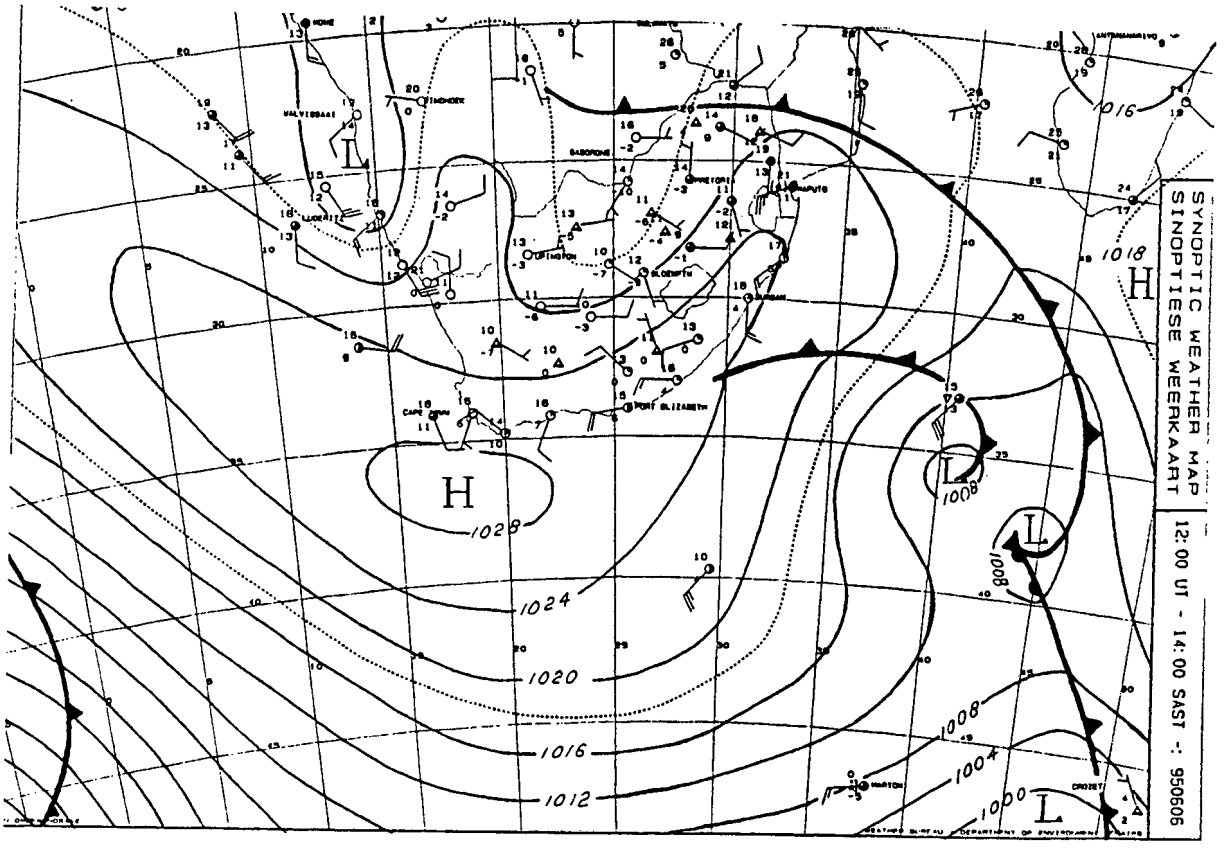

Figure 6.12: SAWB synoptic chart - 6 June 1995

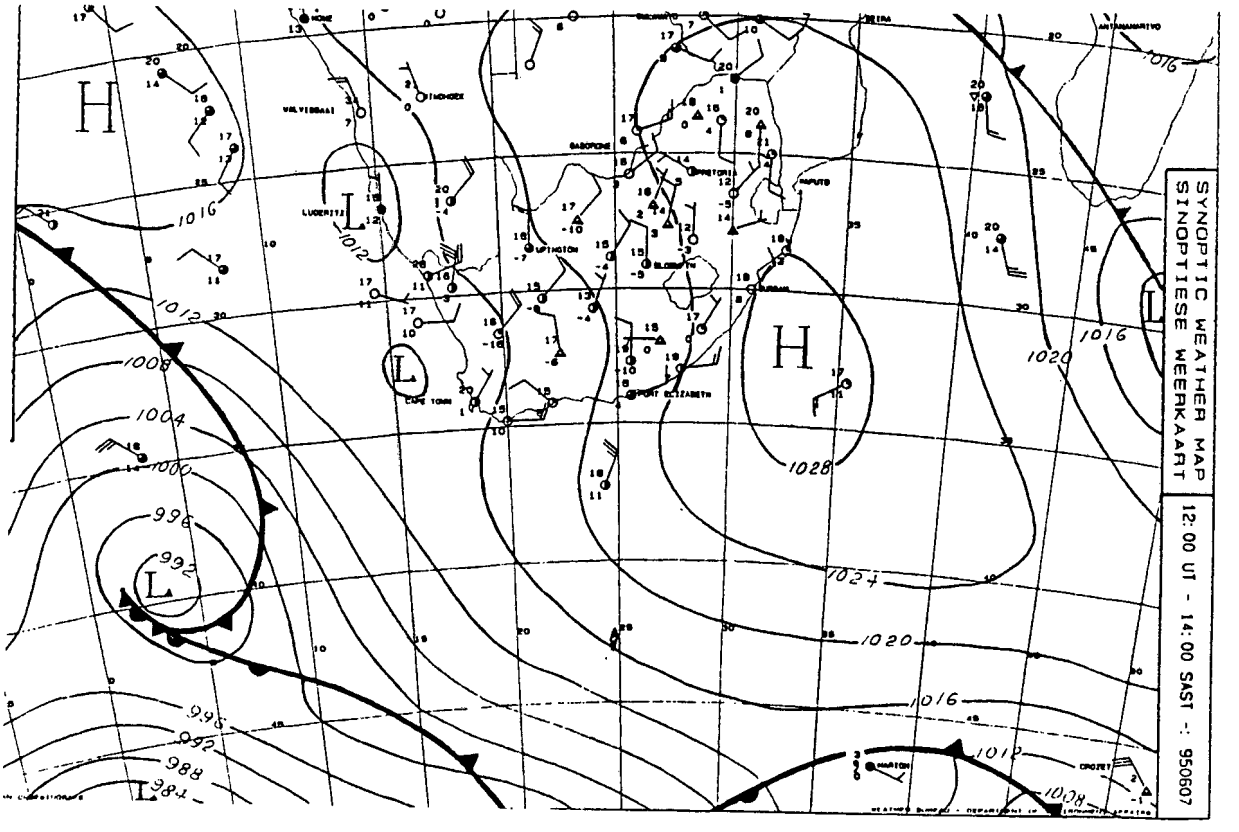

Figure 6.13: SAWB synoptic chart - 7 June 1995

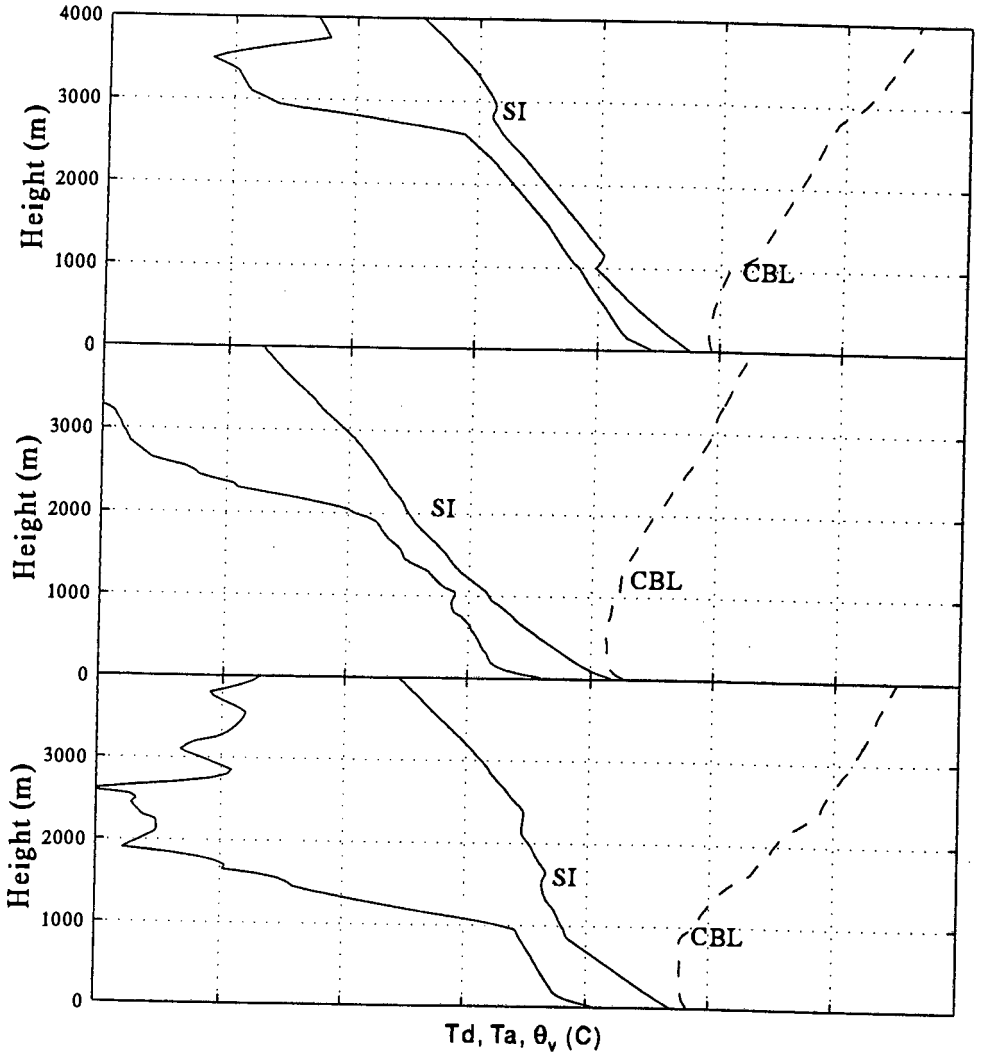

Figure 6.14: Composite plots of T_d, T_a and θ_v for the anticyclonic conditions of M94 and M95. The plots are from top to bottom: easterly case (M94), westerly case (M95), northerly case (M95). The approximate convective boundary layer (CBL) and subsidence inversion (SI) heights are shown.

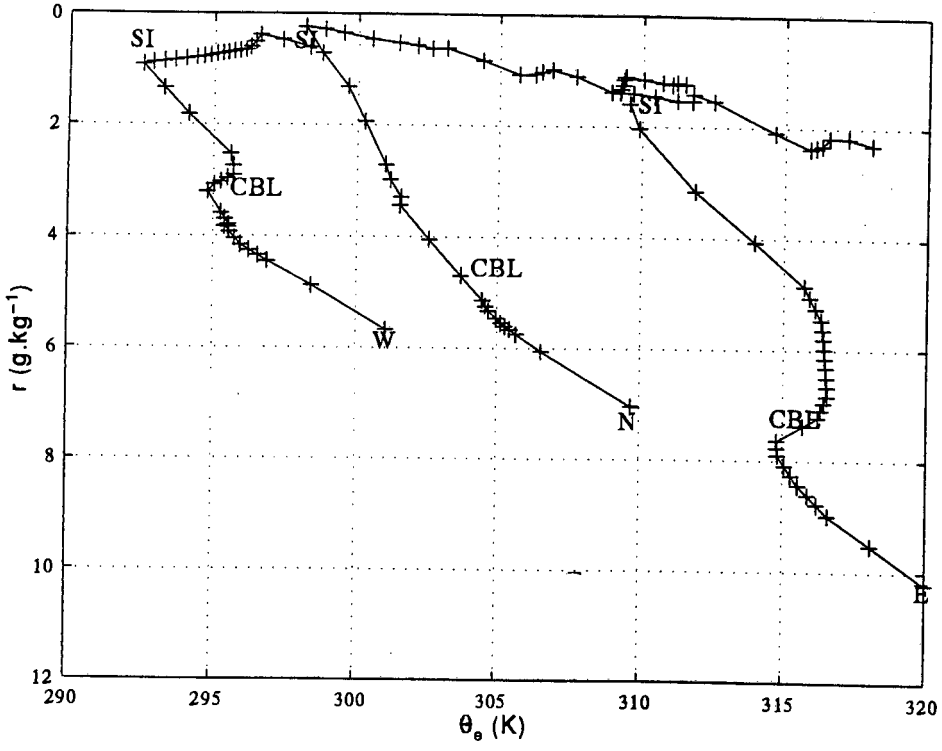

Figure 6.15: Conserved variable diagram of the mixing ratio, r, and equivalent potential temperature, θ_e, for the anticyclonic conditions of M94 and M95. The r-axis has been inverted so the composites presented here superficially represent a $\theta_e - P$ or $\theta_e - z$ plot. The plots are from left to right: westerly case, northerly case, easterly case (labelled W, N and E). The convective boundary layer top (CBL) and subsidence inversion (SI) are indicated.

resolution, the kink for the *easterly* case has been artificially smoothed. Clearly, free-atmosphere air parcels between the convective boundary layer and the subsidence inversion do not fall on a mixing line.

It is instructive to compare these results with those of Betts and Albrecht (1987) for the tropical Pacific ocean. They found that a single mixing line characterized the convective boundary layer until near a single inversion top at approximately (800 hPa). Variations on this mixing line occurred and were attributed to variations of the convective boundary layer height and penetrative downdrafts in deep cumulus clouds. In contrast, the results outlined above show a double-inversion structure. A characteristic mixing line is found below a $\theta_e - r$ kink at z_i. The kink distinguishes mixed-layer and free-atmosphere air properties. The upper inversion marks a θ_e reversal along which radiative cooling has occurred. This inversion has previously been erroneously identified as the boundary layer height (Mey et al., 1990; Figure 6).

6.2.3.2 Transient front

Composites plots (Figure 6.16 and 6.17) illustrate the mixing line structure characterizing boundary layer air and the height of the subsidence inversion. The boundary layer is slightly stable (Figure 6.16) in the presence of low surface heat fluxes.

The ambiguous $\theta_e - r$ structure above the convective boundary layer is possibly an indication of the baroclinic nature of the transient front. This may be compared to the less complicated thermodynamic structure above the convective boundary layer during the anticyclonic cases (Figure 6.15)

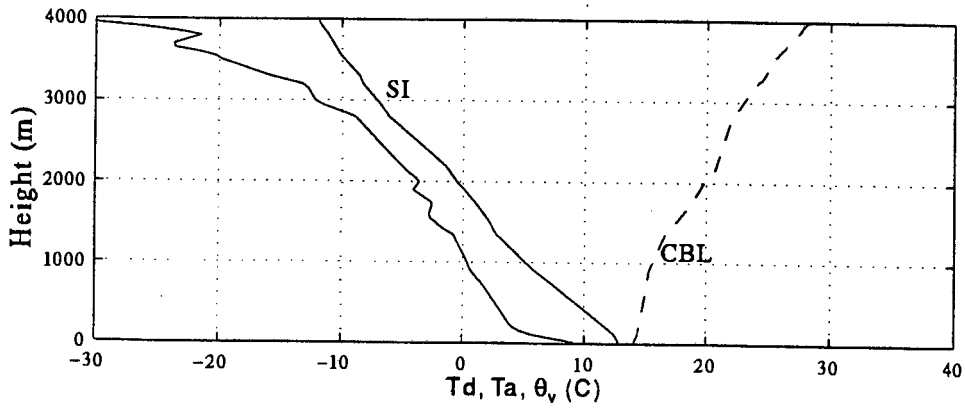

Figure 6.16: Composite plots of T_d, T_a and θ_v for the meteorological frontal conditions of M94. The approximate convective boundary layer (CBL) and subsidence inversion (SI) heights are shown.

6.2.3.3 Cold air outbreak

Composite plots for this case are shown in Figure 6.18 and Figure 6.17 The convective boundary layer and subsidence inversion heights occur at approximately 1500 m and 3500 m respectively. The mixing line in Figure 6.17 terminates at the convective boundary layer top and denotes the limit of boundary layer air. A striking difference is revealed when compared to the anticyclonic and transient frontal cases. The poorly developed $\theta_e - r$ kink (Figure 6.17) indicates an erosion of the inversion above the mixed layer in the presence of large, vigorous surface heat inputs.

Free-atmosphere air parcels fall on a vertical line that would indicate precipitation on a $\theta_e - r_T$ diagram (Betts and Albrecht, 1987). A thunderstorm in the presence of cumulonimbus (with typical anvil-shaped top) was observed during this period.

6.2.4 Boundary layer modification

The response of the boundary layer to the Agulhas Front was sampled during the *anticyclonic* and *transient frontal* cases. For the latter, conditions were not stationary. However, this case has been included for the sake of completeness.

6.2.4.1 Anticyclonic conditions

Atmospheric profiles over the ARR and AF for the **easterly** case are shown in Figure 6.19. The profile of the mean wind, U, describes a typical *trade-wind* profile (Figure 6.20). A local wind speed maximum occurs at approximately 800 m. Higher wind speeds over the AF may be associated with increased geostrophic wind speeds.

It is clear that the convective boundary layer structure over the ARR is replaced by a stable structure over the AF in agreement with the rapid decrease in fluxes. Significant moisture differences can be seen below 1000 m. Above 1000 m the moisture profiles are equivalent. The large lapse rate of q over the ARR may be related to a higher rate of entrainment on the warm side of the front (Khalsa and Greenhut, 1989). This acts to dry out the upper mixed layer (Hess, 1992; p 87).

Table 6.2 clearly demonstrates the impact of the spatial heat flux gradient (Figure 6.8) leading to a warmer and more moist boundary layer over the ARR where $\overline{q}$ and $\overline{\theta}_e$ are approximately 1.3 gkg^{-1} and 7 °C higher. Whilst Table 6.2 does not indicate a lower boundary layer top over the STC, Figure 6.8 shows that this does indeed occur. The ambiguity arises due to the difficulty in defining the stable boundary layer top (Stull, 1988; p 504-506).

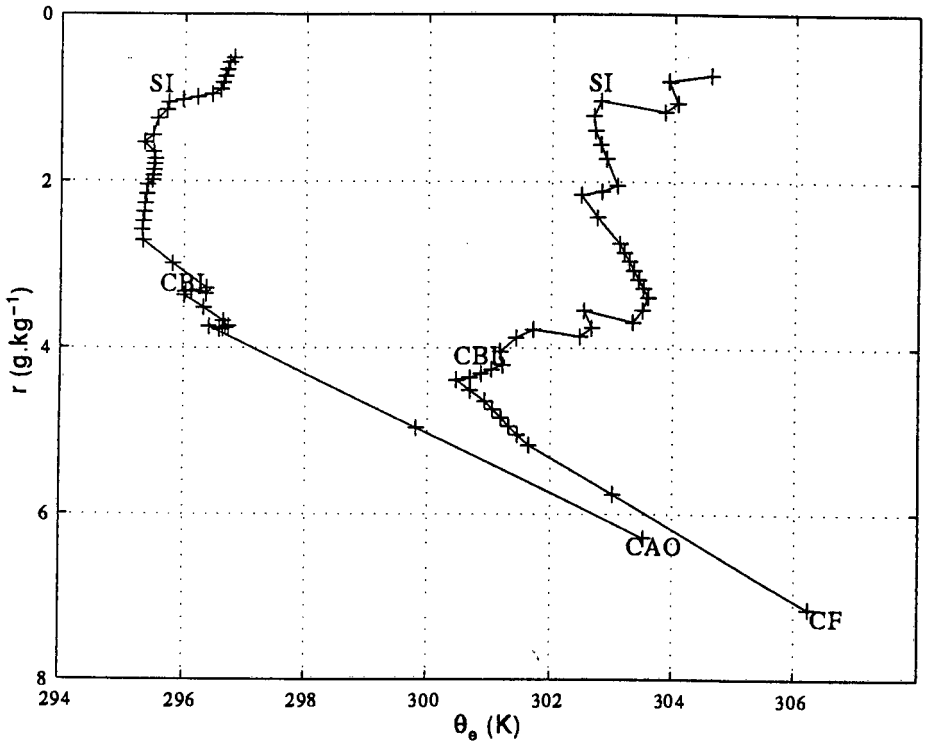

Figure 6.17: Conserved variable diagram of the mixing ratio, r, and equivalent potential temperature, θ_e, for the meteorological frontal conditions and cold-air outbreak of M94. The plots are cold-air outbreak (left) and transient frontal case (right) (labelled CAO (cold-air outbreak) and CF (cold front)). The convective boundary layer top (CBL) and subsidence inversion (SI) are indicated.

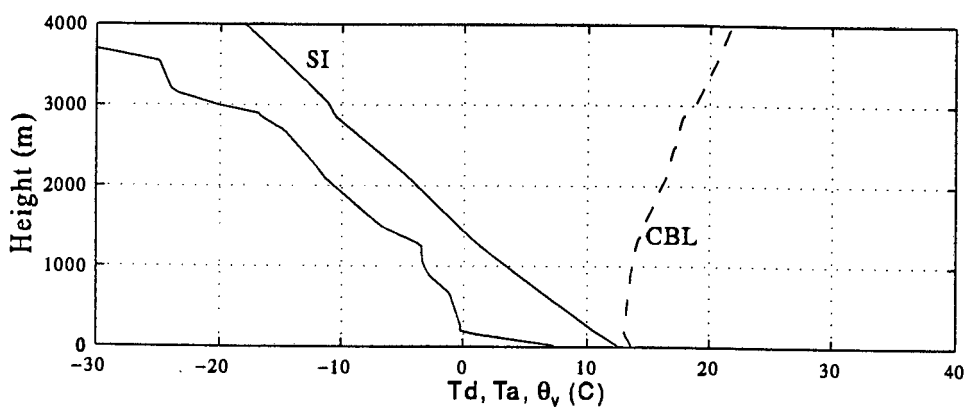

Figure 6.18: Composite plots of T_d, T_a and θ_v for the cold-air outbreak of M94. The approximate convective boundary layer (CBL) and subsidence inversion (SI) heights are shown.

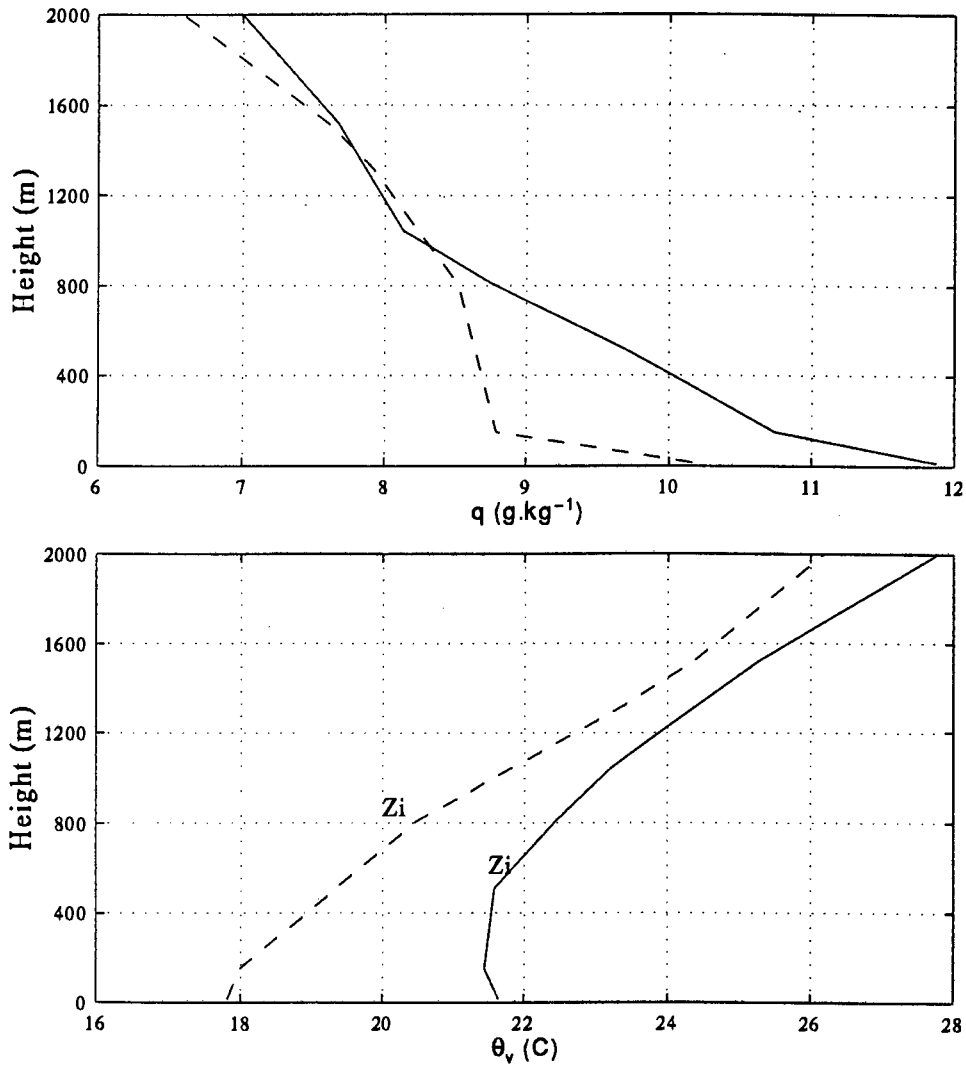

Figure 6.19: Atmospheric profiles showing boundary layer differences - anticyclone (easterly case) (M94). The plots are q (top) and θ_v (bottom); ARC (-) and AF (- -). The approximate mixed layer (z_i) and subsidence inversion (SI) heights are shown. The stable boundary layer over the AF is shown to have a deeper z_i. Clearly this is not the case - an explanation is given in the text.

Table 6.2: Boundary layer differences - Anticyclone - easterly flow. (The left hand column denotes the ascent positions).

	$\overline{z_i}$ (m)	$\overline{q}$ (gkg^{-1})	$\overline{\theta}$ (°C)	$\overline{\theta_e}$ (°C)	COMMENTS
ARC	600	10.3	20.0	49.5	CBL
AF	600	8.9	17.1	42.7	SBL

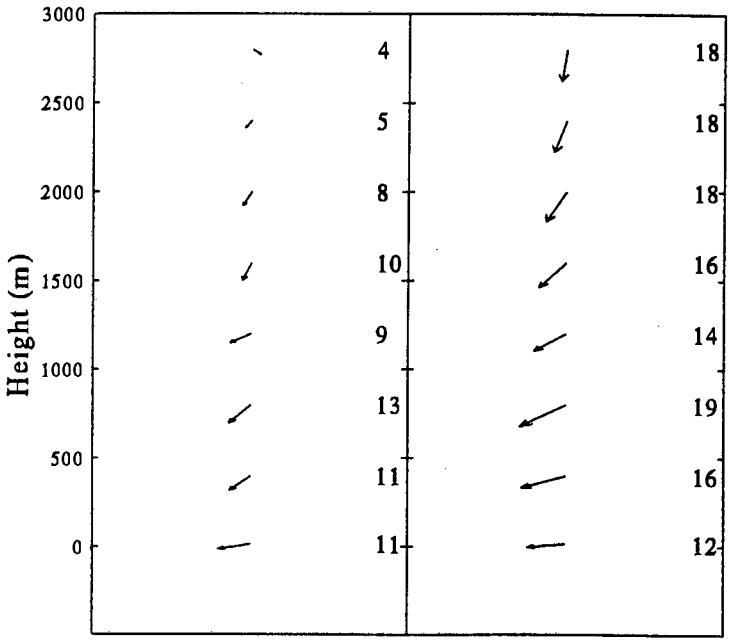

Figure 6.20: Profile of the mean wind (U) during anticyclonic conditions - easterly case (M94). Wind speeds are indicated in ms^{-1}, The plots are ARC (left) and AF (right). Surface easterlies spiral anticlockwise with height to become upper-level northwesterlies.

On the return leg of M95 a ridging anticyclone intitiated **southwesterly** flow on its southern limb on 6 June (Figure 6.12). This case has been studied by Jury and Walker (1988). Atmospheric profiles showing boundary layer differences (Figure 6.21) illustrate the air-sea interaction effects (Table 6.3).

Table 6.3: Boundary layer differences - Anticyclone - southwesterly flow

	$\overline{z}_i$ (m)	$\overline{q}$ (gkg^{-1})	$\overline{\theta}$ (°C)	$\overline{\theta}_e$ (°C)	COMMENTS
STC	1100	4.0	10.4	21.9	CBL
AF	1000	4.2	10.2	22.3	CBL
ARC	1500	4.1	12.1	24.1	CBL

Table 6.4: Boundary layer modification - Anticyclone - northerly flow

	$\overline{z}_i$ (m)	$\overline{q}$ (gkg^{-1})	$\overline{\theta}$ (°C)	$\overline{\theta}_e$ (°C)	COMMENTS
AC$^-$	900	6.3	13.9	32.0	CBL
AC	1200	6.2	17.5	35.4	CBL
AC$^+$	1000	6.0	18.5	36.0	CBL

By 7 June the anticyclone had moved northeastwards and initiated synoptic-scale airflow from the coast. It is therefore not surprising that a drying and warming occurs toward the coast (Figure 6.22 and Table 6.3). Superscripts $^-$ and $^+$ denote an ascent immediately prior to and after a feature. For example, the ascents AC$^-$, AC and AC$^+$ in Table 6.4 occured immediately prior to the AC (i.e over the AC southern SST front), over the AC and over the AC northern SST front.

6.2.4.2 Transient front

Ascents were carried out in the region of the STC, AF and ARC (Figure 6.23). A superadiabatic surface layer is again defined by the humidity profile. A convective boundary layer with well-defined mixed layer (stabilised boundary layer) is found over the ARC (STC and AF). A thermal wind defined by the positive wind shear is found (Figure 6.24) as in Mey et al. (1990).

Synoptic conditions were changing rapidly with the imminent arrival of the cold front. Mean characteristics for this case are given in Table 6.5 .

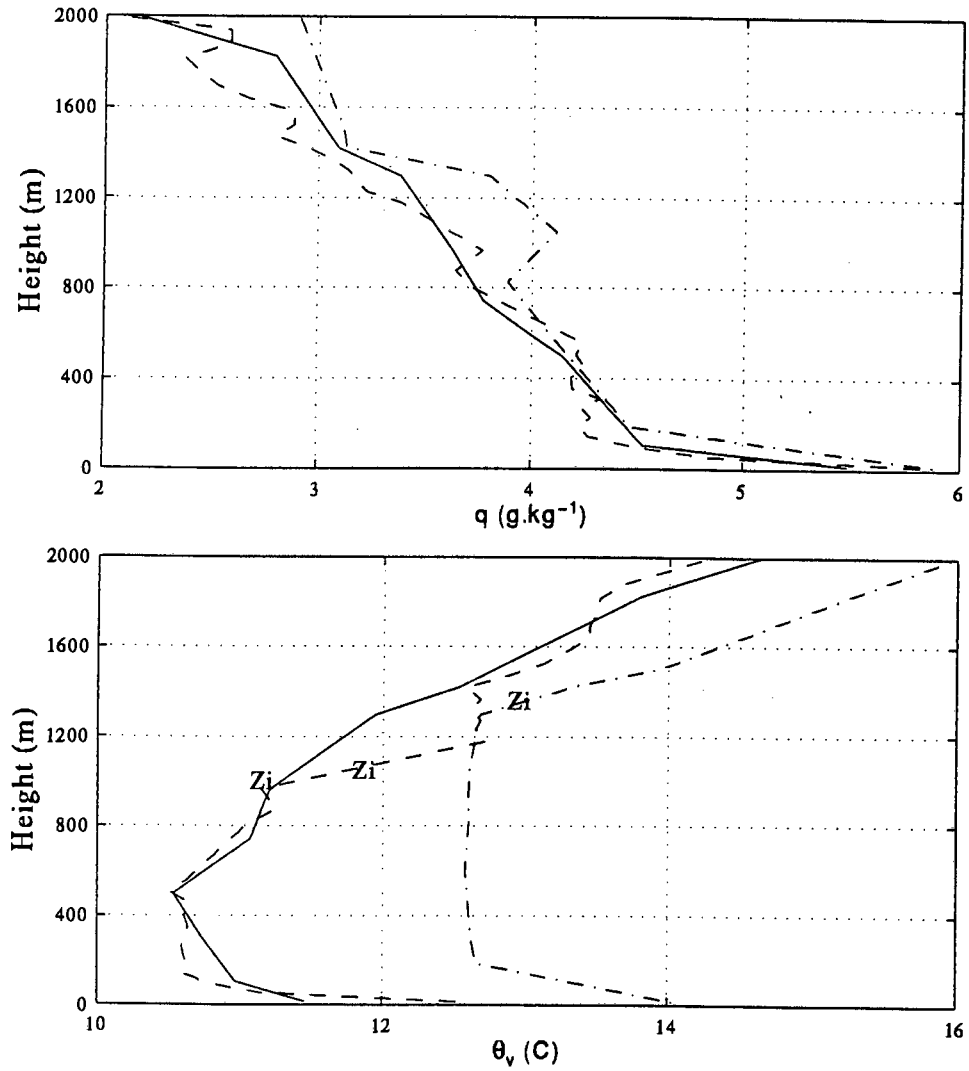

Figure 6.21: Atmospheric profiles showing boundary layer differences - anticyclone (southwesterly case) (M95). The plots are q (top) and θ_v (bottom); STC (-), AF (- -), ARC (-.).

Table 6.5: Boundary layer differences - Transient front

	$\overline{z}_i$ (m)	$\overline{q}$ (gkg^{-1})	$\overline{\theta}$ (°C)	$\overline{\theta}_e$ (°C)	COMMENTS
STC	750	5.5	13.3	29.2	SBL
AF	800	5.2	14.2	29.1	SBL
ARC	800	4.9	13.8	27.9	CBL

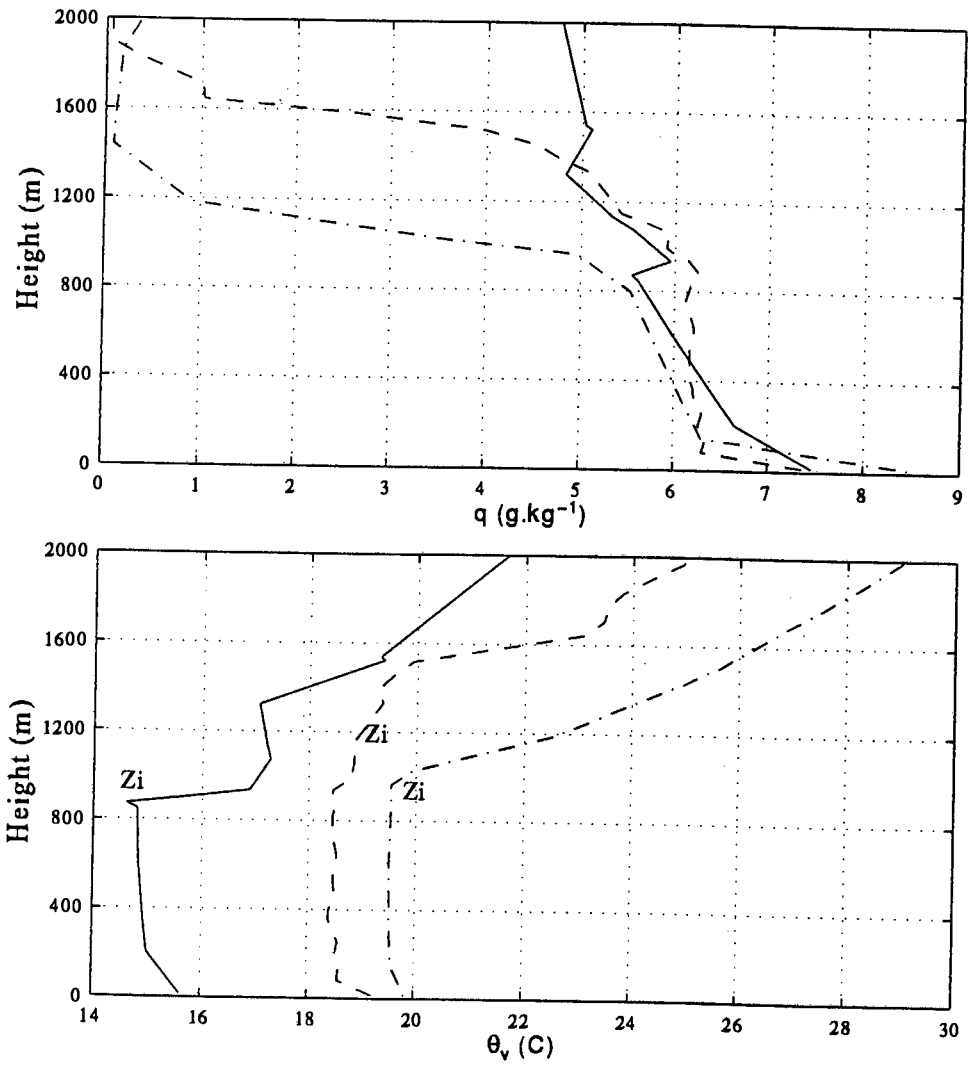

Figure 6.22: Atmospheric profiles showing boundary layer modification - anticyclone (northerly case) (M95). The plots are q (top) and θ_v (bottom); AC$^-$ (immediately prior to the AC) (-), AC (- -), AC$^+$ (immediately beyond the AC) (-.).

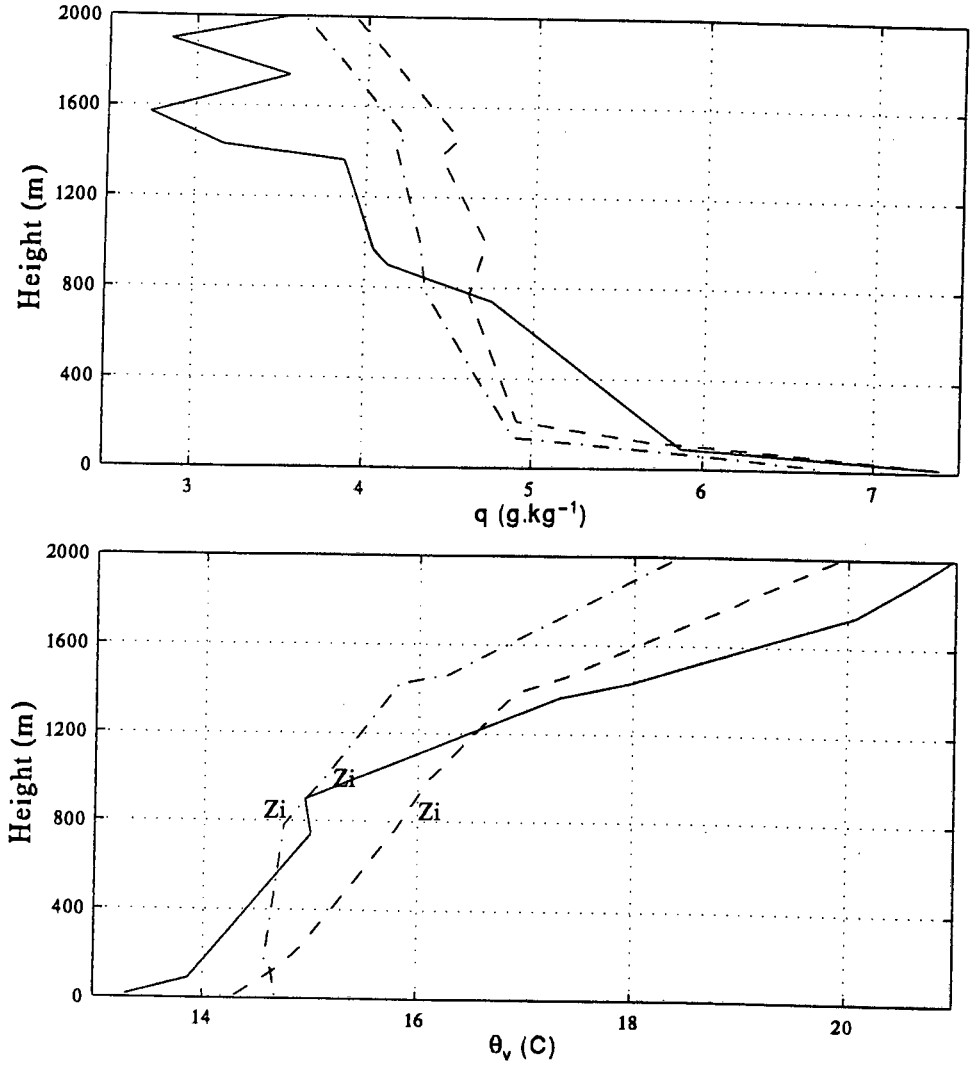

Figure 6.23: Atmospheric profiles showing boundary layer differences - transient front (M94). The plots are q (top) and θ_v (bottom); STC (-), AF (- -), ARC (-.).

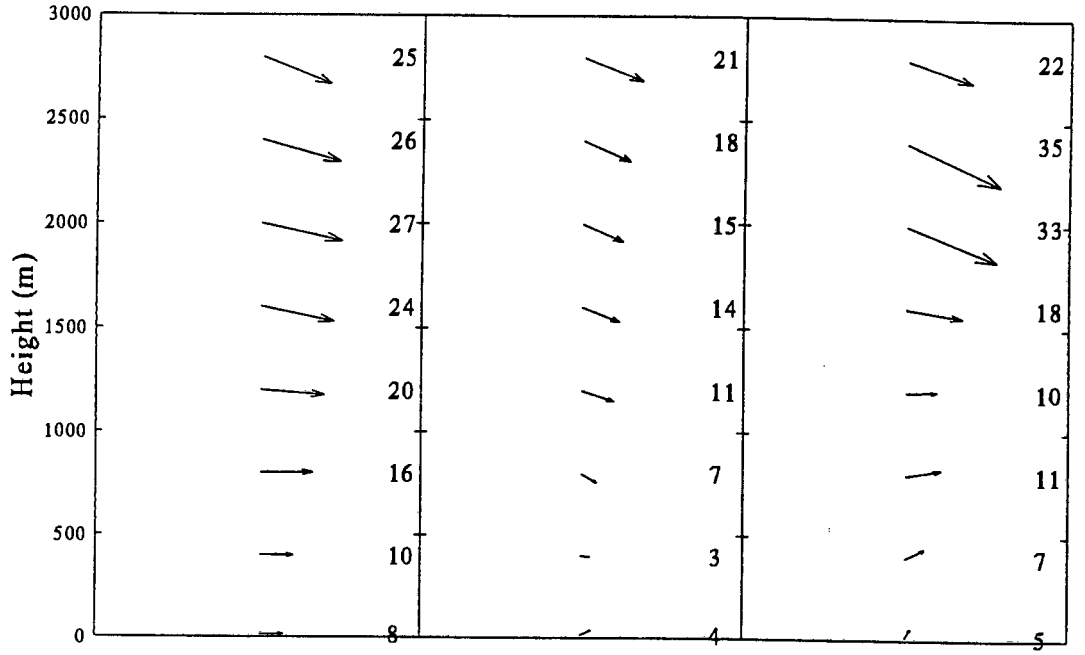

Figure 6.24: Profile of the mean wind (U) during meteorological frontal conditions (M94). Wind speeds are indicated in ms^{-1}, The plots are STC (left), AF (middle) and ARC (right). Westerly winds show marked vertical shear in the first 2000 m.

6.3 Agulhas Current

Results from the ACASEX dataset (collected during autumn 1995) are considered here. The ship track is shown in Figure 6.25.

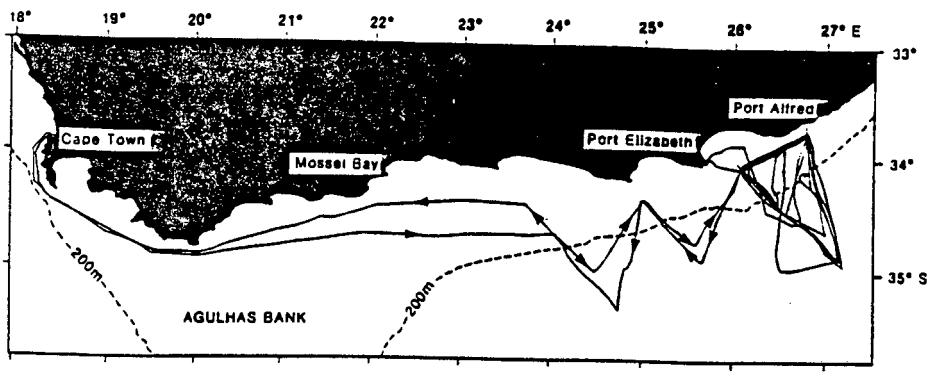

Figure 6.25: ACASEX - Schematic of the ship track (after Rouault et al., 1995). The inshore edge of the Agulhas Current follows approximately the 200 m isobath.

The study region of interest (the eastern Agulhas Bank) was chosen due to the high horizontal SST gradients found in this area (Rouault et al., 1995; Lutjeharms and Cooper, 1995). Twenty-four transects were carried out over the Agulhas Current (Figure 6.25).

6.3.1 Meteorological setting.

During the ACASEX period (21 April to 03 May) transient synoptic sytems tracked rapidly eastward. This may have implications for the stationarity assumption. Agulhas Current transects, however, were of the order of a few hours and synoptic stationarity is a reasonable assumption for most transects. An assortment of weak and moderate cold fronts and ridging anticyclones prevailed. The response of the boundary layer was thus sampled under a variety of conditions.

6.3.2 Air-sea fluxes of momentum, sensible and latent heat

Jury et al. (1993) have postulated that under *light* synoptic condtions or synoptic conditions with a predominantly *alongshore* component of airflow, secondary circulations might be expected to interact with transient weather systems. This is not the case for ACASEX. During gentle synoptic conditions surface heat fluxes were insufficient to generate large convective thermals. In general for ACASEX, the rapid transient nature of the weather systems introduced a high

degree of temporal variability which mitigated against the establishment of any coherent quasi-stationary secondary circulations.

Owing to the large number of transects it is not possible to describe the results of each in turn. Instead a representative subset has been chosen for discussion. However, air-sea transfer statistics for each synoptic type are given as averages for the entire dataset.

The accuracy of a bulk-derived u_* and roughness estimation may be unreliable around the Agulhas Current where current speeds of up to 2 ms^{-1} were measured (Rouault et al., 1995). This in turn has implications for the surface turbulent fluxes.

6.3.2.1 Light, variable conditions

On April 24 (Figure 6.27) maritime weather conditions were influenced by a weak low pressure that upon linking to a cold front to the south (Figure 6.26) had passed to the east of the subcontinent.

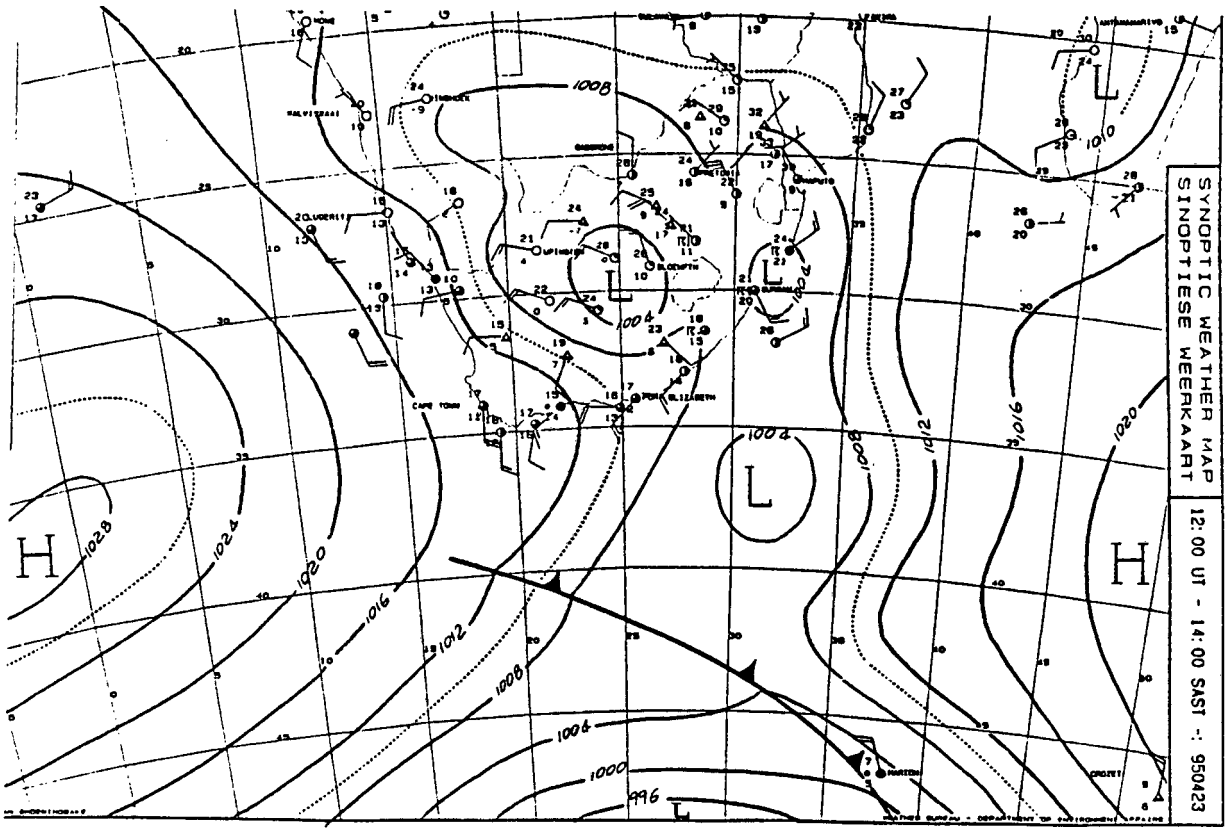

Figure 6.26: SAWB synoptic chart - 23 April 1995

Light, variable geostrophic winds were indicated. Moderate surface westerly winds were approximately parallel to the SST front (with a small component from cold to warm). The easterly winds of the previous two days had initiated surface upwelling in the study region. Shelf SSTs of 15 °C compared with values found for the core of the current ($\leq$ 25 ° C).

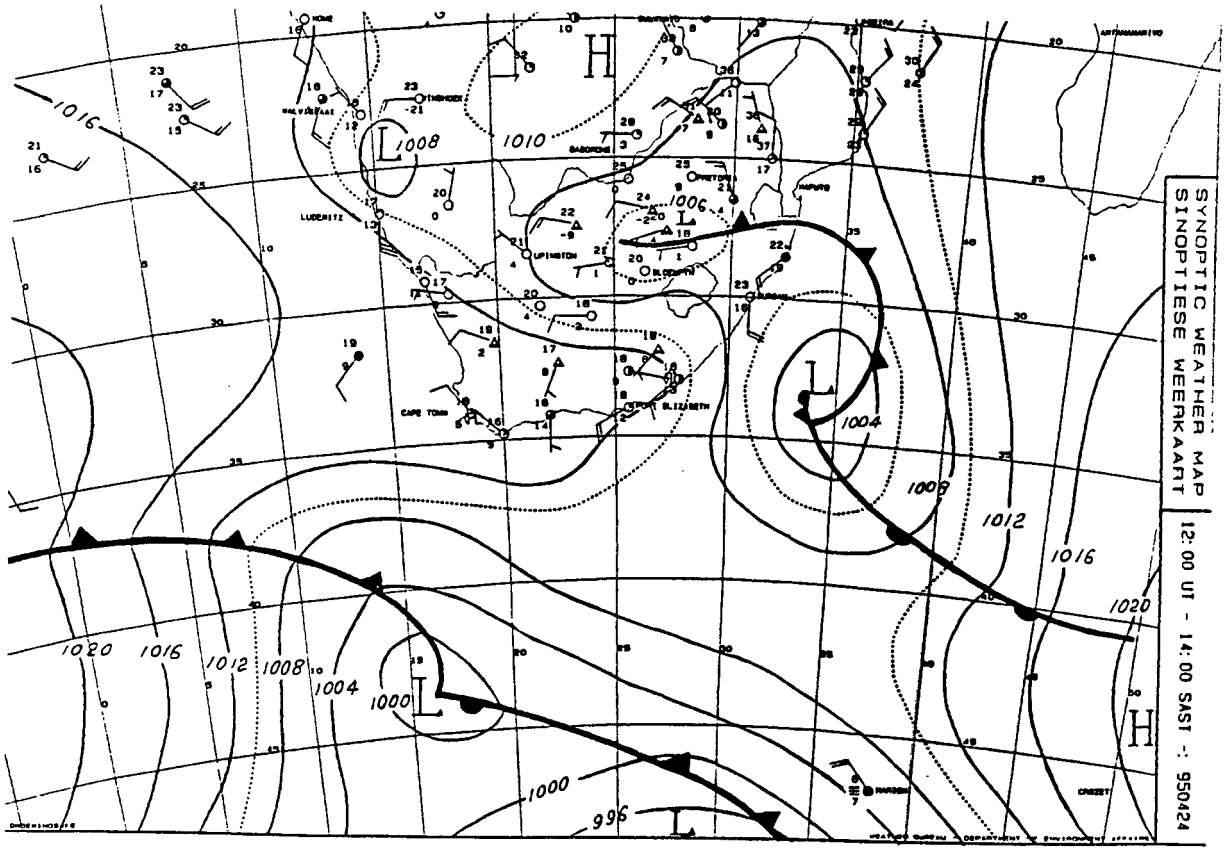

Figure 6.27: SAWB synoptic chart - 24 April 1995

The surface fluxes and forcing parameters for the transects (Figure 6.28) are shown in Figure 6.29.

The ship moved out of the current toward the shelf where the first SST dip may be seen. A transect was then undertaken in the seaward direction. The kink in Figure 6.29 occured during a rawinsonde launch when the ship drifted out of the current into the shelf area. Upon reaching the seaward border (SST $\simeq$ 20 °C) a second transect was undertaken in the shelf direction. In general, highest and lowest fluxes correspond to the current and inshore region. ζ_{10} is neutral to stable over the cool shelf area and corresponds to downward sensible and negligible latent heat fluxes. The shelf edge (first crossing of the SST front) is characterized by a large horizontal latent and negligible horizontal sensible heat flux gradient. Since Q_H gradients were relatively insignificant for all transects the horizontal heat flux gradient, dQ_T/dy, is adequately described by dQ_E/dy. Low fluxes during the second transect are due to an unusually calm period when the eastern Agulhas Bank was situated between two transient cold fronts (Figure 6.27). Winds speeds show an initially remarkable and rapid decline over the current. Large, negative values of ζ_{10} for this case are due to the small $u_\star$ and corresponds to a period of negligible wind stress.

It can be seen that for the weak synoptic forcing studied here, low surface heat and momentum fluxes are unlikely to destabilise the surface layer. This suggests that thermals will not

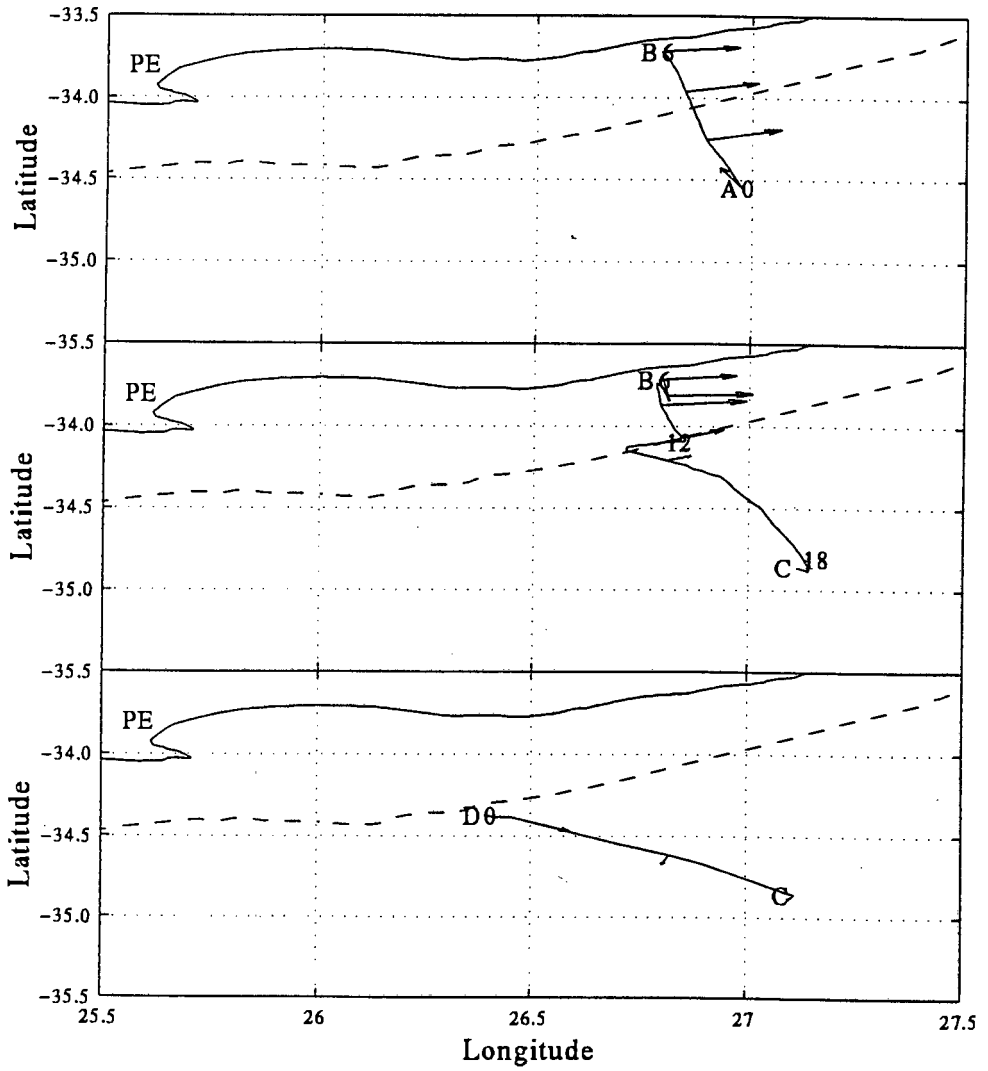

Figure 6.28: ACASEX 24 April - Schematic of the ship track showing transects, mean wind vectors (plotted every two hours), the 200 m isobath and PE (Port Elizabeth). Labels denote the end-points of each transect as they appear in Figure 6.29. Numbers indicate the time of day (GMT) at that position. The first transect is shown in the top panel, second transect in the middle panel and so on.

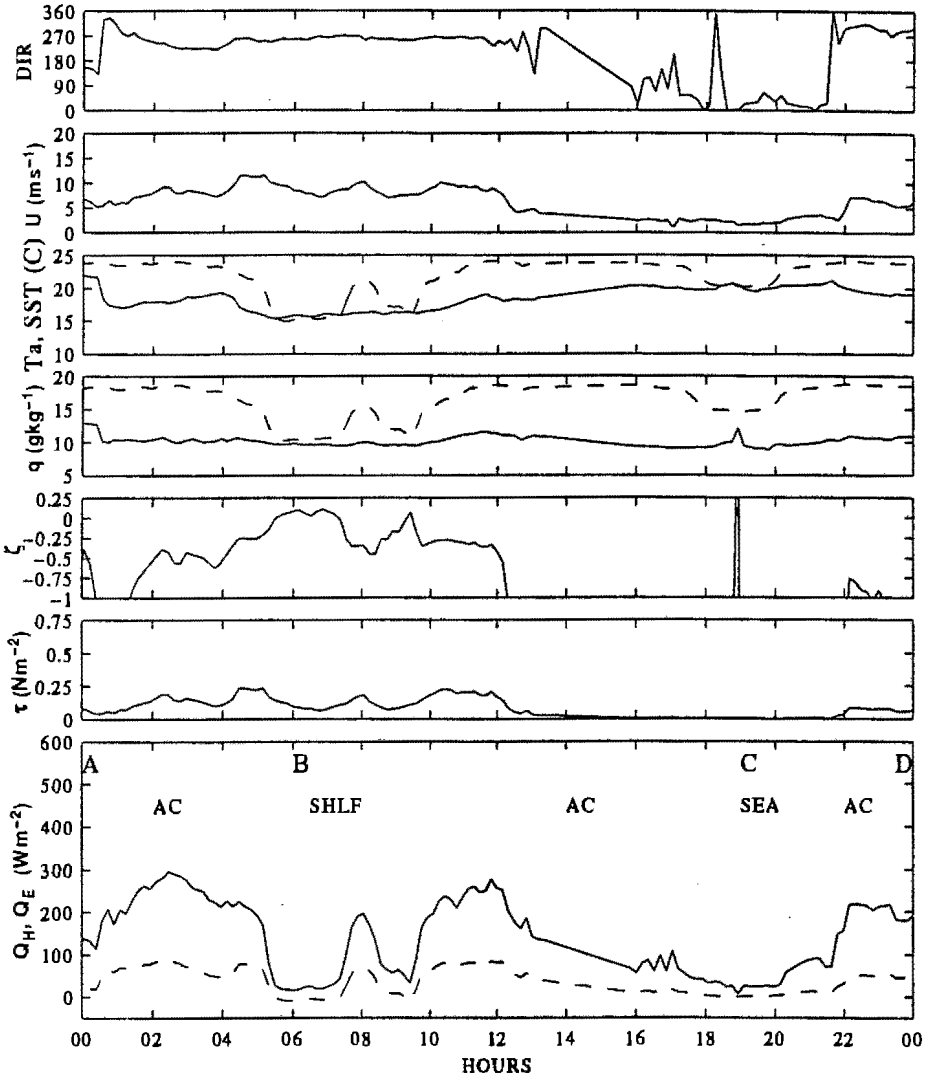

Figure 6.29: Time series of fluxes and parameters of interest during light, variable conditions - 24 April 1995. Parameters as for Figure 6.8. The positions of the Agulhas Current (AC), shelf (SHLF) and seaward border (SEA) are shown.

Table 6.6: Air-sea flux statistics - Light, variable conditions. The quantities dQ_T/dy, and $dSST/dy$ are the horizontal gradients of the total heat flux and sea surface temperature perpendicular to the inshore SST front (i.e between the shelf and current).

	$\overline{\tau}$	$\overline{Q}_H$	$\overline{Q}_E$	$\overline{Q}_T$	$max(Q_T)$	$\overline{\zeta}_{10}$	dQ_T/dy	$dSST/dy$
	$N.m^{-2}$	$W.m^{-2}$					$W.m^{-2}km^{-1}$	$°Ckm^{-1}$
SHLF	0.08	-7	20	13	23	0.07	9.8	0.3
AC	0.08	49	184	233	353	-4.5		

have any significant vertical extent. Furthermore the large horizontal surface heat flux gradient (Table 6.6) is expected to be instrumental in determining mean boundary layer characteristics across the inshore SST front.

6.3.2.2 Transient front

April 25 - 26 saw a strong transient cold front enter and depart the study region (Figures 6.30 and 6.31). It is during this period that highest surface heat of 728 Wm^{-2} occurred (Figure 6.33. Table 6.7).

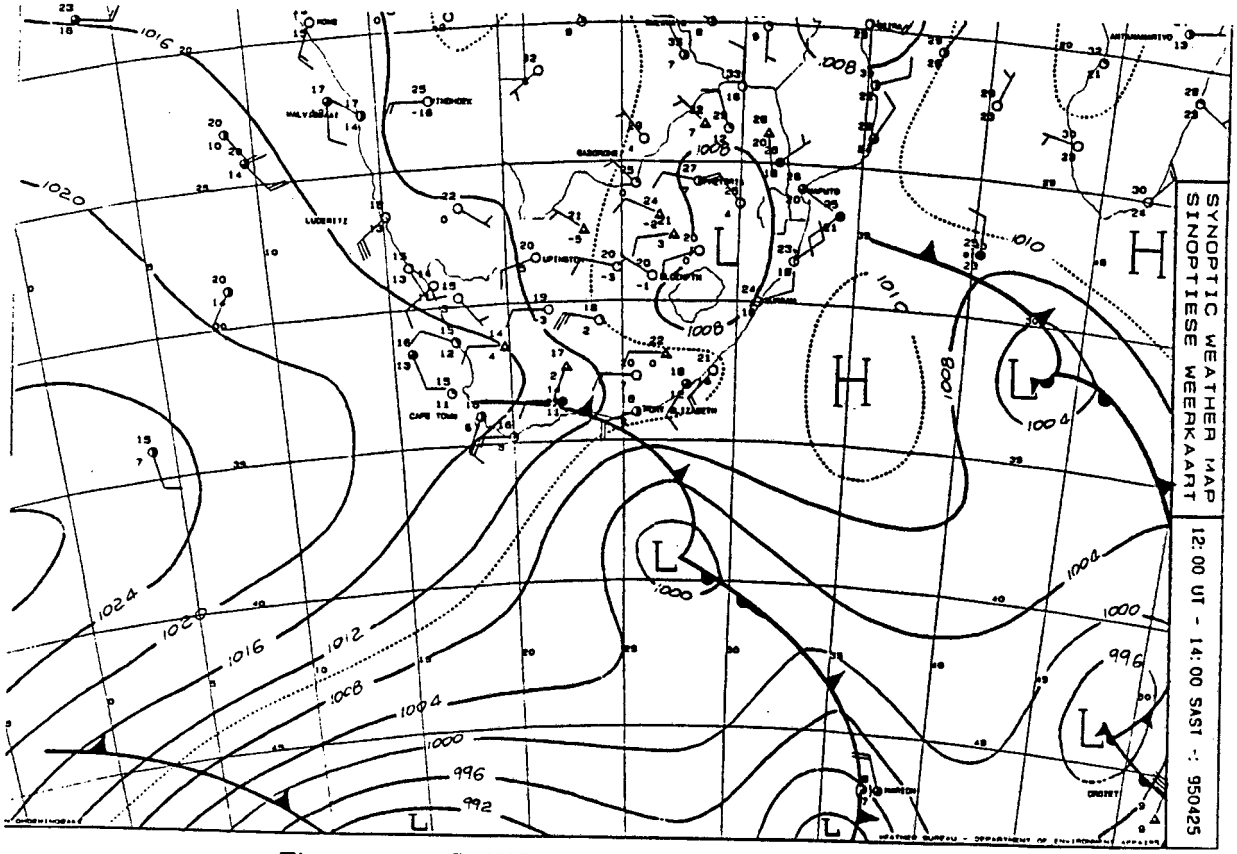

Figure 6.30: SAWB synoptic chart - 25 April 1995.

Winds from the west and south west were approximately parallel to the SST front. Wind speeds appear to increase offshore over the Agulhas current where wind speeds exceeded 15 ms^{-1} and decrease over the shelf. This may also be a synoptic feature associated with the baroclinic frontal zone of the transient front. The sharp dip in air temperature in Figure 6.33 coincides with a shift in wind direction and marks the arrival of the transient cold front. Surface fluxes in the meteorological post-frontal stage clearly exceed the pre-frontal stage.

Over the cool shelf, surface stability corresponds to a (small) downward total surface heat flux. In contrast, unstable to near neutral conditions prevailed over the seaward front and surface heat fluxes decrease only slightly. The decrease in surface fluxes is somewhat accentuated in

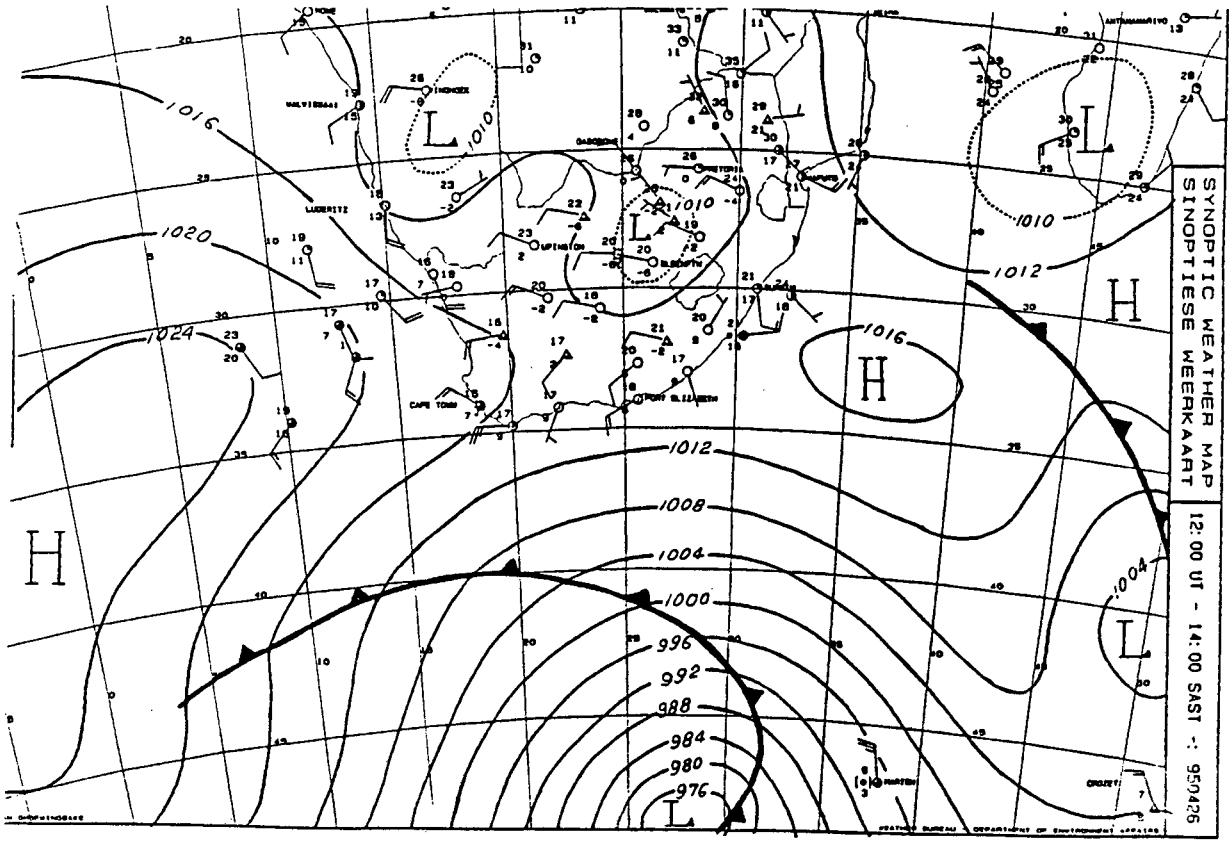

Figure 6.31: SAWB synoptic chart - 26 April 1995.

Table 6.7: Air-sea flux statistics - Transient front

	$\overline{\tau}$	$\overline{Q}_H$	$\overline{Q}_E$	$\overline{Q}_T$	$max(Q_T)$	$\overline{\zeta}_{10}$	dQ_T/dy	$dSST/dy$
	$N.m^{-2}$	$W.m^{-2}$					$W.m^{-2}km^{-1}$	$°Ckm^{-1}$
SHLF	0.11	7	66	73	135	-0.23	6.5	0.16
AC	0.44	96	460	556	728	-0.16		

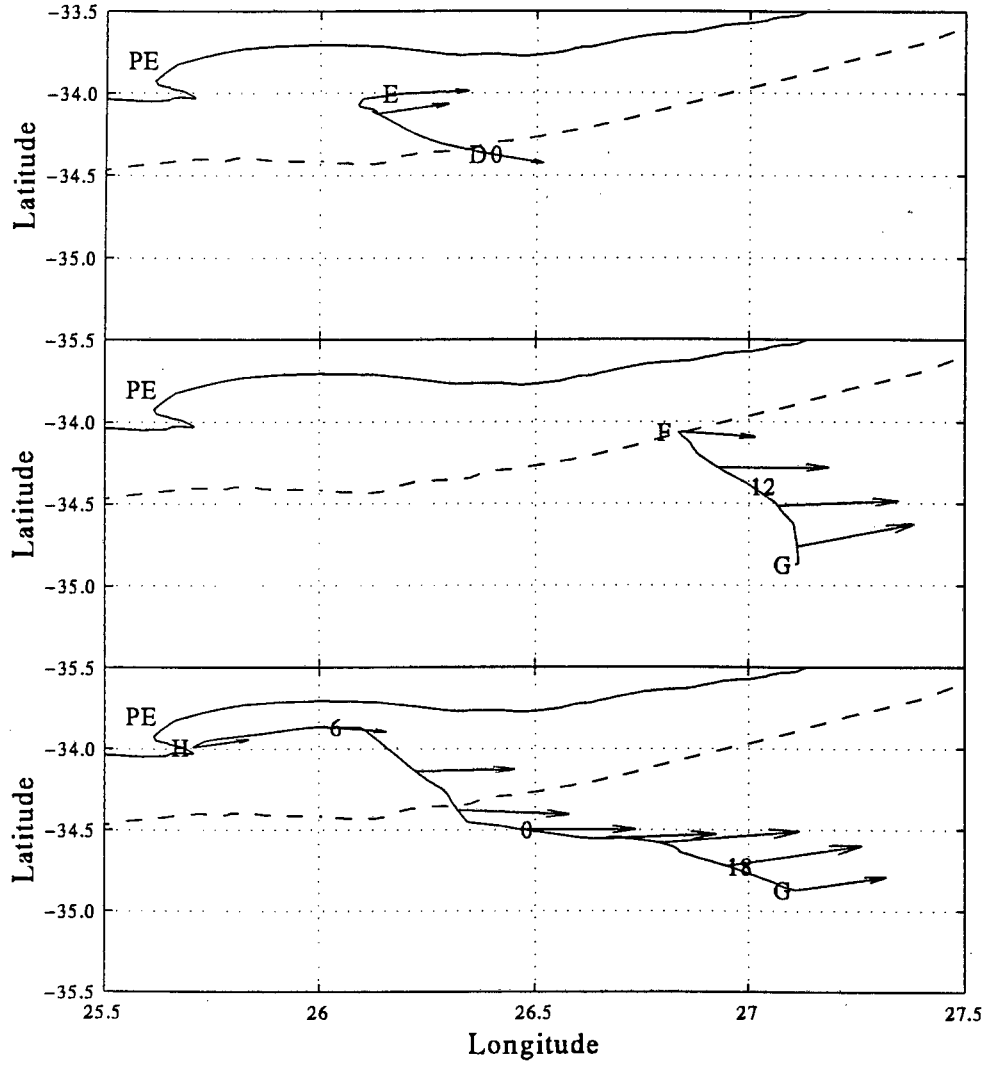

Figure 6.32: ACASEX 25 April - Schematic of the ship track showing transects and mean wind vectors. As for Figure 6.28 but for Figure 6.33

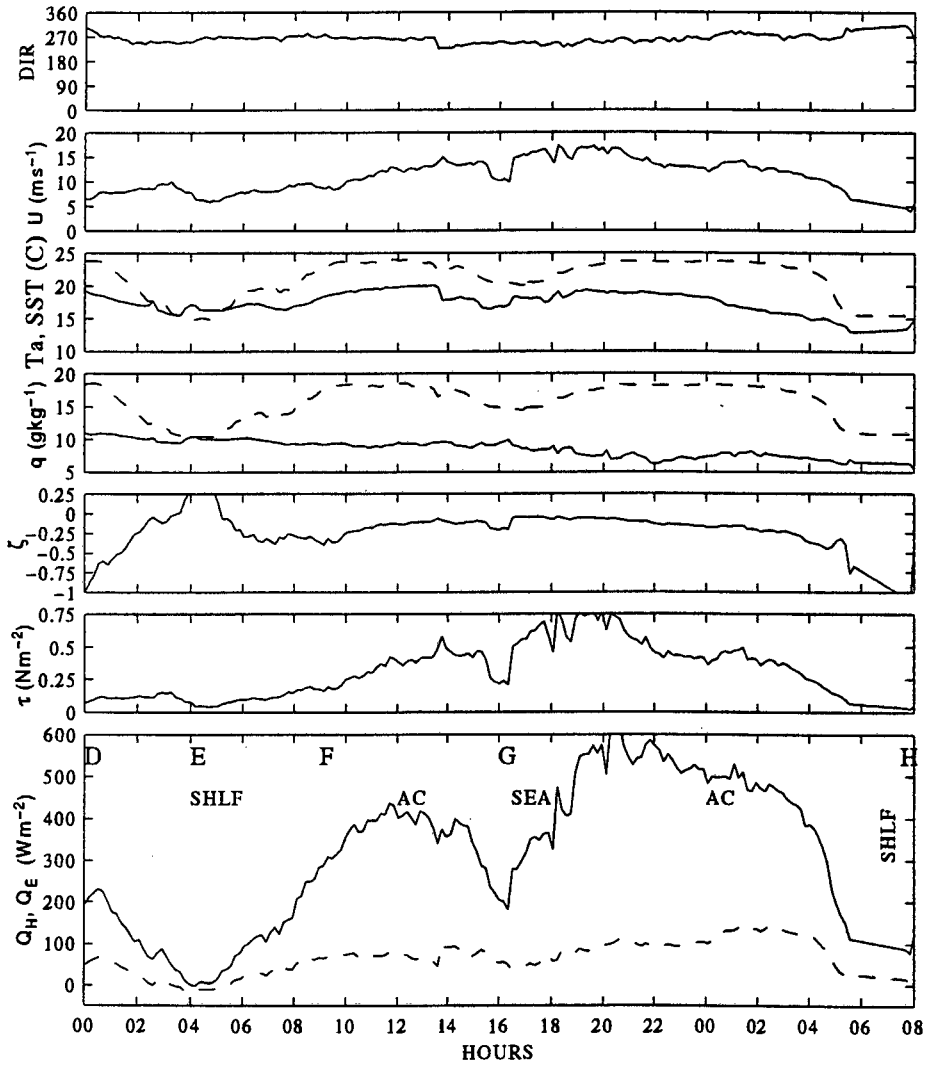

Figure 6.33: Time series of fluxes and parameters of interest during a transient front - 25 April 1995. Parameters as for Figure 6.8.

this case by a local wind speed minimum.

Horizontal surface heat flux gradients were analysed for each crossing of the SST front (Figure 6.32). Figure 6.33 shows a maximum (minimum) gradient for the inshore (seaward) SST front. Onshore Ekman drift of Agulhas Current surface waters under the westerly wind regime had reduced the intensity of the inshore SST front. This onshore transport extended nearer to the coast in the first transect (off Port Alfred) than the second (Algoa bay) where cold upwelled water was still present in the inshore zone. This explains the dQ_E/dy difference (Figure 6.33) for the two transects.

A simple pattern begins to emerge in agreement with Jury and Courtney (1991) and Jury (1993) whereby surface turbulent heat losses are maximised over the current, decrease dramatically over the inshore SST front and are negligible over the shelf. The horizontal heat flux profiles (Q_E and Q_H) for the westerly wind regime studied here agrees well with the smoothed profile of Jury and Courtney (1991; Figure 9) although the analysis here shows dQ_E/dy to be more intense.

6.3.2.3 Ridging anticyclone

It has been postulated that heat and moisture uptake over the Agulhas Current during onshore flow have important climatological consequences.

Onshore (southerly) flow was experienced as a result of a fairly strong ridge of high pressure on 28 April (Figure 6.34) behind a transient front. The maritime airmass had the open oceanic region to the south as its source region. Nevertheless a sustained latent heat flux of 320 Wm^{-2} was achieved (Figure 6.36). The surface sensible heat flux was moderate and positive over the current and negligible over the shelf. Warm Agulhas Current surface waters in the inshore region provided unstable conditions in this area. As a result the spatial latent heat flux gradients have been minimized in this scenario (Table 6.7).

Table 6.8: Air-sea flux statistics - Anticyclone - Southerly flow

	$\overline{\tau}$	$\overline{Q}_H$	$\overline{Q}_E$	$\overline{Q}_T$	$max(Q_T)$	$\overline{\zeta}_{10}$	dQ_T/dy	$dSST/dy$
	$N.m^{-2}$	$W.m^{-2}$					$W.m^{-2}km^{-1}$	$°Ckm^{-1}$
SHLF	0.01	6	40	46	71	-6.20	10.9	0.2
AC	0.10	52	268	320	469	-1.22		

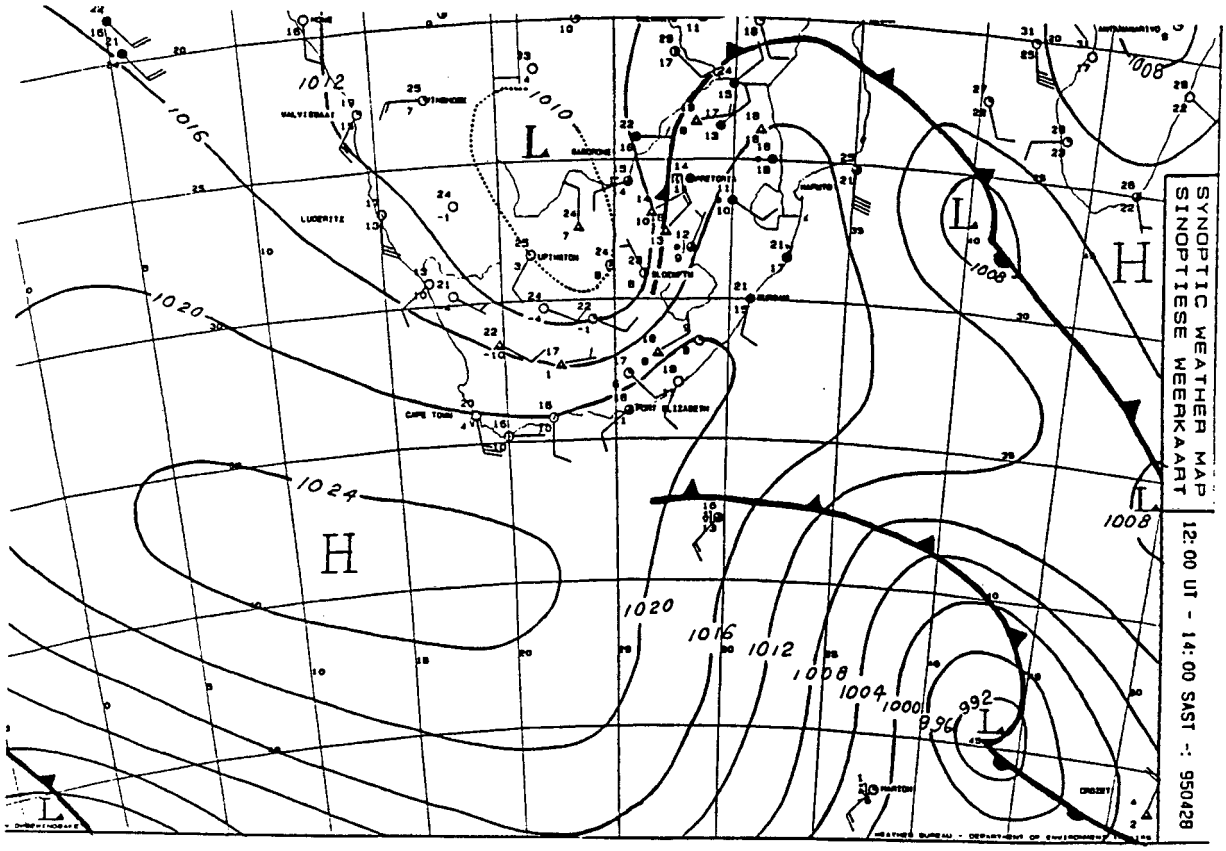

Figure 6.34: SAWB synoptic chart - 28 April 1995

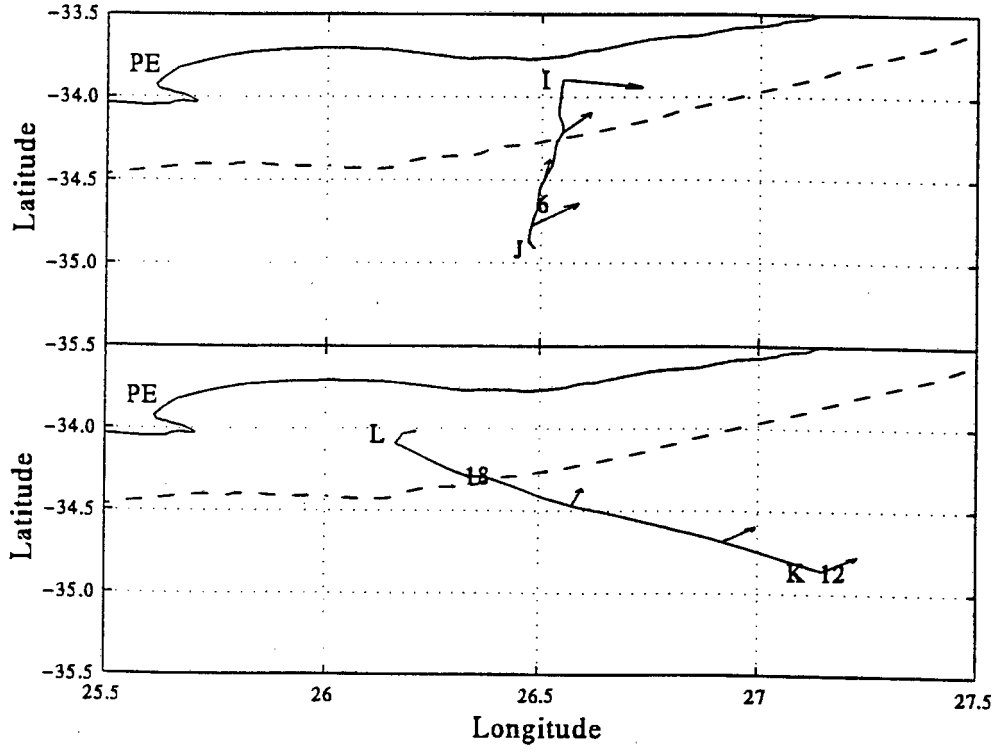

Figure 6.35: ACASEX 28 April - Schematic of the ship track showing transects and mean wind vectors. As for Figure 6.28 but for Figure 6.36

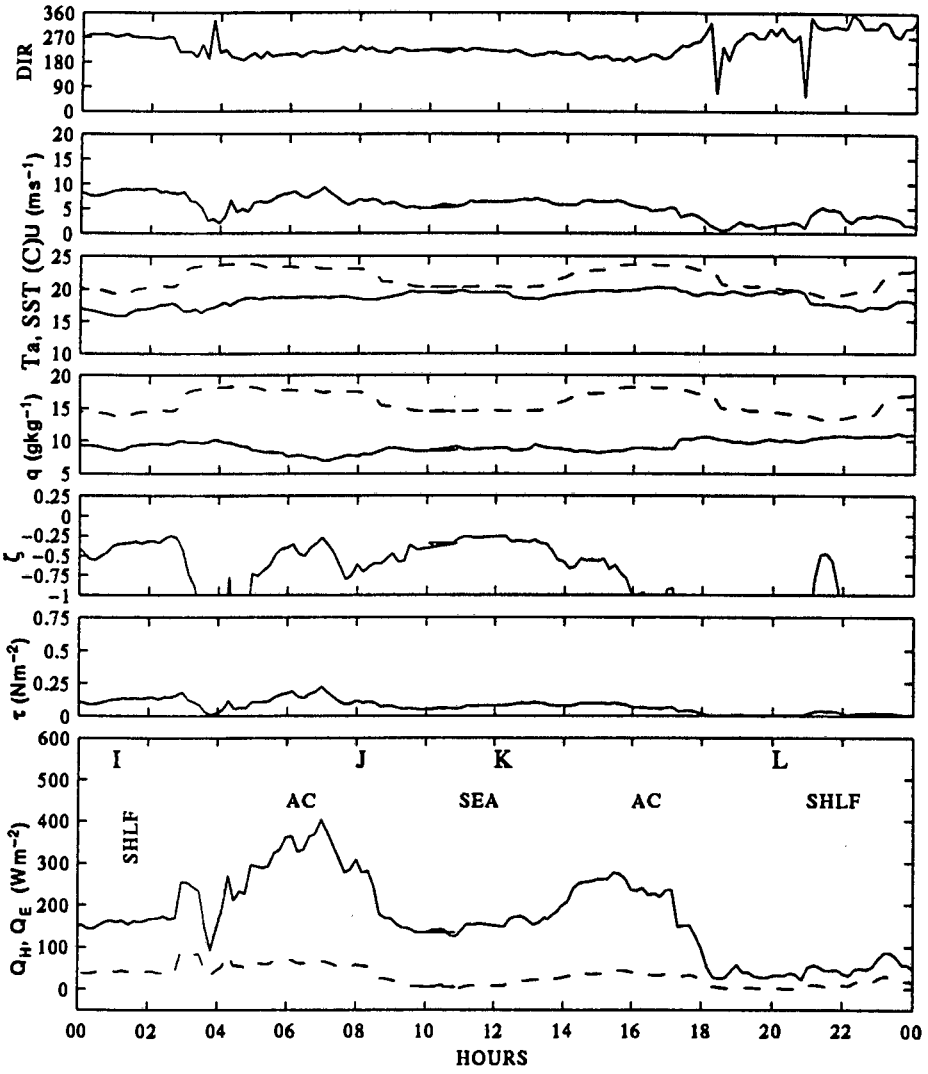

Figure 6.36: Time series of fluxes and parameters of interest during a ridging anticyclone - southerly flow - 28 April 1995. Parameters as for Figure 6.8.

Figure 6.37 follows the anticyclone as it continued to ridge eastwards on 29 May. An easterly airflow persisted which shifted to northeasterly the following day. The easterly flow was approximately to the inshore SST front.

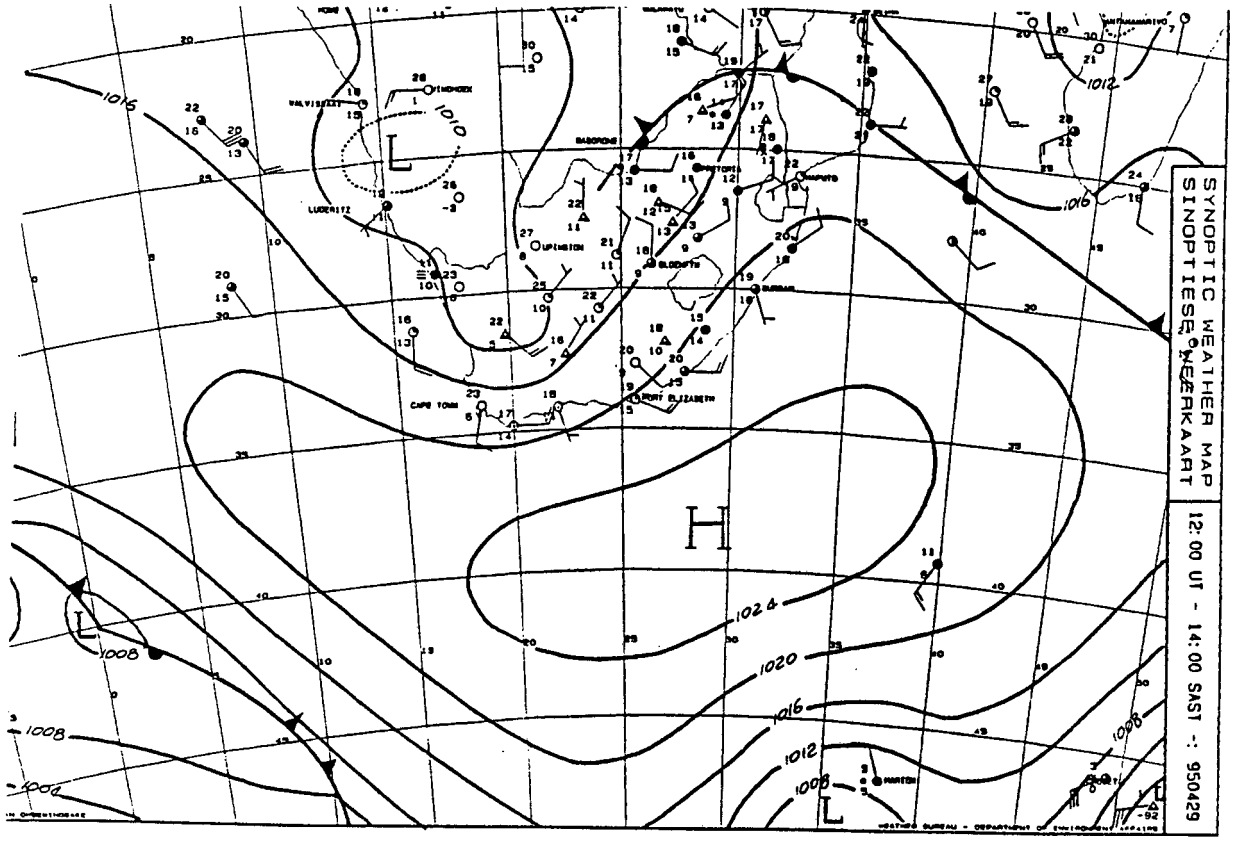

Figure 6.37: SAWB synoptic chart - 29 April 1995

Three transects were undertaken (Figure 6.38 and Figure 6.39). Mean surface heat losses are comparable to the previous day. Sensible heat fluxes were small and positive (negligible or negative) over the Agulhas Current (shelf). A maximum turbulent heat flux of 347 Wm^{-2} during this case for the third transect is related to the wind speed increase. SSTs over the shelf region are slightly cooler than the previous day (a feature that was to be repeated the following day).

By 30 April the anticyclone was situated well east of the subcontinent (Figure 6.40). Surface northeasterly winds were parallel to the axis of the inshore SST front. During this case that mean surface winds ($\overline{U}$=15 ms^{-1}) exceeded indicated geostrophic wind speeds (U_g=7.5 ms^{-1}) by a factor of 2. The two transects are shown in Figure 6.42.

The geostrophic departure is greatest for the second transect and corresponds to a shift in the wind direction. During this transect the wind speed increased over the current. Over the shelf region a dramatic decrease decrease in the wind speed is shown. Once again maxima, minima land highest horizontal gradients of surface momentum and heat fluxes correspond to

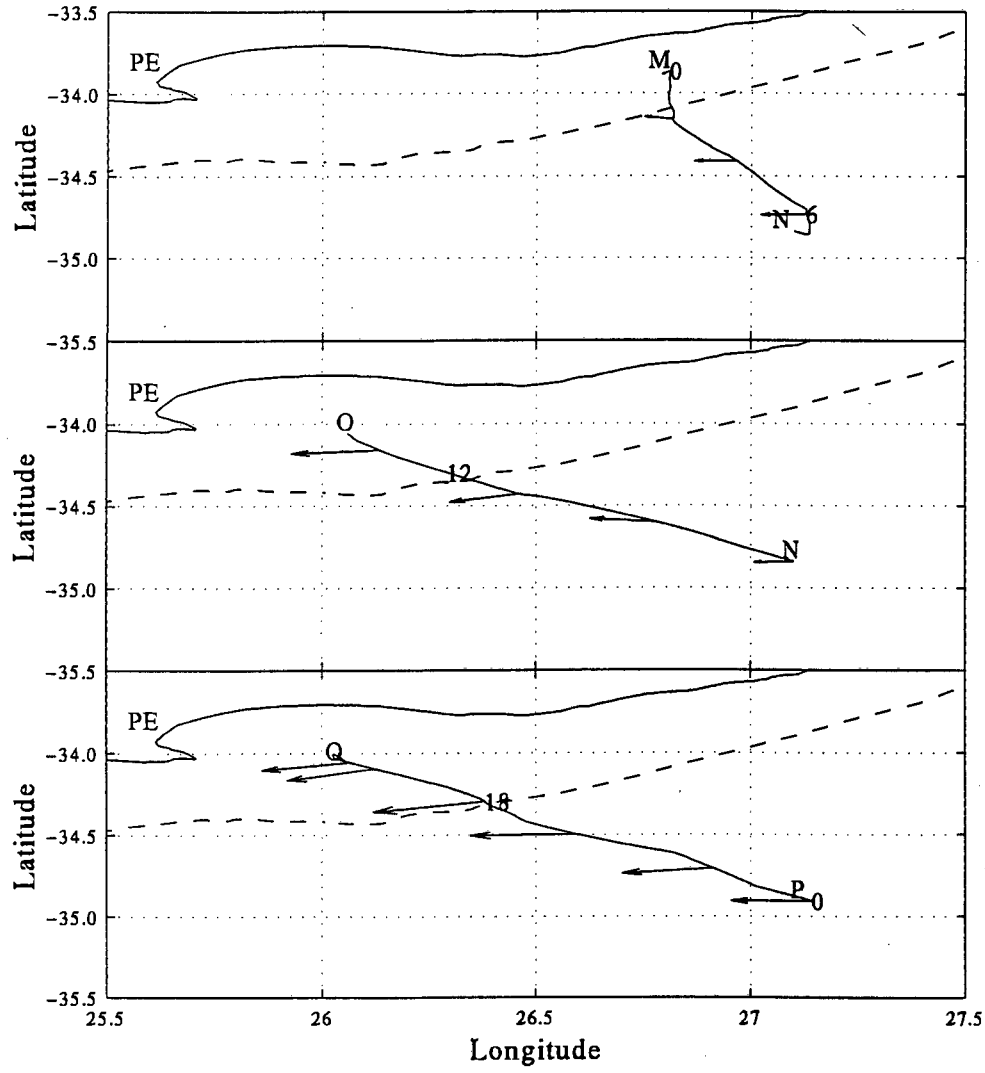

Figure 6.38: ACASEX 29 April - Schematic of the ship track showing transects and mean wind vectors. As for Figure 6.28 but for Figure 6.39

Table 6.9: Air-sea flux statistics - Anticyclone - Easterly flow

	$\overline{\tau}$	$\overline{Q}_H$	$\overline{Q}_E$	$\overline{Q}_T$	$max(Q_T)$	$\overline{\zeta}_{10}$	dQ_T/dy	$dSST/dy$
	$N.m^{-2}$	$W.m^{-2}$					$W.m^{-2}km^{-1}$	$°Ckm^{-1}$
SHLF	0.14	-5	78	73	102	-0.01	10.4	0.2
AC	0.10	38	198	236	347	-3.0		

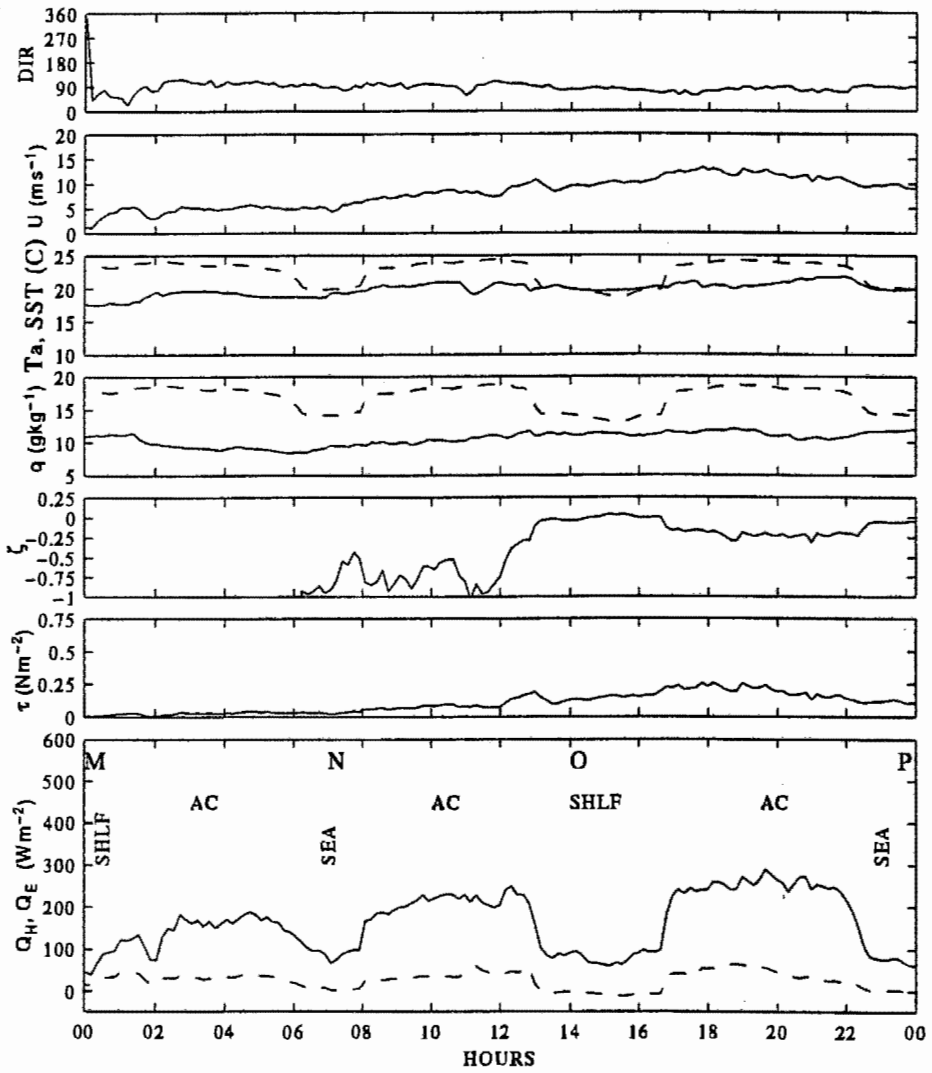

Figure 6.39: Time series of fluxes and parameters of interest during a ridging anticyclone - easterly flow - 29 April 1995. Parameters as for Figure 6.8.

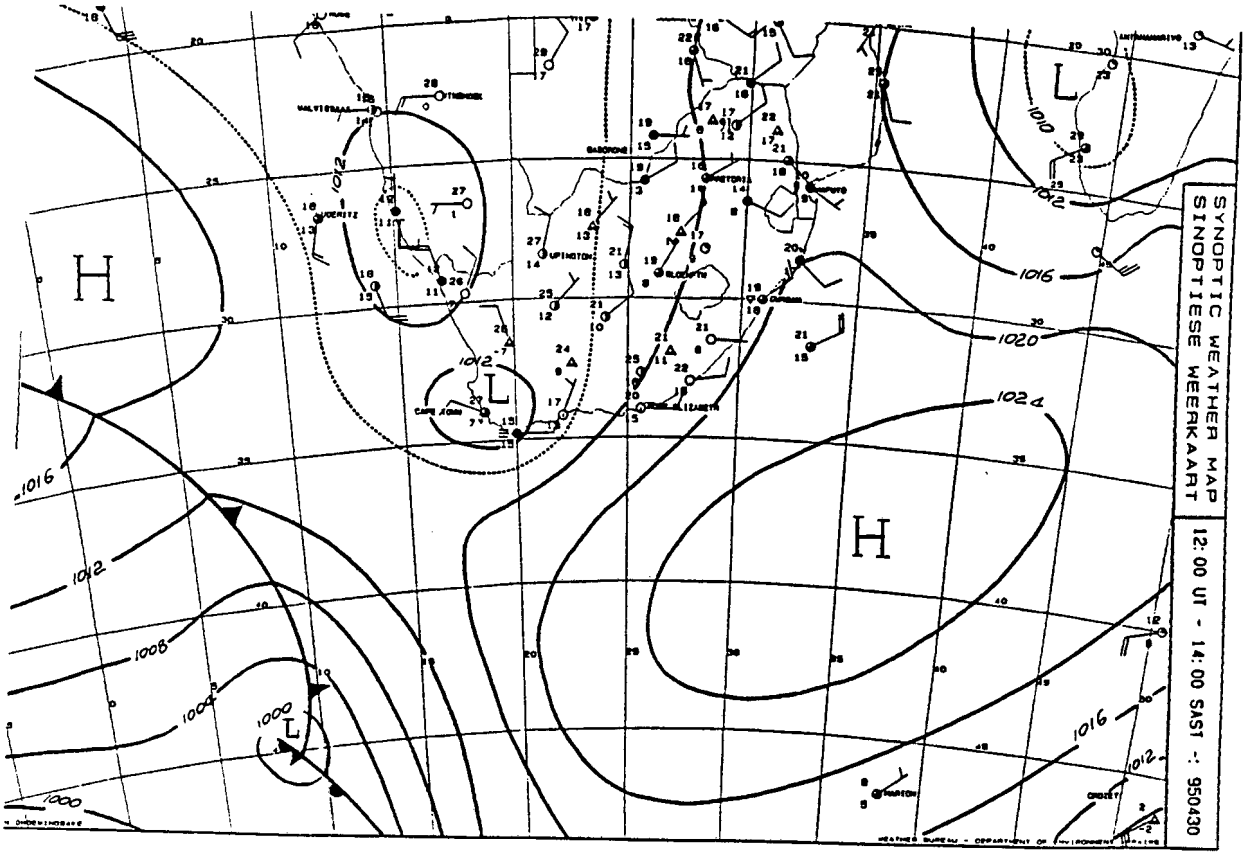

Figure 6.40: SAWB synoptic chart - 30 April.

the core of the current, the shelf region and the inshore SST front respectively. Conditions are stable over the inshore region.

6.3.3 Convective boundary layer mean thermodynamic structure

6.3.3.1 Light, variable conditions

The low heat fluxes for the case of 24 April (Figure 6.29) limited the vertical extent of convective eddies (Figure 6.43). Composite plots of the convective boundary layer mean profile and $\theta_e - r$ are shown in Figure 6.43 and 6.44.

A mixing line is found between the surface layer air and convective boundary layer top (CBL). The top of the convective boundary layer is again emphasised by a large $\theta_e - r$ kink. The line between CBL and the subsidence inversion does not denote a mixing line. A high-level subsidence inversion was again found to exist (Figure 6.43 and 6.44) at (2960 m).

6.3.3.2 Anticyclonic conditions

Composite thermodynamic structures for the ridging anticylone during the *southerly* (28 May), *easterly* (29 May) and *north-easterly* (30 May) are shown in Figure 6.45 and 6.46.

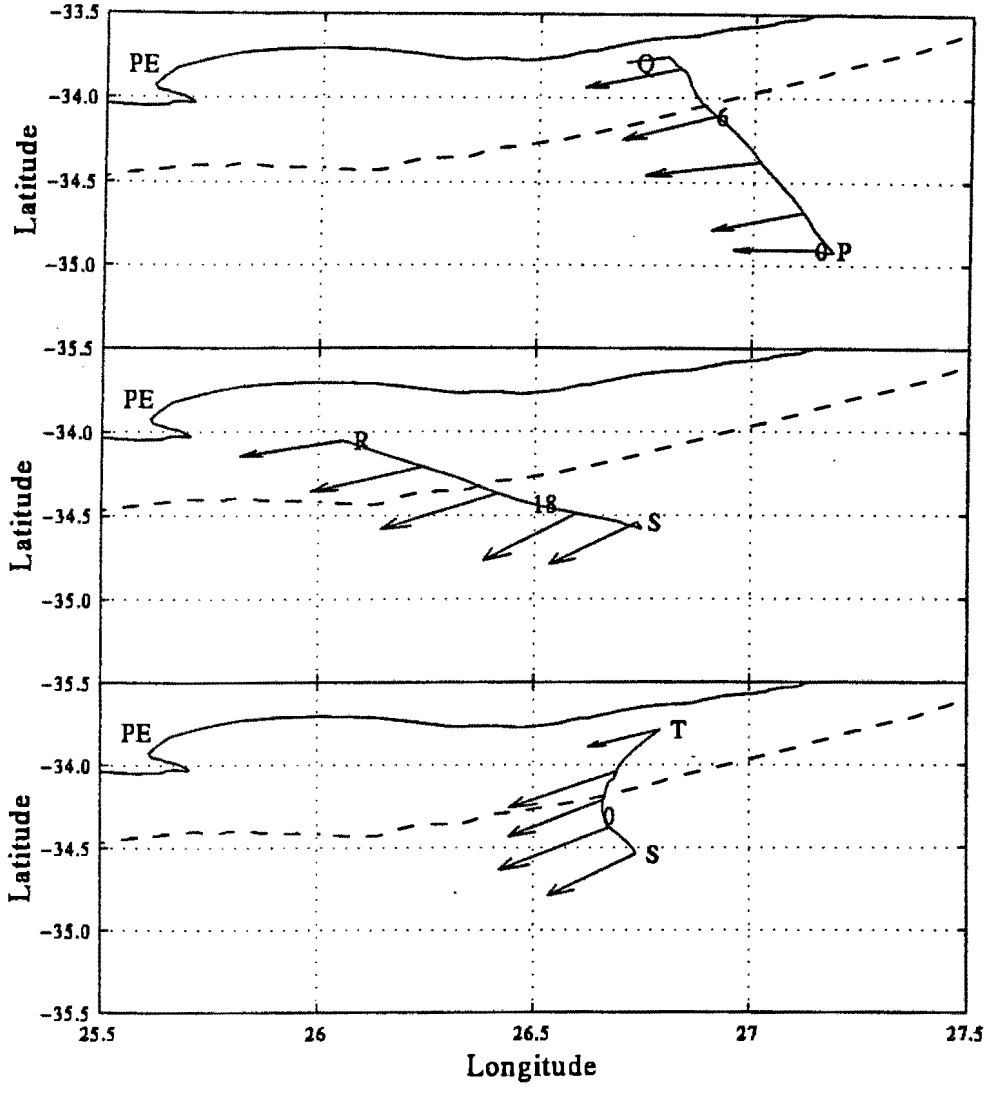

Figure 6.41: ACASEX 30 April - Schematic of the ship track showing transects and mean wind vectors. As for Figure 6.28 but for Figure 6.42

Table 6.10: Air-sea flux statistics - Anticyclone - Northeasterly flow

	$\overline{\tau}$	$\overline{Q}_H$	$\overline{Q}_E$	$\overline{Q}_T$	$max(Q_T)$	$\overline{\zeta}_{10}$	dQ_T/dy	$dSST/dy$
	$N.m^{-2}$	$W.m^{-2}$					$W.m^{-2}km^{-1}$	$°Ckm^{-1}$
SHLF	0.17	-31	58	27	92	0.13	6.1	0.12
AC	0.33	25	255	280	360	-0.09		

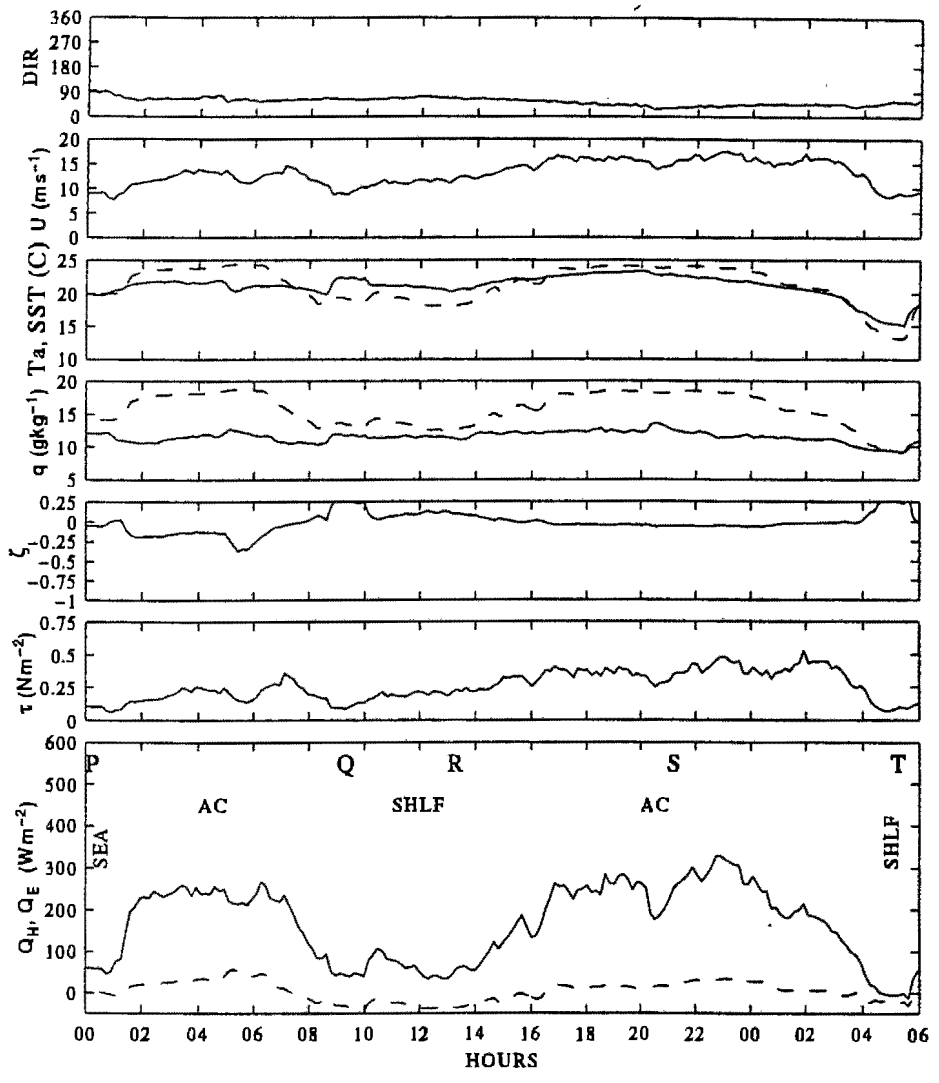

Figure 6.42: Time series of fluxes and parameters of interest during a ridging anticyclone - northeasterly flow - 30 April 1995. Parameters as for Figure 6.8.

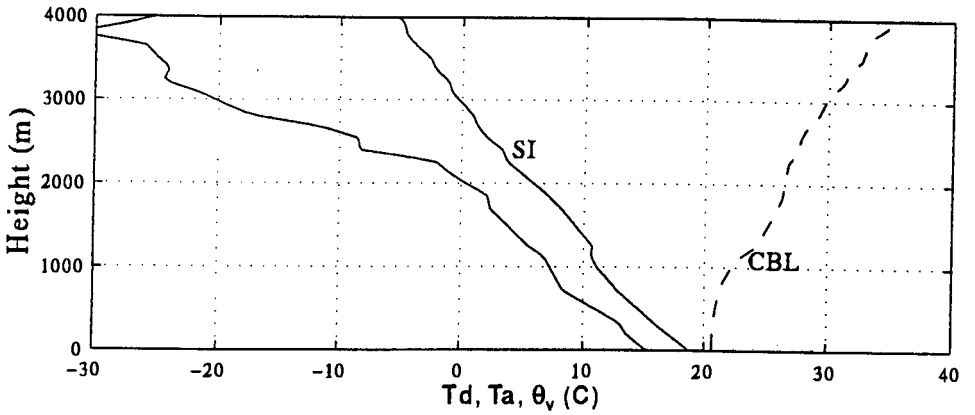

Figure 6.43: Composite plots of T_d, T_a and θ_v for the light, variable conditions of 24 April. The approximate convective boundary layer (CBL) and subsidence inversion (SI) heights are shown.

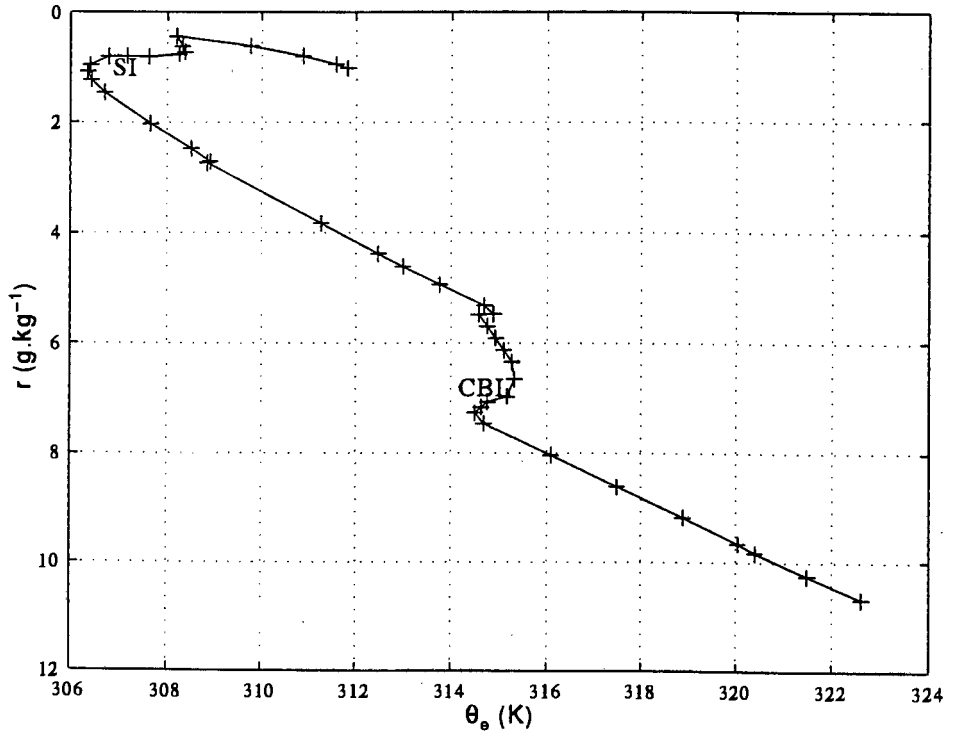

Figure 6.44: Conserved variable diagram of the mixing ratio, r, and equivalent potential temperature, θ_e, for the light, variable conditions of 24 April. The convective boundary layer top (CBL) and subsidence inversion (SI) are indicated.

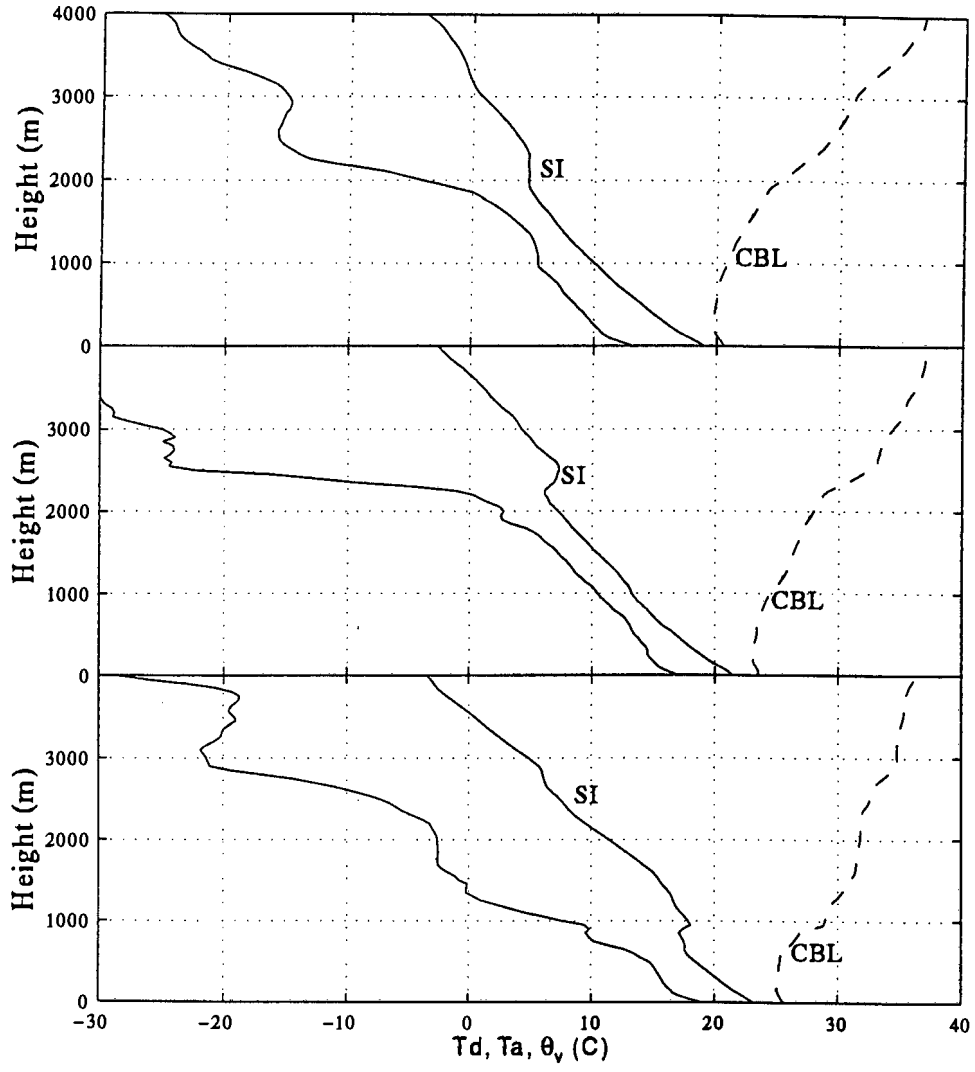

Figure 6.45: Composite plots of T_d, T_a and θ_v for the anticyclonic conditions of 28, 29 and 30 April. The plots are from top to bottom: southerly case (28 April), easterly case (29 April), northerly case (30 April). The approximate convective boundary layer (CBL) and subsidence inversion (SI) heights are shown.

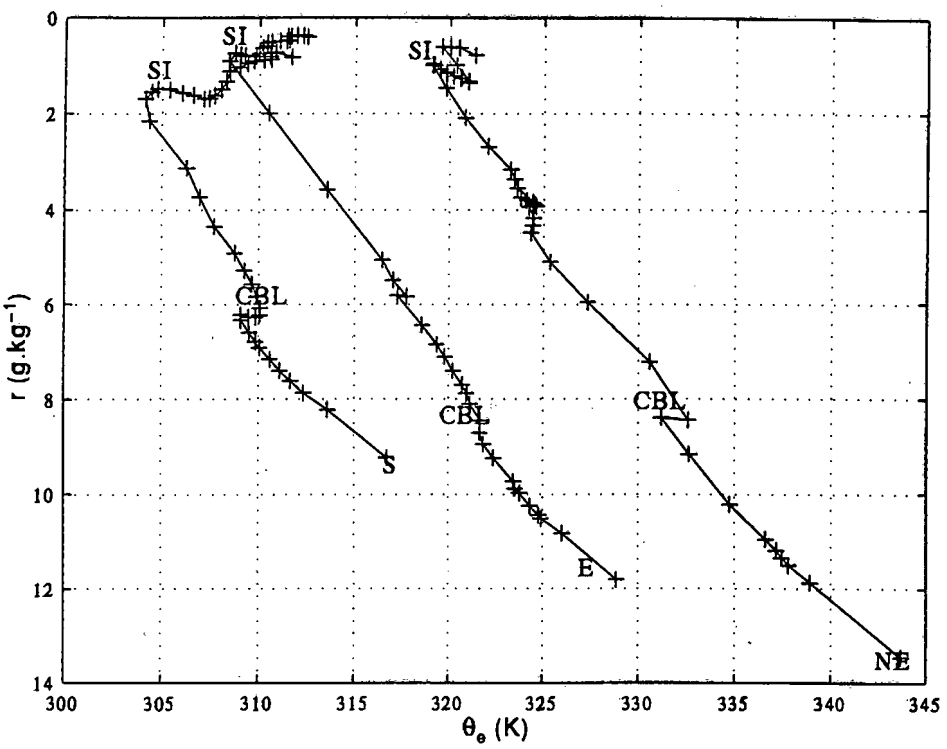

Figure 6.46: Conserved variable diagram of the mixing ratio, r, and equivalent potential temperature, θ_e, for the anticyclonic conditions of 28, 29 and 30 April. The plots are from left to right: southerly case, easterly case, northeasterly case (labelled S, E and NE). The plots corresponding to the southerly and northeasterly cases have been offset by - 2 °C and +8 °C to aid visualization The convective boundary layer top (CBL) and subsidence inversion (SI) are indicated.

The height and nature of the subsidence inversion (marked by θ_e reversals in Figure 6.46) is seen to vary significantly (Figure 6.45). Variations occur also in the stability and height of the mixed layer. z_i varies from $\simeq$500 m (northeasterly case) to $\simeq$1000 m (southerly case). The convective boundary layer is again characterized by a single mixing line contained by a kink in the $\theta e - r$ profile Figure(6.46).

It is interesting to note the apparent temporal decay of this kink (in keeping with the waning influence of the anticyclone). A concomittant lowering of the inversion above z_i occurs. Figure 6.45 clearly demonstrates this temporal evolution.

6.3.4 Boundary layer modification

For the cases studied in Section 6.3.2 the latent heat flux has been shown to be the main component of surface turbulent heat losses and resultant surface destabilisation. The inshore SST front is characterised by a large horizontal latent heat flux gradient (Tables 6.6 to 6.10; Figures 6.29, 6.33, 6.36, 6.39 and 6.42).

Whilst Jury (1993) has suggested that during airflow that is parallel to the SST front the transition of the boundary layer from the current to adjacent inshore region defines an atmospheric *thermal* front the analysis here leads to an alternative hypothesis. The large dQ_E/dy suggests that this transition may instead be defined by an atmospheric **moisture** front. The exact nature of such a moisture front will depend on the orientation of the mean boundary layer wind and intensity of the inshore SST front. This hypothesis can easily be tested using the data from the rawinsonde ascents conducted during ACASEX.

A pattern of transition from a convective boundary layer to a stable (or relatively more stable) one will be shown to be a central theme in all cases of boundary layer modification (and is in close agreement with the large dQ_T/dy and decay of turbulence over the shelf that has been found). Variations to this pattern as a result of synoptic scale processes will also be shown to occur.

6.3.4.1 Light, variable conditions

6.3.4.1.1 Low pressure Airflow for the case of 24 May was mostly **westerly** (approximately parallel to the isotherms with a small component from cold to warm). Figure 6.48 shows boundary layer differences over the shelf, inshore frontal region, current and seaward SST front. Although the q (and θ_v) profile over the shelf is suspect this profile has been retained to illustrate the stabilisation due to θ.

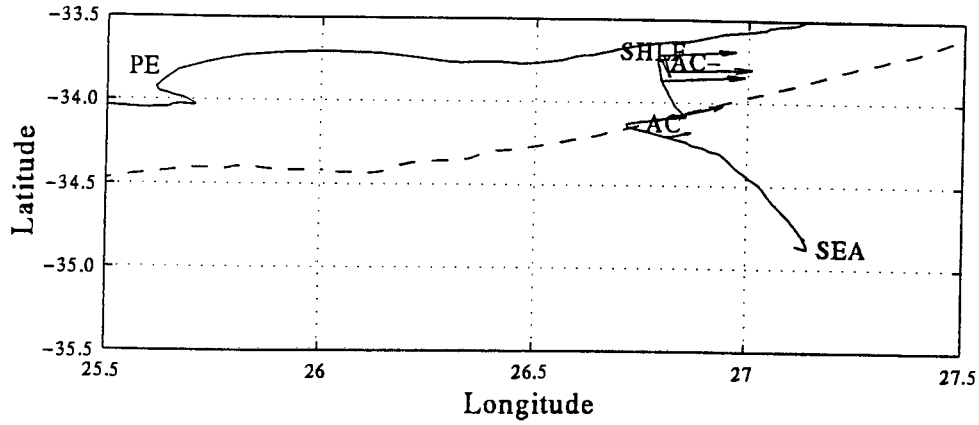

Figure 6.47: Location of rawinsonde ascents - light, variable conditions[a] (24 April). The positions of Port Elizabeth (PE) and the 200 m isobath (dashed) are shown. Labels denote the positions of atmospheric profiles found in Figure 6.48

The stable shelf profile is "capped" by an inversion. Destabilisation of the surface layer (in the inshore frontal region) then occurs as the first surface thermals mix vertically and a convective thermal internal boundary layer (CTIBL) structure is formed. The TIBL top is sharp (Figure 6.48; Stull, 1988, p 600). Downwind (over the Agulhas Current core) a shallow, well-mixed profile is attained. The profile is not as convective as might be expected due to diminishing surface heat fluxes (Figure 6.29). Beyond the current on the seaward border, surface heat and momentum fluxes are negligible and a stable profile is attained.

Variations in mean specific humidity $\overline{q}$, mean equivalent potential temperature $\overline{\theta}_e$ and z_i are shown in Table 6.11 . Highest $\overline{q}$ and $\overline{\theta}_e$ occur over the current. These results provide the first indication of a possible atmospheric moisture front.

Figure 6.50 shows boundary layer differences over the inshore front and current for the second transect (Figure 6.49). The pattern of stabilisation-destabilisation is repeated. Table 6.12 summarizes mean variations in q, θ, θ_e and z_i.

Although surface heat losses for 1 May have not been explicitly discussed (Section 6.3.2) this case is included as as an example of the convective TIBL development (Figure 6.52). Synoptic conditions were weakly pre-frontal although with a well developed inversion at $\simeq$600 m, This may be attributed to the waning anticyclonic influence which provided for synoptic-scale airflow that originated from the coast. Mean surface heat losses ($\overline{Q}_T$=194, $\overline{Q}_E$=163, $\overline{Q}_H$=31) were quite similar to the case discussed above. Surface westerly winds (across the SST front from cold to warm) were experienced in the study region.

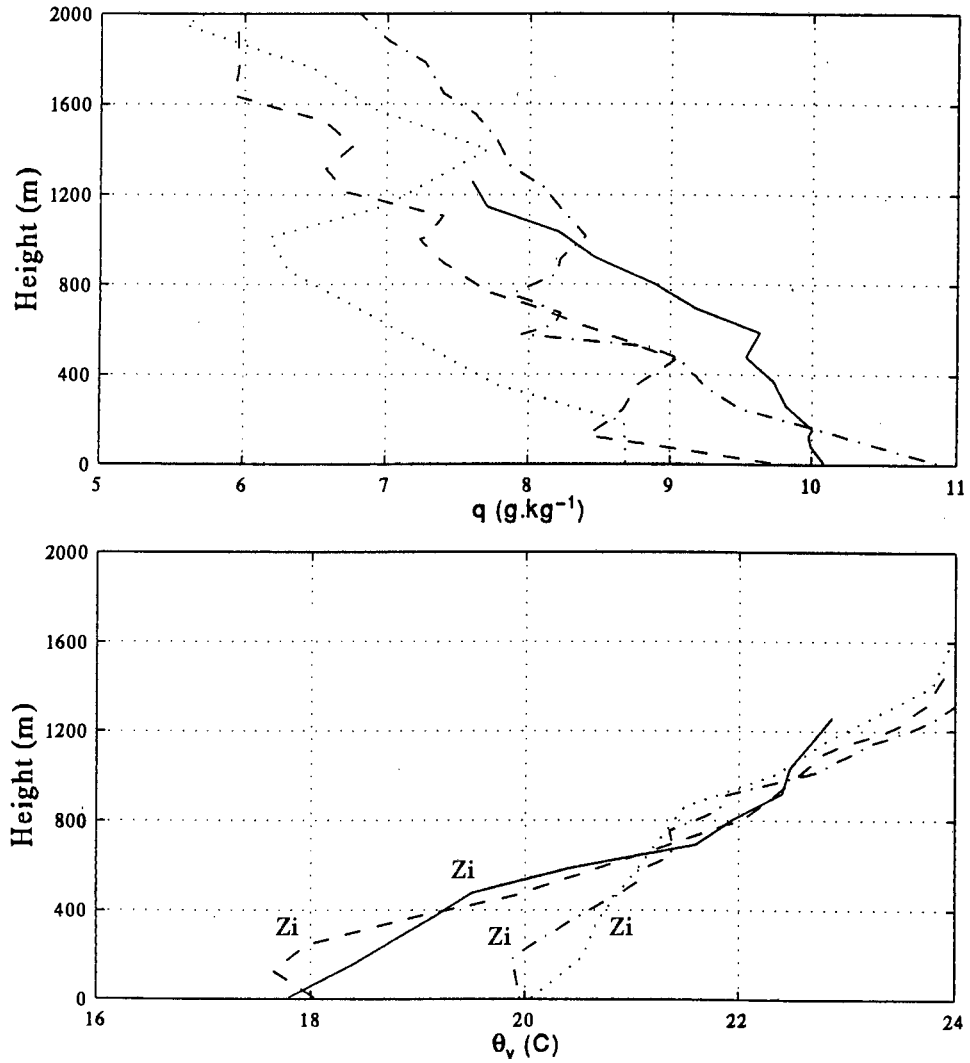

Figure 6.48: Atmospheric profiles showing boundary layer differences - light, variable conditions[a] (24 April). The plots are q (top) and θ_v (bottom); SHLF (-), AC$^-$ (- -), AC (-.) and SEA (:).

Table 6.11: Boundary layer differences - Light, variable synoptic conditions - weakly pre-frontal[a]

	$\overline{z}_i$ (m)	$\overline{q}$ (gkg^{-1})	$\overline{\theta}$ (°C)	$\overline{\theta}_e$ (°C)	COMMENTS
SHLF	500	9.8	17.0	45.1	SBL
AC$^-$	350	8.9	16.5	41.8	TIBL
AC	250	10.2	18.1	47.5	TIBL/ML
SEA	350	8.4	18.9	43.4	SBL

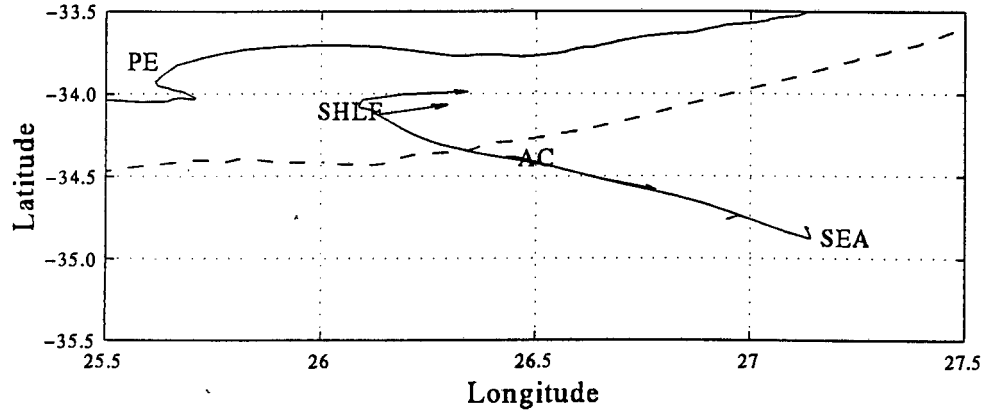

Figure 6.49: Location of rawinsonde ascents - light, variable conditions[b] (24 April). As for Figure 6.48 but for Figure 6.50

Table 6.12: Boundary layer differences - Light, variable synoptic conditions - weakly pre-frontal[b]

	$\overline{z}_i$ (m)	$\overline{q}$ (gkg^{-1})	$\overline{\theta}$ (°C)	$\overline{\theta}_e$ (°C)	COMMENTS
SHLF	200	8.4	15.8	41.5	SIBL
AC	300	10.1	18.8	48.0	ML
SEA	350	9.0	18.9	43.4	SBL

Table 6.13: Boundary layer modification - Light, variable synoptic conditions[c]

	$\overline{z}_i$ (m)	$\overline{q}$ (gkg^{-1})	$\overline{\theta}$ (°C)	$\overline{\theta}_e$ (°C)	COMMENTS
SHLF	400	8.6	19.4	44.2	SBL
AC$^-$	300	12.2	20.3	55.5	TIBL
AC	300	12.6	23.0	60.0	TIBL

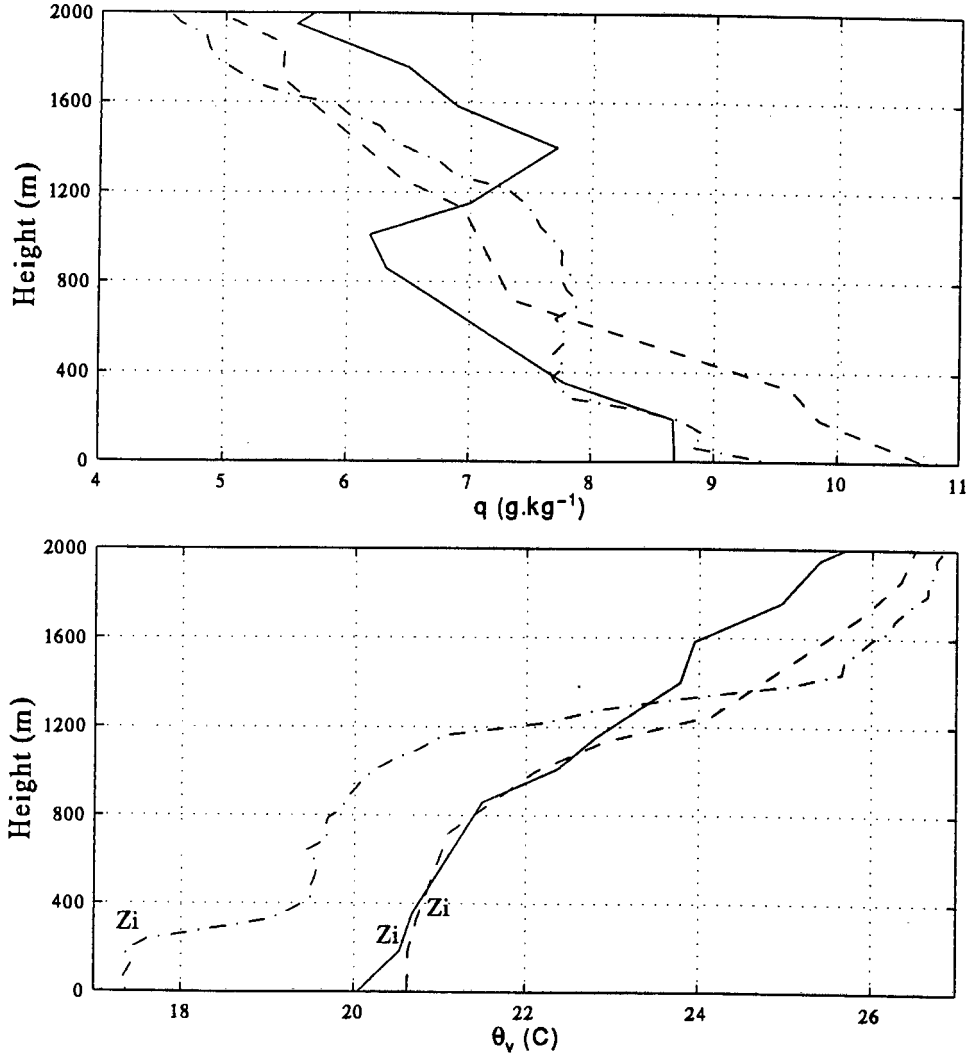

Figure 6.50: Atmospheric profiles showing boundary layer differences - light, variable conditions[b] (24 April). The plots are q (top) and θ_v (bottom); SEA (-), AC (- -), SHLF (–.).

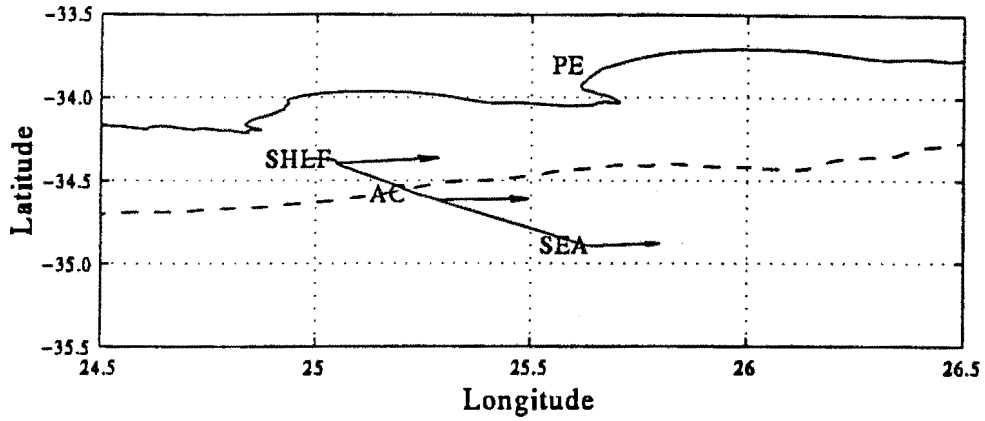

Figure 6.51: Location of rawinsonde ascents - light, variable conditions[c] (01 May). As for Figure 6.48 but for Figure 6.52

The pattern of transition from a stable to convective structure (in the downwind direction) is repeated.

The results presented here confirm the existence of an internal boundary layer at the SST front.

6.3.4.2 Anticyclonic conditions

6.3.4.2.1 Southerly, onshore airflow Thermodynamic differences in the profiles over the shelf front and seaward border during the this case (28 May) can be viewed from a Lagrangian perspective (i.e. an airmass with the initial properties of the seaward profile becomes modified to that of the shelf front profile). This may have important climatic implications.

Figure 6.54 shows significant heat (θ_e) and moisture (q) differences below 1000 m. Whilst the convective limit of surface parcels for the seaward scenario exceeds that of the shelf scenario, a comparison of the moisture profiles shows the seaward (shelf) area to have a layer well-mixed in q until 400 m (800 m). The deep moisture layer over the shelf exists as a **residual layer** (Stull, 1998; p 14-15). Moisture in this case acts as a passive tracer and indicates the former vertical extent of eddies whilst the θ_v profile indicates rapid convective adjustment over the shelf.

Table 6.14 summarizes the thermodynamic differences. $\overline{q}$ and $\overline{\theta}_e$ are $\simeq$2 gkg^{-1} and $\simeq$4.5 °C greater over the shelf. Integrating to 1000 m yields $\Delta_{\overline{q}} \simeq 2$ gkg^{-1} and $\Delta_{\overline{\theta}_e} \simeq 5.5$ °C

Owing to its possible climatological importance this case merits further attention. Results from a second transect conducted on 28 April (Figure 6.55) can be seen in Figure 6.56.

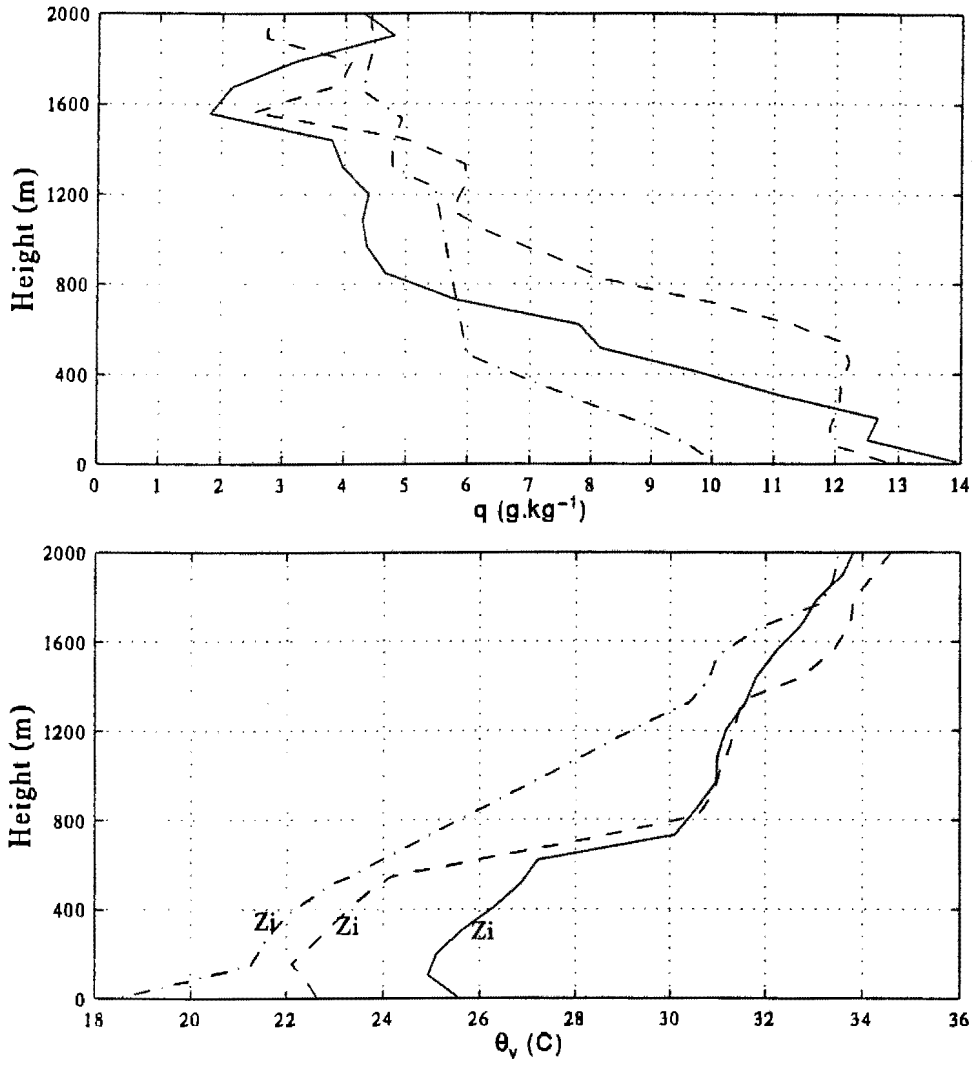

Figure 6.52: Atmospheric profiles showing boundary layer modification - light, variable conditions[c] (01 May). The plots are q (top) and θ_v (bottom); SEA (-), AC (- -), SHLF (-.).

Table 6.14: Boundary layer modification - Anticyclone - southerly, onshore flow[a]

	$\overline{z}_i$ (m)	$\overline{q}$ (gkg^{-1})	$\overline{\theta}$ (°C)	$\overline{\theta}_e$ (°C)	COMMENTS
SHLF	400	8.9	16.9	42.4	CBL
SEA	600	7.3	16.9	38.0	CBL

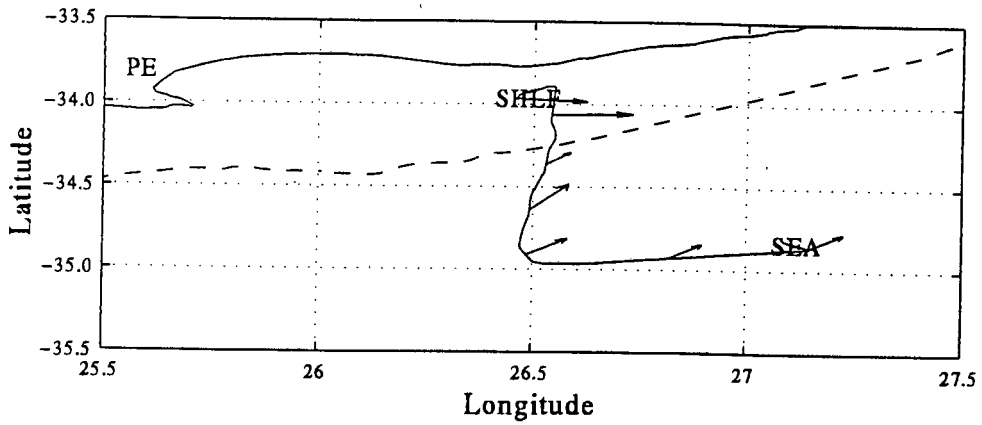

Figure 6.53: Location of rawinsonde ascents - southerly flow[a] (28 April). As for Figure 6.48 but for Figure 6.54

The convective nature of the boundary is eroded as the airmass moves over the cool shelf and an IBL is formed. The limit of (dry adiabatic) convection for the IBL is $\simeq$300 m. In contrast, mixed layer humidity depths (not neccessarily equal to the limit of surface convection z_i) over the current vary from 800 m to 1200 m. A **residual** humidity layer over the shelf is once again found to exist (between 600 m and 1400 m). Without exception, the boundary layer becomes warmer and more humid as air is advected over the current (Table 6.15). Boundary layer values of $\overline{q}$ and $\overline{\theta}_e$ for air over the shelf are approximately 2 gkg^{-1} and 6 °C greater than over the current.

Table 6.15: Boundary layer modification - Anticyclone - southerly, onshore flow[b]

	$\overline{z}_i$ (m)	$\overline{q}$ (gkg^{-1})	$\overline{\theta}$ (°C)	$\overline{\theta}_e$ (°C)	COMMENTS
SHLF	300	8.9	19.2	45.0	SIBL
AC$^-$	1200	7.3	19.0	40.3	CBL
AC	1400	6.7	19.6	39.1	CBL
SEA	800	7.0	17.1	37.3	CBL

These measurements (see also Section 6.3.2) provide the first documented evidence of moisture uptake of *onshore*-moving air over the Agulhas Current.

6.3.4.2.2 Easterly airflow Figure 6.58 follows the boundary layer structure across the current during easterly airflow parallel to the SST front. An initially stable boundary layer (seaward

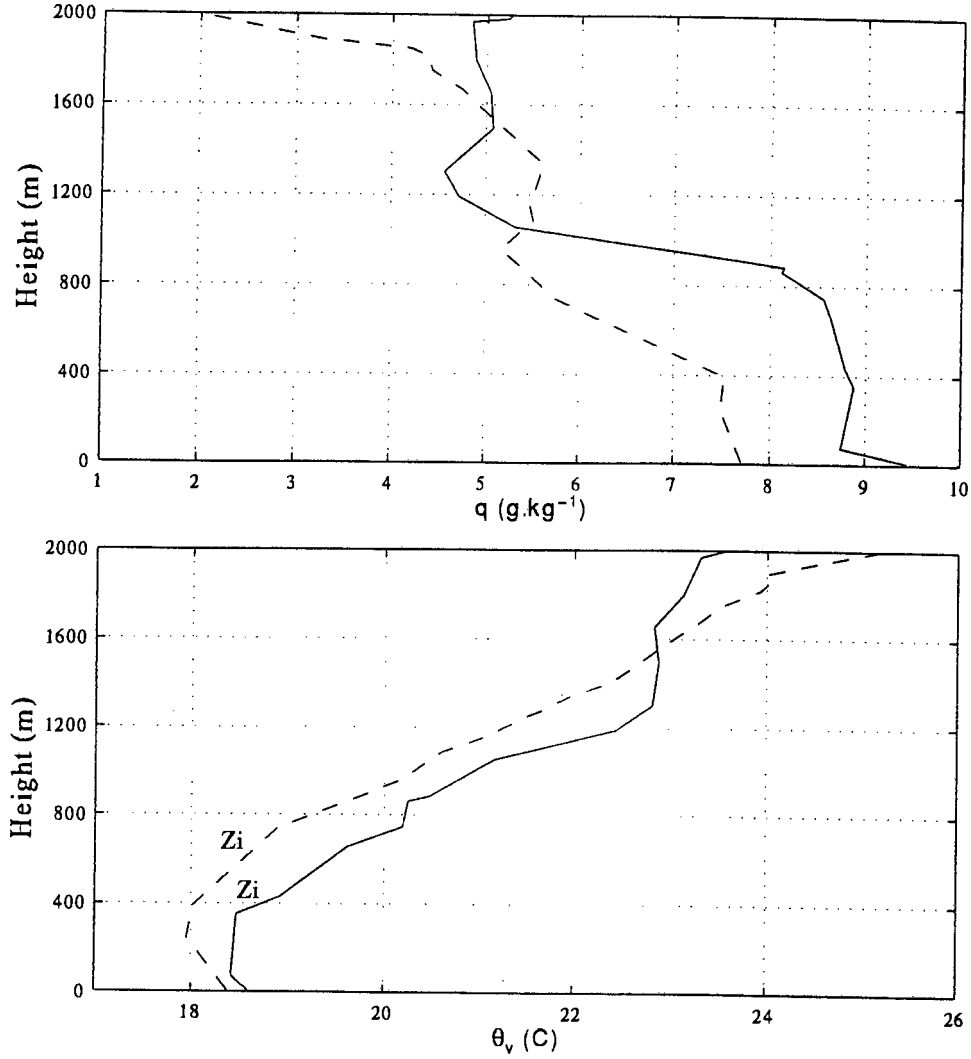

Figure 6.54: Atmospheric profiles showing boundary layer modification - southerly flow[a] (28 April). The plots are q (top) and θ_v (bottom); SHLF (-) and SEA (- -).

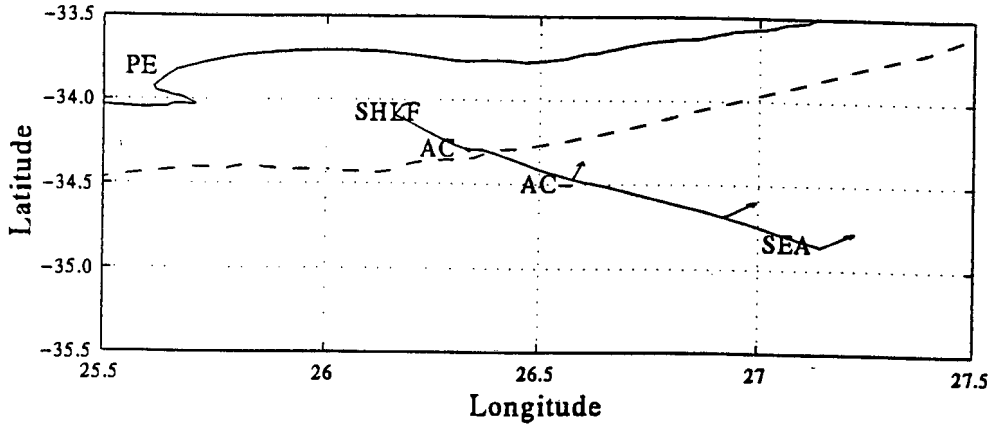

Figure 6.55: Location of rawinsonde ascents - southerly flow[b] (28 April). As for Figure 6.48 but for Figure 6.56

front) is replaced by a convective boundary layer (current) and shallow convective boundary layer (shelf). The convective nature of the shelf boundary layer is due to the small oceanic heat loss in this region.

The most interesting results for this case are the $\overline{q}$ and $\overline{\theta}_e$ differences (Table 6.16). AC^1 and AC^2 in Table 6.16 refer to the first and second ascent over the current.

Table 6.16: Boundary layer differences - Anticyclone - easterly flow

	$\overline{z}_i$ (m)	$\overline{q}$ (gkg^{-1})	$\overline{\theta}$ (°C)	$\overline{\theta}_e$ (°C)	COMMENTS
SHLF	700	9.7	20.6	48.9	CBL
AC^1	1000	10.7	21.6	52.7	CBL
AC^2	800	10.11	22.5	52.2	ML/SBL

Notwithstanding the convective nature of the shelf profile the boundary layer is drier than over the current. It would appear that the dQ_E/dy has also set up a weak **atmospheric moisture front**. With the horizontal sampling it is not possible to describe the nature and position of the axis of this moisture front. However, for the case of airflow parallel to the SST front it is likely to follow closely the horizontal latent heat flux profile. It will also be shown that this moisture front may extend vertically beyond the convective boundary layer due to cloud-scale mixing over the current (Section 6.3.5).

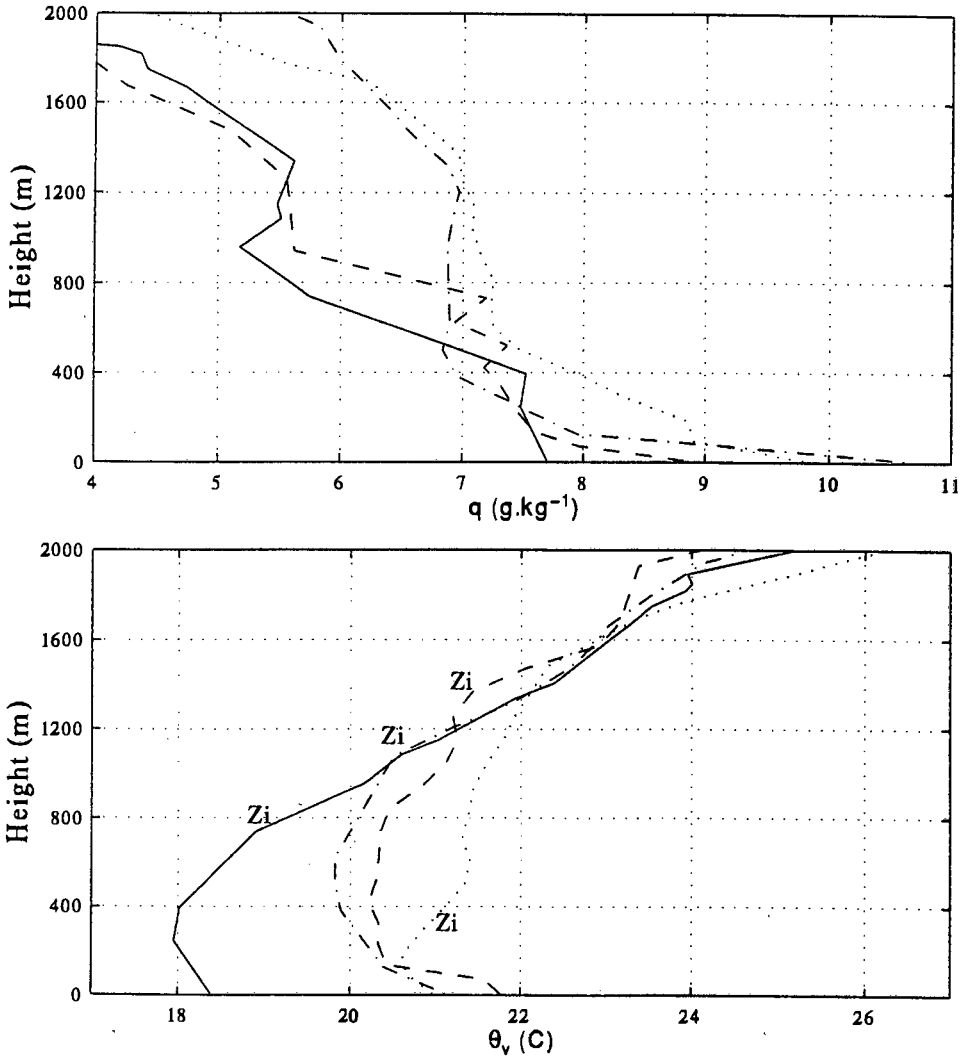

Figure 6.56: Atmospheric profiles showing boundary layer modification - southerly flow^b (28 April). The plots are q (top) and θ_v (bottom); SEA (-), AC$^-$ (- -), AC (-.) and SHLF (:).

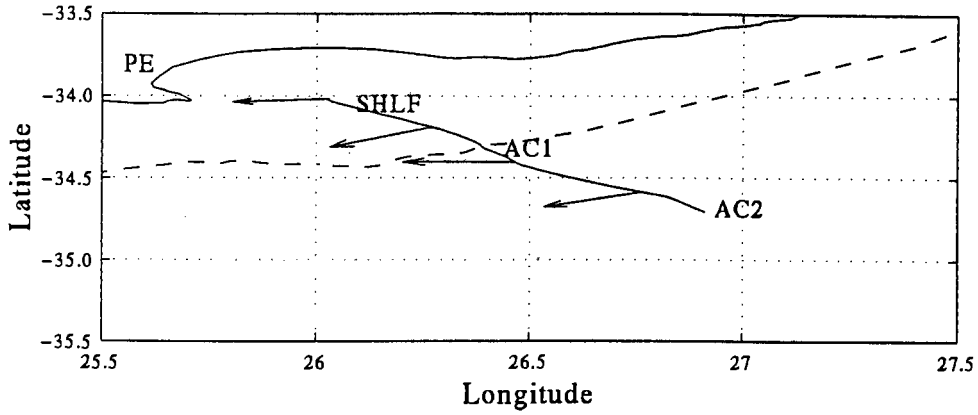

Figure 6.57: Location of rawinsonde ascents - easterly flow (29 April). As for Figure 6.48 but for Figure 6.58

6.3.4.2.3 North-easterly flow Boundary layer profiles in Figure 6.60 correspond to the shelf, shelf SST front and current respectively (Figure 6.59). The northeasterly airflow was approximately parallel to the SST front. The strong inversion in the profile over the current is related to a strengthening of the subsidence field (during the transect). A clear transition (convective to stable structure) exists (from the current toward the shelf). The large mean specific humidity difference ($\Delta_{\overline{q}} \simeq 2.5$ gkg^{-1}) between the shelf SST front and current core (Table 6.17) again indicates the existence of an *atmospheric moisture front* around the shelf SST front. $\overline{\theta}_e$ over the current core exceeds that over the shelf SST front by $\simeq$10 °C.

Table 6.17: Boundary layer differences - Anticyclone - northeasterly flow

	$\overline{z}_i$ (m)	$\overline{q}$ (gkg^{-1})	$\overline{\theta}$ (°C)	$\overline{\theta}_e$ (°C)	COMMENTS
SHLF	500	9.5	22.5	50.4	SBL
AC$^-$	700	10.0	22.7	52.0	CBL
AC	500	12.8	23.5	61.2	ML/SBL

6.3.5 Clouds

There is a complex coupling of radiative processes, latent heating, turbulence and vertical mixing due to clouds in cloudy boundary layers (Taylor et al., 1983, p 289; Stull, 1988, p 545). A feature of ACASEX was the persistent layer of cumulus clouds over the current, clear conditions over the shelf and scattered cumulus over the seaward border (Figure 6.61). The role of cumulus

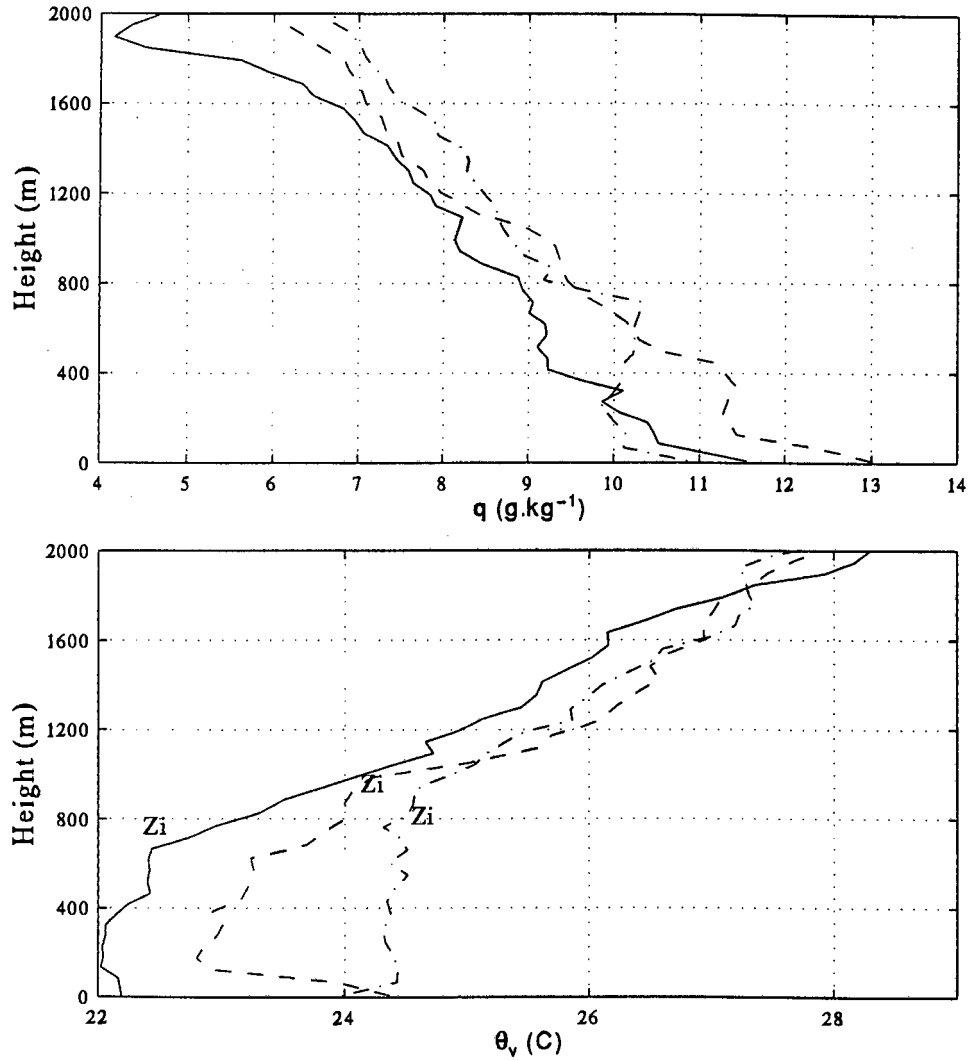

Figure 6.58: Atmospheric profiles showing boundary layer differences - easterly flow (29 April). The plots are q (top) and θ_v (bottom); SHLF (-), AC^1 (- -), AC^2 (-.). The latter profile is on the current side of the seaward front.

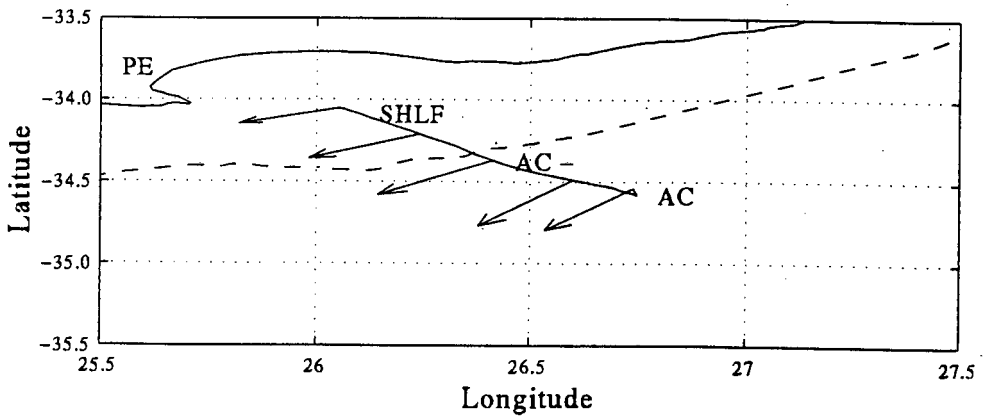

Figure 6.59: Location of rawinsonde ascents - northeasterly flow[a] (30 April). As for Figure 6.48 but for Figure 6.60

clouds in regulating boundary layer dynamics during ACASEX is difficult to assess.

It is not possible to investigate this relationship with the available dataset. This is an obvious shortcoming. However, an investigation of the spatial and temporal variability as well as an assessment of the liquid water contribution to the total atmospheric water content of clouds is possible.

Observations during ACASEX suggest that cumulus clouds are a ubiquitous feature above the Agulhas Current during most synoptic situations. This is illustrated in Figure 6.62 for 28 April. The potential temperature of an air parcel ascending from the base of the mixed layer show good agreement with the environmental potential temperature ($\theta_{environ}$) above cloud base. The environmental profile therefore follows a wet adiabat in this region. The relative humidity "composite" is included in Figure 6.62 for comparison. An increase in relative humidity occurs at cloud base and a decrease coincides approximately with cloud top. Figure 6.62 also shows that cloud growth will be limited by the subsidence inversion.

6.3.5.1 Evolution of convective available potential energy

The potential evolution of convective available potential energy (CAPE), level of free convection (LFC) and limit of convection (LOC) for the 24 April (westerly - front parallel, Figure 6.64), 28 April (southerly - onshore case, Figure 6.65) and 29 April (easterly - front parallel, Figure 6.66) cases are shown.

An example of the derivation of CAPE is given graphically in Figure 6.63.

In general the convective available potential energy is maximised over the current and is

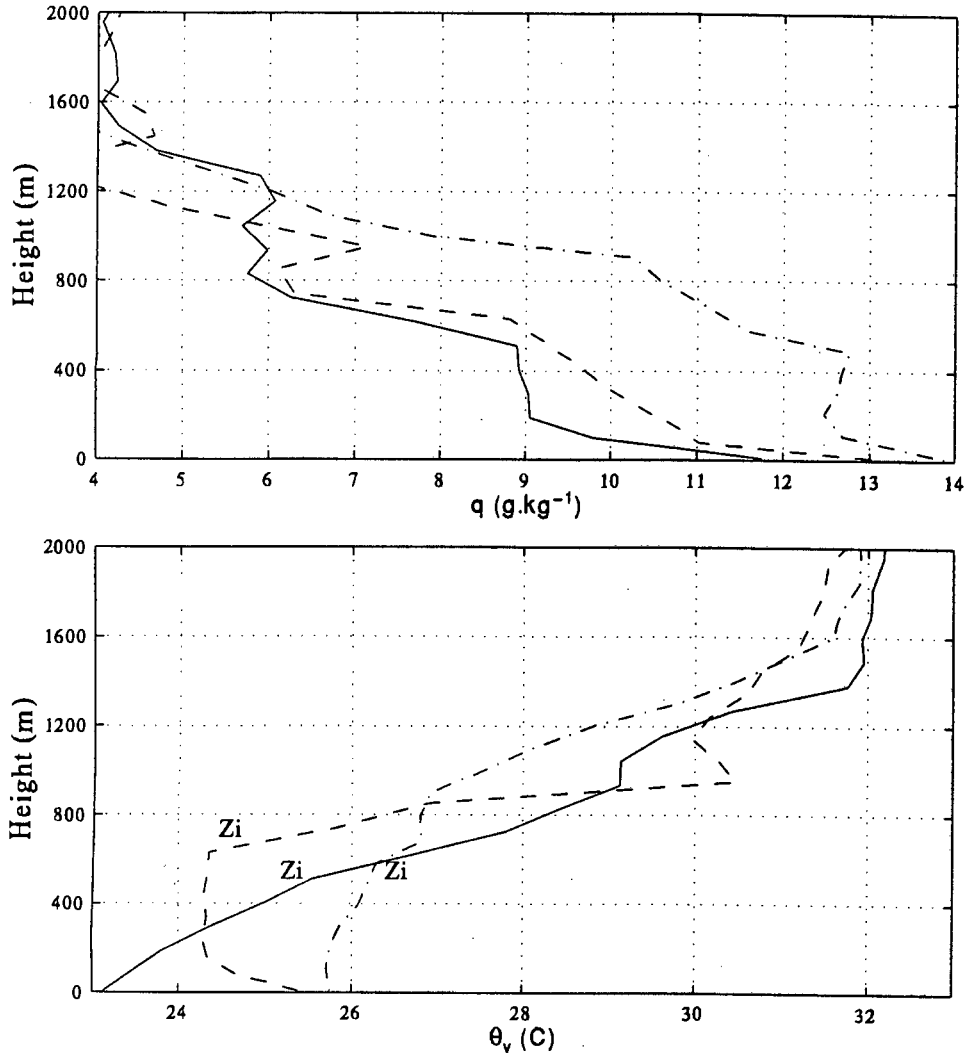

Figure 6.60: Atmospheric profiles showing boundary layer differences - northeasterly flow (30 April). The plots are q (top) and θ_v (bottom); SHLF (-), AC$^-$ (- -) and AC (-.).

Figure 6.61: Photographs of cumulus formation over the shelf, Agulhas Current and seaward regions. The photographs are from top to bottom, left to right: facing west toward the coast from the shelf (fair-weather conditions); facing east toward the Agulhas Current from the shelf (where the edge of the current is clearly demarcated by cumulus formation); cumulus formation over the Agulhas Current; facing seaward from the current where cumulus becomes more scattered.

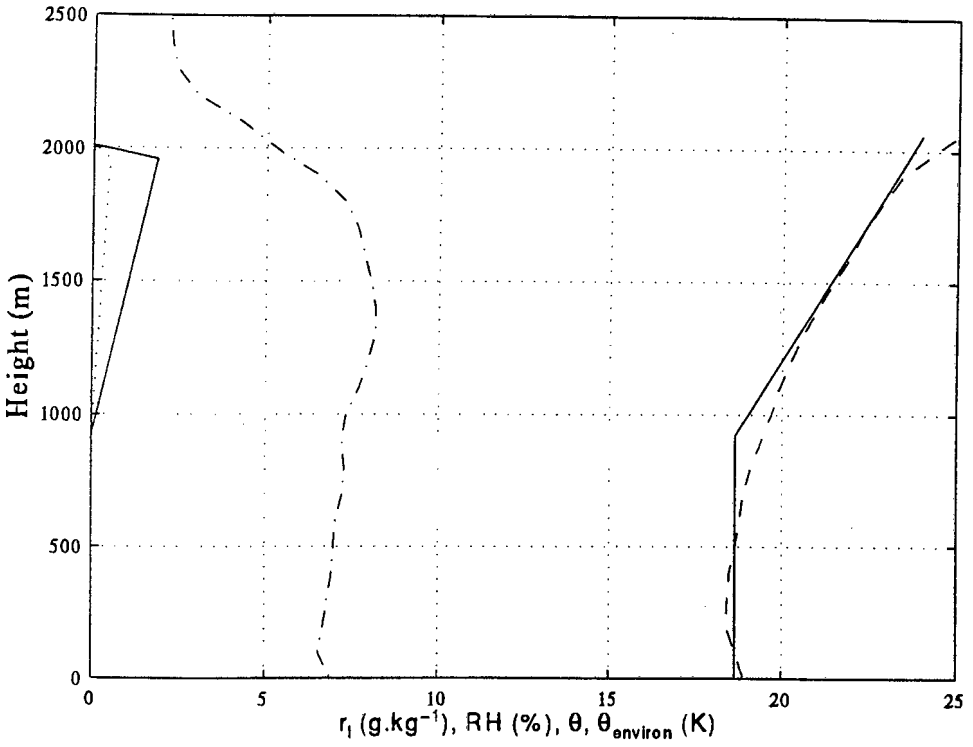

Figure 6.62: Schematic of environmental and adiabatic cloud paramaters from the composite of April 28. The plots are from left to right: the liquid water mixing ratio at a fraction (0.25) of the adiabatic value (:); adiabatic liquid water mixing ratio (-); relative humidity "composite" (calculated from T_a and T_d composites) (-.) and scaled by a factor of 10 to aid comparison; air parcel potential temperature, θ, (-) and environmental potential temperature, $\theta_{environ}$, (- -).

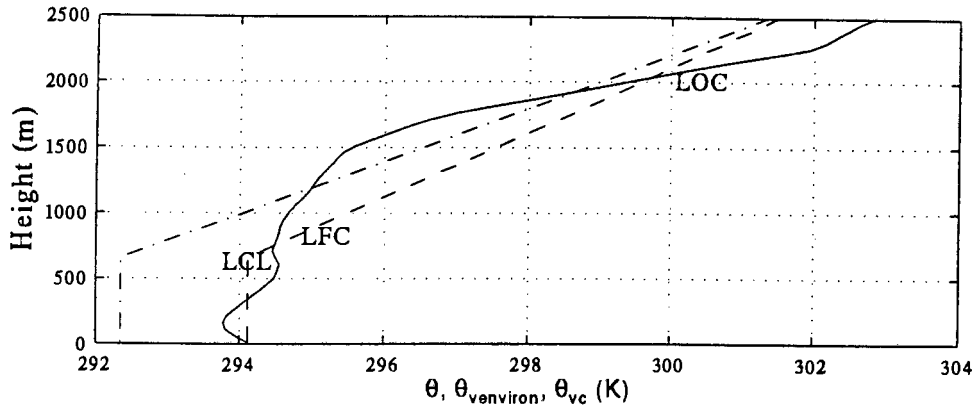

Figure 6.63: Schematic example of the derivation of the convective available potential energy. The surface air parcel initially follows a dry adiabat until the lifting condensation level (LCL) (a reasonable approximation of cloud base). It then follows the wet adiabat. The potential temperature of the air parcel path is shown (-.). The air parcel virtual potential temperature (- -) is θ_{vu} and θ_{vc} below and above cloud base. If the ascending parcel overcomes the area of negative bouyancy below the level of free convection (LFC) then it will continue to ascend until the limit of convection (LOC) where $\theta_{venviron} > \theta_{vc}$. The area of positive buoyancy is integrated to yield the convective available potential energy.

small or absent over the shelf and seaward regions.

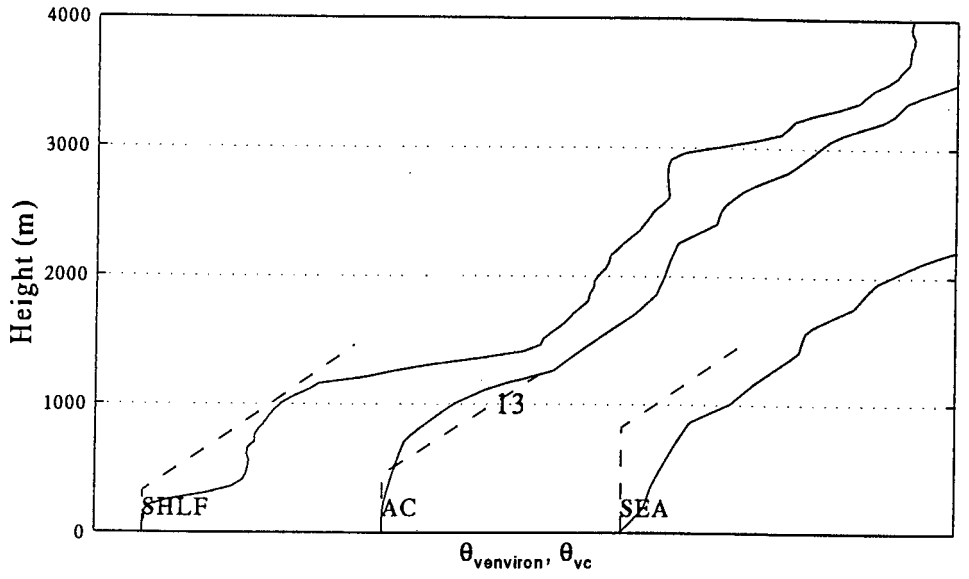

Figure 6.64: Evolution of convective available potential energy over the Agulhas Current on 24 April at the positions shown. The plots are the environmental ($\theta_{venviron}$) profile (-) and ascending air parcel (θ_{vc}) profile (- -) .The plots have been offset to aid visualization. The CAPE (in $m^2.s^{-2}$) is also given with each profile.

For the southerly (28 April) case (Figure 6.65) surface thermals over the seaward region do not attain a level of free convection as potential cloud parcels are always negatively buoyant relative to the environment. Over the current, surface thermals attain their lifting condensation level within the boundary layer. In this case it may be assumed that the cumulus clouds are convectively coupled to the surface. This has important implications for the redistribution of moisture in the vertical. Shallow cumulus convection is possible over the shelf. This requires sufficient inertia to overcome the negatively buoyant overshoot above the inversion. This may occur periodically and lead to scattered cumulus formation.

This pattern is repeated with some variation for the easterly case of 29 April (Figure 6.66). Potential cumulus formation is minimized over the seaward region. Over the current, deep cumulus convection is coupled to the surface. CAPE is weak over the shelf edge where cumulus convection was observed to be absent. This dramatic transition in cumulus was observed visually (Figure 6.61).

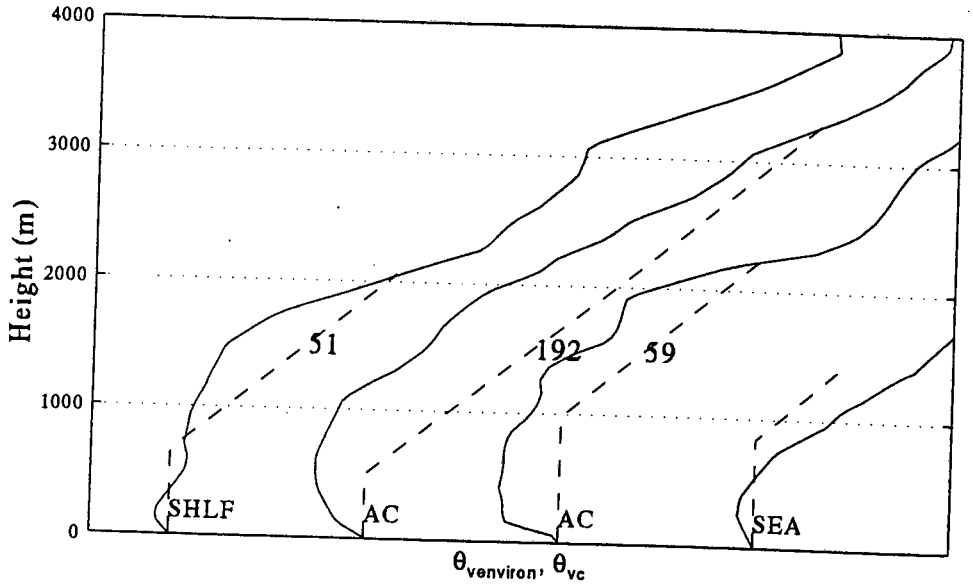

Figure 6.65: Evolution of convective available potential energy over the Agulhas Current on 28 April at the positions shown. As for Figure 6.64.

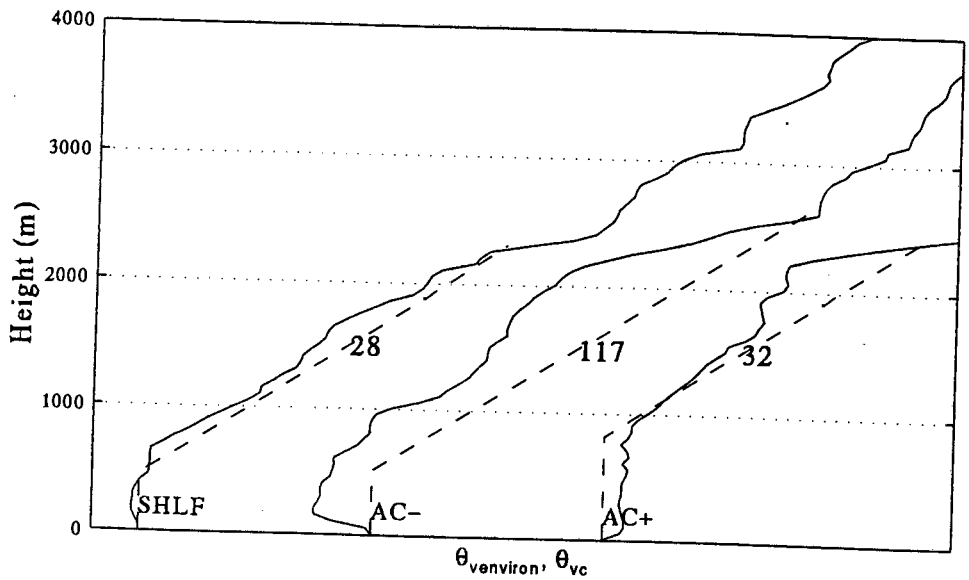

Figure 6.66: Evolution of convective available potential energy over the Agulhas Current on 30 April at the positions shown. As for Figure 6.64. The ascent AC^+ is adjacent to the seaward front on the current side.

Table 6.18: Precipitable water content of the atmosphere above the Agulhas Current. Estimates of the water vapour path $(\Delta z)_v$ are given for the boundary layer (BL), for the atmosphere below the subsidence inversion (SI) and for the atmosphere as a whole (TOTAL). Percentages refer to the ratio of water vapour path to the the total atmospheric water vapour path. The liquid water vapour path value for the northeasterly case (30 April) was negligible. See text for an explantion of the bracketed values (northeasterly case).

		BL		SI		TOTAL
	$(\Delta z)_l$ (mm)	$(\Delta z)_v$ (mm)	$(\Delta z)_{\%}$	$(\Delta z)_v$ (mm)	$(\Delta z)_{\%}$	$(\Delta z)_v$ (mm)
SOUTHERLY (28 April)	0.2	11.0	61	14.2	79	18.0
EASTERLY (29 April)	0.4	11.3	52	19.9	92	22.0
NORTHEASTERLY (30 April)	-	7.8 (11.6)	38 (56)	11.6 (18.5)	56 (89)	20.6
WESTERLY (25-26 April)	0.4	9.3	40	20.8	91	23.0

6.3.6 Precipitable water vapor content

The total precipitable water content (total water vapour path) is of interest climatologically. The high resolution ACASEX data is used here to provide for the first time an accurate description of this quantity.

Estimates of the water vapor path are given in in Table 6.18. The data used are the composites presented in Section 6.3.3. The liquid water path was calculated by assuming adiabatic ascent of an air parcel originating at the base of the mixed layer (eg., Betts and Ridgway, 1988, p 527). An average cloud layer interval of 1000 m was assumed. The liquid water profile was scaled by a factor of 0.25, an acceptable mean for cumulus clouds of this depth (Warner, 1970, Table 1). An example is given in Figure 6.62. Typically, $(\Delta z)_l$ is small (on the order of a few tenths of miilimetres). Estimates of the total water vapour path were obtained by integrating to 400 mb. Estimates for the northeasterly case are for a boundary layer and subsidence height of 600 m and 1000 m respectively. This gives a biased view in this case since average boundary layer and subsidence heights for the other cases were approximately 1000 m and 2000 m respectively. Therefore 1000 m and 2000 m estimates for this case are also given (bracketed in Table 6.18).

In general the boundary layer contains approximately 50 % of the total water vapour path. Up to 90 % is contained below the subsidence inversion. Boundary layer $(\Delta z)_v$ estimates for the anticyclonic cases are quite similar. Synoptic variations to the total water vapour path also occur.

Chapter 7

Conclusion

This section is a synthesis of the most important results.

Some large gaps in our knowledge of air-sea interactions over the Agulhas Current were outlined in Chapter 3. They relate to the inadequate description of surface turbulent fluxes, scant attention paid to the climatologically interesting quantification of moisture uptake especially for onshore-moving air originating seaward of the current, persistence of quasi-stationary secondary circulations, problem of separating thermodynamic and kinematic processes, absence of knowledge of the boundary layer above the northern Agulhas Current system, and the poor understanding of the response of the current to atmospheric circulation anomalies.

The need to investigate the characteristics of the boundary layer above the Agulhas Current is clear. The last three points have not been addressed in this thesis.

Other features of the boundary layer have emerged in the course of this study. They are the large horizontal inhomogeneity, the processes underlying the transition in cumulus, an atmospheric moisture front in the region of the inshore sea surface temperature front and the mean thermodynamic structure of the boundary layer.

The major results of this thesis may be summarized as follows:

1. Surface turbulent fluxes demonstrate short-term inhomogeneity. On a larger scale, large horizontal gradients of the latent heat flux occur.

2. An atmospheric moisture front and transition in atmospheric stability occurs in the boundary layer across the inshore sea surface temperature front. Significant moisture uptake occurs over the current during onshore airflow.

3. A transition in cumulus across the inshore sea surface temperature front owes its presence

to the spatial heat flux gradient.

4. The atmosphere contains two inversions. The first inversion caps the boundary layer and limits dry adiabatic convection. The second higher-level inversion is associated with synoptic-scale subsidence and limits the vertical extent of cumulus convection.

7.1 Surface fluxes of momentum, sensible and latent heat

A primary aim of this thesis was to accurately determine the surface fluxes of heat and momentum. The turbulent fluxes derived from fine resolution shipboard data demonstrated short-term inhomogeneity and large horizontal gradients at the edge of the current. Surface fluxes of sensible and latent heat were shown to be maximized over the current, decrease rapidly across the inshore sea surface temperature front and were small or negligible over the shelf. There is some uncertainty as to the validity of the bulk method in a region of strong sea surface currents.

Over the Agulhas Retroflection Region and Agulhas Current a sustained latent heat flux was measured during anticyclonic ridging behind a cold front.

7.2 Marine boundary layer modification and moisture uptake above the Agulhas Current

An objective derivation of the mean scalar quantities of the boundary layer has led to a useful description of mean changes within the boundary layer.

For airflow that was approximately **parallel** to the current the large latent heat flux gradient was manifested as an atmospheric moisture front with a moist and relatively dry boundary layer over the current and shelf respectively. A mean specific humidity difference in the boundary layer of approximately 2 gkg^{-1} exists between the shelf and Agulhas Current. A stable boundary layer over the shelf was replaced by an unstable, convective boundary layer over the current.

When winds were approximately **perpendicular** to the sea surface temperature front an internal boundary layer was observed to develop. The internal boundary layer was convective when the wind blew from cold to warm water and stable when the wind blew from warm to cold water. The stabilisation of the boundary layer over the shelf during onshore flow indicates rapid convective adjustment of large convective eddies to the spatial heat flux gradient. Significant moisture uptake within the boundary layer was measured during onshore flow over the Agulhas

Current. Mean specific humidity increased by nearly $2gkg^{-1}$ as air was advected towards the coast.

7.3 Cumulus convection

With few exceptions the horizontal heat flux gradient is also accompanied by a rapid transition in cumulus across the inshore sea surface temperature front. This transition is emphasised during airflow that is parallel to the current. Fair weather conditions and cumulus convection are found over the shelf and current respectively. The transition in cumulus may increase the vertical extent of the atmospheric moisture front through vertical redistribution of moisture. Whilst kinematic processes may not be discounted it has been shown that thermodynamic considerations adequately account for this cumulus transition. The vertical extent of cumulus is influenced by the atmospheric stability and is limited by the subsidence inversion.

7.4 Mean thermodynamic structure

A conserved variable method was used to investigate the mean thermodynamic structure of the boundary layer. This was found to be useful for the barotropic flow associated with anticyclonic ridging, but some uncertainty exists as to its applicability to the baroclinic mid-latitude depressions. A characteristic thermodynamic structure was found with variations due to synoptic type. The boundary layer was characterized by a mixing line. The inversion top separates boundary layer air from air having the properties of the free-atmosphere. A second, higher-level inversion is associated with radiative cooling and synoptic scale subsidence. The large observed vertical variations in the height of this second inversion have contributed to its confusion with the height of the boundary layer.

7.5 Secondary circulations

It is important to distinguish between the quasi-stationary feature observed by Jury (1993) and the secondary circulations referred to as organized large eddies or coherent structures by Brown and Foster (1994). The latter have dimensions comparable to the boundary layer height and advect with the mean wind. With the available data it was not possible to adequately investigate either feature. An unambiguous wind speed increase over the current and decrease over the shelf was observed to occur only once during a period of synoptic stationarity. For the

most part, rapidly changing synoptic conditions during the study period would have inhibited the establishment of any quasi-stationary structure such as observed by Jury (1993). In addition it is suggested that for light synoptic conditions this quasi-stationary feature may be absent. This may be seen from the small oceanic heat loss and predominantly stably-stratified boundary layer associated with light wind conditions. In the absence of convective eddies with any significant vertical extent the secondary thermal gradients of heat are unlikely to be established.

However, the short-term variability of the turbulent fluxes suggests that inhomogenous turbulent flow and organized large eddies may be inherent to the Agulhas Retroflection Region and Agulhas Current.

7.6 Overview

The Agulhas Current has frequently been linked to South African climate. Thus an emphasis has been placed on a useful quantification and characterization of the atmospheric boundary layer. Moisture uptake, mean thermodynamic properties and surface turbulent fluxes have been reliably determined for the first time in this region. The results confirm the hypothesis that moisture and heat uptake above the Agulhas Current is significant.

The results have also led to the unambiguous characterization of the boundary layer above the Agulhas Current as an area of high horizontal inhomogeneity. This inhomogeneity occurs on the scale of large convective eddies and the domain of the Agulhas Current. Large horizontal gradients of the surface turbulent fluxes were found to have far-reaching implications. Airmass properties over the Agulhas Current are radically different from the seaward and shelf regions. Atmospheric general circulation models have been criticized for not taking into account boundary layer inhomogeneity (Brown and Foster, 1994; Foster and Brown, 1994). The boundary layer over the Agulhas Current must be considered to be an excellent example of a region of extreme horizontal inhomogeneity. Its inclusion is vital to any successful model of South African climate.

References

Albrecht B A, C W Fairall, D W Thomson, A B White, J B Snider and W H Schubert, 1990, Surface based remote sensing of the observed and the adiabatic liquid water content of stratocumulus clouds, *Geophysical Research Letters*, **17**, 89-92.

Bane J M Jr, 1989, Results From the Genesis of Atlantic Lows Experiment, physical oceanographic studies: introduction, *Journal of Geophysical Research*, **94**, 10685.

Bane J M Jr, and K E Osgood, 1989, Wintertime air-sea interaction procceses across the Gulf Stream, *Journal of Geophysical Research*, **94**, 10755-10772.

Bang N D, 1970, Dynamic interpretations of a detailed surface temperature chart of the Agulhas Current retroflexion (sic) and fragmentation area, *South African Geographical Journal*, **52**, 67-76.

Betts A K, 1985, Mixing line analysis of clouds and cloudy boundary layers, *Journal of the Atmospheric Sciences*, **42**, 2751-2763.

Betts A K and B A Albrecht, 1987, Conserved variable analysis of the convective boundary layer thermodynamic structure over the tropical oceans, *Journal of the Atmospheric Sciences*, **44**, 83-99.

Betts A K and J Bartlo, 1991, The density temperature and the dry and wet virtual adiabats, *Monthly Weather Review*, **119**, 169-175.

Betts A K and W Ridgway, 1988, Coupling of the radiative, convective and surface fluxes over the equatorial Pacific, *Journal of the Atmospheric Sciences*, **45**, 522-536.

Blanc T. V., 1985, The effects of inaccuracies in weather-ship data on bulk-derived estimates of flux , stability and sea surface roughness, *Journal of Atmospheric and Oceanic Technology*, **3**, 12-25.

Blanc T V, 1987, Accuracy of bulk-determined flux , stability and sea surface roughness, *Journal of Geophysical Research*, **92**, 3867-3875.

Bolton D, 1980, The computation of equivalent potential temperature, *Monthly Weather Review*, **108**, 1046-1053.

Brown R A and R C Foster, 1994, On PBL models for general circulation models, *The Global Atmosphere and Ocean System*, **2**, 163-183.

Buck A L, 1981, New equations for computing vapor pressure and enhancement factor, *Journal of Applied Meteorology*, **20**, 1527-1532.

Budyko M I, 1963, Atlas of heat balance of the world, Glabnaia Geofiz. Observ., [Also: Guide to the atlas of the heat balance of the earth. Translation by I A Donehoo, 1963, U S Weather Bureau WB/T-106, Washington D C].

Bunker A F, 1976, Computations of surface energy flux and annual air-sea interaction cycles of the North Atlantic Ocean, *Monthly Weather Review*, **104**, 1122-1140.

Byrne D A, A L Gordon and W F Haxby, 1995, Agulhas eddies: a synoptic view using GEOSAT ERM data, *Journal of Physical Oceanography*, **25**, 902-917.

Cattle H and C Gordon, 1990, Specification and variability of the surface forcing of the ocean, 1990, in *Climate-Ocean Interaction*, editor: M E Shlesinger, Kluwer Academic Publishers, Netherlands, 193-210.

Charnock H and J A Businger, 1991, The frontal air-sea interaction experiment in perspective, *Journal of Geophysical Research*, **96**, 8639-8642.

DeCosmo J, K B Katsaros, S D Smith, R J Anderson, W A Oost, K Bumke and H Chadwick, 1996, Air-sea exchange of water vapour and sensible heat: The Humidity Exchange Over the Sea (HEXOS) results, *Journal of Geophysical Research*, **101**, 12001-12016.

de Ruijter W P M, 1982, Asymptotic analysis of the Agulhas and Brazil current systems, *Journal of Physical Oceanography*, **12**, 361-373.

de Ruijter W P M and D B Boudra, 1985, The wind-driven circulation in the South Atlantic-Indian Ocean, I, Numerical Experiments in a one-layer model, *Deep Sea Research*, **32**, 557-574.

Duncan C P, 1970, The Agulhas Current, PhD dissertation, University of Hawaii.

Duncombe Rae C M, 1991, Agulhas retroflection rings in the South Atlantic Ocean: an overview, *South African Journal of Marine Science*, **11**, 327-344.

Fairall C W, E F Bradley, D P Rogers, J B Edson and G S Young, 1996, Bulk parametrization of air-sea fluxes for TOGA COARE, submitted to *Journal of Geophysical Research.*

Fitschen L J and L W Gay, 1979, *Environmental Instrumentation*, Springer-Verlag, New York.

Foreman S J, 1990, The ocean as a component of the climate sytem, in *Climate-Ocean Interaction*, editor: M E Shlesinger, Kluwer Academic Publishers, Netherlands, 3-17.

Foster R C and R A Brown, 1994, On large-scale PBL modelling: surface wind and latent heat flux comparisons, *The Global Atmosphere and Ocean System*, **2**, 199-219.

Friehe C A, W J Shaw, D P Rogers, K L Davidson, W G Large, S A Stage, G H Crescenti, S J S Khalsa, G K Greenhut and F Li, 1991, Air-sea fluxes and surface layer turbulence around a sea surface temperature front, *Journal of Geophysical Research*, **96**, 8593-8609.

Geernaert G L, K B Katsaros and K Richter, 1986, Variation of the drag coefficient and its dependence on sea state, *Journal of Geophysical Research*, **91**, 7667-7679.

Gordon A L, 1986, Inter-ocean exchange of thermocline water, *Journal of Geophysical Research*, **91**, 5037-5046.

Gründlingh M L, 1980, On the volume transport of the Agulhas Current, *Deep-Sea Research*, **27**, 557-563.

Gründlingh M L, 1988, Review of cyclonic eddies in the Mozambique Ridge Current, *South African Journal of Marine Science*, **6**, 193-206.

Guymer T H, J A Businger, K B Katsaros, W J Shaw, P K Taylor, W G Large and R E Payne, 1983, Transfer processes at the air-sea interface, *Philosophical Transactions of the Royal Society of London*, **A 308**, 253-273.

Harris T F W , 1972, Sources of the Agulhas Current in the spring of 1964, *Deep-Sea Research*, **19**, 633-650.

Harrison M S J, 1984, A generalized classification of South African summer rain-bearing synoptic systems, *Journal of Climatology*, **4**, 547-560.

Hess G D, 1992, Observations and scaling of the atmospheric boundary layer, *Australian Meteorological Magazine*, **41**, 79-99.

Holton J R, 1979, *An introduction to dynamic meteorology, second edition*, Academic Press, San Diego, California.

Jury M R, 1993, A thermal front within the atmospheric boundary layer over the Agulhas Current south of Africa: Composite aircraft observations, *Journal of Geophysical Research*, **99**, 3297-3304.

Jury M R, 1994, A review of the meteorology of the eastern Agulhas Bank, *South African Journal of Science*, **90**, 109-113.

Jury M R and S Courtney, 1991, A transition in weather over the Agulhas Current, *South African Journal of Marine Science*, **10**, 159-171.

Jury M R and K Levey, 1993, The climatology and characteristics of drought in the eastern Cape of South Africa, *International Journal of Climatology*, **13**, 629-641.

Jury M R, H R Valentine and J R E Lutjeharms, 1993, Influence of the Agulhas Current on summer rainfall along the southeast coast of South Africa, *Journal of Applied Meteorology*, **32**, 1282-1287.

Jury M R and N D Walker, 1988, Marine boundary layer modification across the edge of the Agulhas Current, *Journal of Geophysical Research*, **93**, 647-654.

Katsaros K B, M A Donelan, W M Drennan and K M Howard, 1994, Surface fluxes and their relation to planetary boundary layer structure, in Proceedings of "*Air-Sea Interface Symposium, Radio and Acoustic Sensing, Turbulence and Wave Dynamics*", Marseilles, France, June 24-30, 1993.

Khalsa S J S and G K Greenhut 1989 Atmospheric turbulence structure in the vicinity of an oceanic front, *Journal of Geophysical Research*, **94**, 4913-4922.

Liu W T, K B Katsaros and J A Businger, 1979, Bulk parametrization of air-sea exchanges of heat and water vapour including the molecular constraints at the interface, *Journal of the Atmospheric Sciences*, **36**, 1722-1734.

Lutjeharms, J R E, 1981a, Features of the southern Agulhas Current circulation from satellite remote sensing, *South African Journal of Science*, **77**, 231-236.

Lutjeharms, J R E, 1981b, Spatial scales and intensities of circulation in the ocean areas adjacent to South Africa, *Deep-Sea Research*, **28**, 1289-1302.

Lutjeharms J R E, 1985, Location of frontal systems between Africa and Antarctica: some preliminary results, *Deep-Sea Research*, **32**, 1499-1509.

Lutjeharms J R E, 1988, On the role of the East Madagascar Current as a source of the Agulhas Current, *South African Journal of Science*, **84**, 236-237.

Lutjeharms J R E, 1996, The exchange of water between the South Indian and South Atlantic Oceans, in *The South Atlantic: Present and Past Circulation*, editors: Wefer G, W H Berger, G Siedler and D Webb, Springer-Verlag, accepted.

Lutjeharms J R E, N D Bang and C P Duncan, 1981, Characteristics of the currents east and south of Madagascar, *Deep-Sea Research*, **28**, 879-899.

Lutjeharms J R E and J Cooper, 1995, Upwelling inshore of the Agulhas Current, submitted to *Continental Shelf Research*.

Lutjeharms J R E , R D Mey and I T Hunter, 1986, Cloud lines over the Agulhas Current, *South African Journal of Science*, **82**, 635-640.

Lutjeharms J R E and H R Roberts, 1988, The Natal pulse: an extreme transient on the Agulhas Current, *Journal of Geophysical Research*, **93**, 631-645.

Lutjeharms J R E and H R Valentine, 1988, Eddies at the Sub-Tropical Convergence south of Africa, *Journal of Physical of Oceanography*, **18**, 761-774.

Lutjeharms J R E and R C van Ballegooyen, 1984, Topographic control in the Agulhas Current System, *Deep-Sea Research*, **31**, 1321-1337.

Lutjeharms J R E and R C van Ballegooyen, 1988a, The Retroflection of the Agulhas Current, *Journal of Geophysical Research*, **18**, 1570-1583.

Lutjeharms J R E and R C van Ballegooyen, 1988b. Anomalous upstream retroflection in the Agulhas Current, *Science*, **240**, 1770-1772.

Mesiä H, 1993, Humicap, 20 years of excellence, *Vaisala News*, **129**, 6-8.

Mey R D, N D Walker and M R Jury, 1990, Surface heat fluxes and marine boundary layer modification in the Agulhas Retroflection Region. *Journal of Geophyscical Research*, **95**, 15997-16015.

Olson DB and RH Evans, 1986. Rings of the Agulhas Current, *Deep-Sea Research*, **33**, 27-32.

Pearce A F, 1977 Some features of the upper 500 m of the Agulhas Current, *Journal of Marine Research*, **35**, 731-751.

Pearce A F and M L Gründlingh, 1982, Is there a seasonal variation in the Agulhas Current?, *Journal of Marine Research*, **40**, 328-331.

Preston-Whyte R A and P D Tyson, 1988, *The atmosphere and weather of southern Africa*, Oxford University Press, Cape Town, South Africa.

Rouault M, A M Lee-Thorp, I Ansorge and J R E Lutjeharms, 1995, Agulhas Current Air-Sea Exchange Experiment, *South African Journal of Science*, **91**, 493-496.

Rouault M, A M Lee-Thorp, I Ansorge and J R E Lutjeharms, 1996, *Data report on the Agulhas Current Air-Sea Exchange Experiment*, University of Cape Town, in preparation.

Rouault M and J R E Lutjeharms, 1994, Air-sea interaction in the marine atmospheric boundary layer: a new South African research venture, *South African Journal of Science*, **90**, 11-12.

Saetre R and A Jorge da Silva, 1984, The circulation of the Mozambique Channel, *Deep-Sea Research*, **31**, 485-508.

Schumann E H, 1981, Low-freqency fluctuations off the Natal Coast, *Journal of Geophysical Research*, **86**, 6499-6508.

Schumann E H, 1989, The propagation of air pressure and wind systems along the South African coast, *South African Journal of Science*, **85**, 382-385.

Schumann E H, L A Perrins and I T Hunter, 1982, Upwelling along the south coast of the Cape Province, South Africa, *South African Journal of Science*, **78**, 238-242.

Smith S D, 1988, Coefficients for sea surface wind stress, heat flux and wind profiles as a function of wind speed and temperature, *Journal of Geophysical Research*, **93**, 15467-15472.

Stramma L and J R E Lutjeharms, 1995, The flow field of the subtropical gyre of the South Indian Ocean, submitted to *Journal of Geophysical Research*.

Stull, R B, 1988, *An introduction to boundary layer meteorology*, Kluwer Academic Publishers, Dordrecht, The Netherlands.

Taylor P K, A L M Grant, H Günther and G Olbrück, 1983, Mass, momentum, sensible heat and latent heat budgets for the lower atmosphere, *Philosophical Transactions of the Royal Society of London*, **A 308**, 275-290.

Walker N D, 1990, Links between South African rainfall and temperature variability of the Agulhas and Benguela Current systems, *Journal of Geophysical Research*, **95**, 3297-3319.

Walker N D and R D Mey, 1988, Ocean/atmosphere heat fluxes within the Agulhas Retroflection Region, **93**, *Journal of Geophysical Research*, 15473-15483.

Webster P J and R Lukas, 1992, TOGA COARE: The coupled ocean-atmosphere response experiment, *Bulletin of the American Meteorological Society*, **73**, 1377-1416.